

NASA/CR—2001-210762



Theory for Broadband Noise of Rotor and Stator Cascades With Inhomogeneous Inflow Turbulence Including Effects of Lean and Sweep

Donald B. Hanson
United Technologies Corporation, East Hartford, Connecticut

Prepared under Contract NAS3-27727, AST Task 13

National Aeronautics and
Space Administration

Glenn Research Center

May 2001

Acknowledgments

This work was supported under Contract NAS3-27727 (AST Task 13) from NASA Glenn Research Center with Dennis Huff as the contract monitor. The author wishes to thank NASA and also Professor Stewart Glegg of Florida Atlantic University. Professor Glegg provided the harmonic cascade response code and documentation used to develop the broadband prediction procedure.

Available from

NASA Center for Aerospace Information
7121 Standard Drive
Hanover, MD 21076

National Technical Information Service
5285 Port Royal Road
Springfield, VA 22100

Available electronically at <http://gltrs.grc.nasa.gov/GLTRS>

TABLE OF CONTENTS

Section Number	Page Number
	v
Summary	v
1 Introduction	1
2 Background on Glegg’s Harmonic Cascade Theory	3
3 Coordinate Transformations and Geometry for Lean and Sweep.....	5
4 Derivation of Equations for Sound Power Spectrum.....	9
4.1 Generalization for Random Inflow	9
4.2 Transformation to Stationary Coordinate System.....	10
4.3 Acoustic Intensity	11
4.4 Reduce Upwash Spectrum to Standard Form for Turbulence Spectrum.....	12
4.5 Integral of Intensity for Sound Power.....	15
5 Turbulence Spectra for BBCascade	20
5.1 Liepmann Spectrum	20
5.2 Axi-symmetric Spectrum	21
6 Application of Theory & Formulas for BBCascade	24
6.1 Non-dimensional Forms.....	24
6.2 Integration and Summation Limits	25
6.3 Sample Calculation – Comparison with ADP Test Data.....	28
7 Interpretation of the Noise Equation – Spectra of Turbulence & Cascade Response..	29
8 Comparisons with Test Data and Related Parametric Studies.....	33
8.1 Variations on ADP Fan 1 – Turbulence Scale, Mach Number, etc.	33
8.2 Allison Fan and the Effects of Lean & Sweep on Stator Noise.....	41
8.3 Boeing Fan Analysis and Variations.....	49
9 Concluding Remarks.....	62
References.....	63
A Appendix A – Cascade Geometry for Lean and Sweep Analysis.....	64
B Appendix B – Wavenumbers in Various Coordinate Systems	71
C Appendix C – Symbols and Summary of Coordinates & Wavenumber Components	73



SUMMARY

The problem of broadband noise generated by turbulence impinging on a downstream blade row is examined from a theoretical viewpoint. Equations are derived for sound power spectra in terms of 3 dimensional wavenumber spectra of the turbulence. Particular attention is given to issues of turbulence inhomogeneity associated with the near field of the rotor and variations through boundary layers. Both radial and blade-to-blade variations in turbulence statistics are treated rigorously without adding significant complexity to the final noise equations. Lean and sweep of the rotor or stator cascade are also handled rigorously with a full derivation of the relevant geometry and definitions of lean and sweep angles using 2 independent angle conventions. This report treats noise response of a cascade to turbulence with specified statistical properties; it is assumed that turbulence properties will be provided from CFD calculations or measurement.

Derivation of the noise equations is made possible by the appearance of a flat plate, rectilinear cascade acoustic response theory by Professor Stewart Glegg of Florida Atlantic University. His theory includes a spanwise flow component (for treatment of the sweep effect) and a spanwise wavenumber component (in addition to the usual streamwise and gapwise wavenumber components in 2D theories). Glegg's theory is for waves that are sinusoidal in space and time. This report provides the statistical analysis required to apply Glegg's theory to the turbulence interaction problem. The final noise equations give the spectra of upstream and downstream sound power generated by turbulence interacting with a rotor or stator cascade. A specific recipe is given for dealing with inhomogeneity in terms of integrals of the turbulence covariance function (or of the turbulence spectrum function) at the cascade face.

The general theory has been incorporated into the fan noise prediction system BFaNS. This requires, as a minimum, providing the circumferential and radial distribution of turbulence over the cascade inlet plane. However, use of the general theory is illustrated herein by 2 simple theoretical spectra for homogeneous turbulence. One is the Liepmann spectrum (for isotropic turbulence) and the other is an axi-symmetric turbulence spectrum from the literature. Limited comparisons are made with data from model fans designed by Pratt & Whitney, Allison, and Boeing.

Parametric studies for stator noise are presented showing trends with Mach number, vane count, turbulence scale and intensity, lean, and sweep. Two conventions are presented to define lean and sweep. In the "cascade system" lean is a rotation out of its plane about the streamwise coordinate axis and sweep is a rotation of the airfoil in its plane. In the "duct system" lean is the leading edge angle viewing the fan from the front (along the fan axis) and sweep is the angle viewing the fan from the side (perpendicular to the axis). It is shown that the governing parameter is sweep in the plane of the airfoil (which reduces the chordwise component of Mach number). Lean (out of the plane of the airfoil) has little effect. Rotor noise predictions are compared with duct turbulence/rotor interaction noise data from Boeing and variations, including blade tip sweep and turbulence axial and transverse scales are explored.

The report also serves as documentation of the equations in BBCascade and as a reference for the BFaNS code. BBCascade treats a single geometry and mean flow; BFaNS integrates the BBCascade equations over geometry and flow as they vary over radius of a fan.



SECTION 1

INTRODUCTION

Figure 1 represents the side view of a turbofan with an upstream rotor and downstream stator. Broadband noise is generated when turbulence interacts with leading and trailing edges of stator vanes and rotor blades. Three of the leading edge interactions can be analyzed with the theory of this report and for each of these, the turbulence is intrinsically inhomogeneous or anisotropic, or both. For example, turbulence drawn into the inlet from the atmosphere or from flow over external objects interacts with the rotor. If the fan is stationary or moving slowly, the turbulent eddies are stretched in the flow direction so that the inflow turbulence tends to have an axi-symmetric form of anisotropy. In another mechanism, turbulence in the boundary layer of the duct interacts with the rotor. Since this is

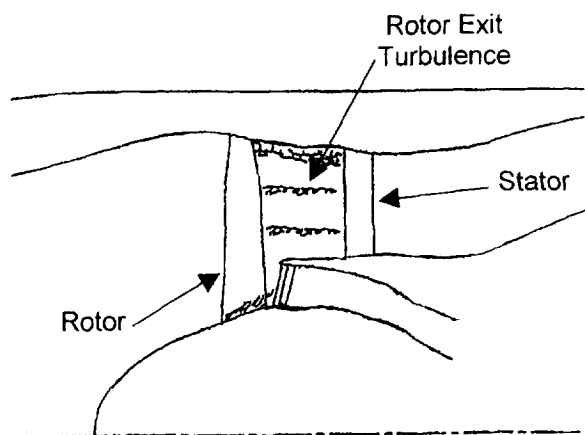


Figure 1. Noise generation in a turbofan by turbulence in rotor wakes impinging on stator.

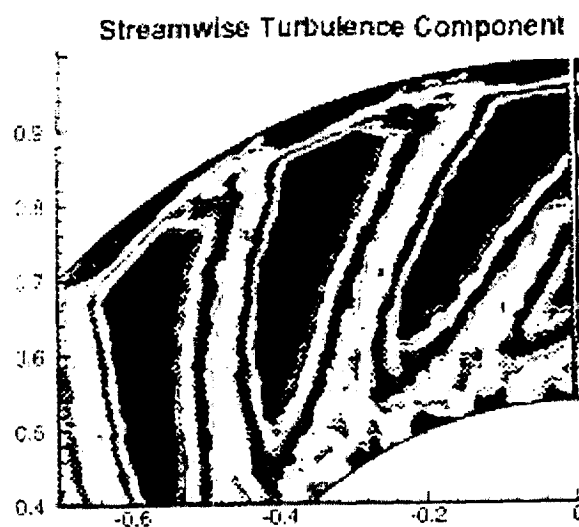


Figure 2. Inhomogeneity of rotor wake at entrance to stator. Test data from reference 1.

confined to a thin layer, it is highly inhomogeneous in the radial direction. Finally, wakes from the rotor blades impinge on the stator. The turbulence field behind a rotor is shown in Figure 2. It also is highly inhomogeneous with turbulence statistics varying periodically in the gapwise direction. A fundamental prediction theory is needed for these complex mechanisms that is sensitive to turbulence properties (scales and intensities) and that rigorously addresses the issues of inhomogeneity and anisotropy. Furthermore, with the current interest in lean and sweep of stator vanes and rotor blades, the theory should treat those geometries rigorously, also.

In this report, we develop theory for the spectra of upstream and downstream sound power from a rotor or stator cascade as an integral over the wavenumbers of the incoming turbulence field. The only simplification regarding representation of the turbulence is use of Taylor's hypothesis (i.e. the frozen gust assumption). This reduces the turbulence representation from a 4 dimensional wavenumber-frequency spectrum to a 3D wavenumber spectrum and results in manageable noise equations. The principal simplification regarding geometry is use of a rectilinear, flat plate cascade model. At low frequencies, this may be problematical; however, at mid and high frequencies where noise generation is dominated by small scale eddies, the rectilinear cascade approximation should be acceptable.

Some other aspects of this work have been published previously. Reference 2 examined the problem of measuring turbulent inflow to a stator for the purpose of making noise predictions. Two probe measurements are required and guidance for the required data processing and probe separation were given. Reference 3 showed in detail how the turbulence spectrum and the acoustic response spectrum work together in a stator noise calculation. Parametric studies showing trends with Mach number, vane count, turbulence scale, etc. were also given. Reference 4 is a greatly reduced version of this report that adds effects of lean and sweep to the previously published results.

This work has been enabled by the appearance of a harmonic cascade theory by Glegg (ref. 5) that this report adapts to the broadband problem. Glegg, too, has published broadband applications using his cascade theory. Reference 6 is a recent example. The main additions of the present report are the focus on lean and sweep plus treatment of turbulence inhomogeneity and anisotropy. It also serves as documentation for the code BBCascade, which treats rotors and stators in a unified analysis.

Analysis herein is confined to noise from a cascade with constant geometry and flow properties in the spanwise (or radial) direction. It is a useful analysis tool as is; however, for fan noise diagnosis and design it has been incorporated in Morin's BFaNS code (ref. 7). In BFaNS, geometry and flow for the leading edge sources on the rotor and stator are integrated over the fan radius using the theoretical equations of this report.

In the present report: Section 2 is a review of Glegg's harmonic cascade theory. Section 3 outlines the geometry of lean and sweep and gives the equations for transforming coordinate systems and wavenumbers from duct coordinates to Glegg's cascade coordinates. Section 4 is the derivation of the broadband noise theory. Section 5 presents the 2 turbulence spectra currently in use: one for isotropic turbulence and the other for axi-symmetric turbulence. Section 6 non-dimensionalizes the working equations and provides documentation for code BBCascade. Section 7 shows how the noise prediction equations work with illustrations of turbulence spectra and cascade response spectra. Section 8 shows the capability of the broadband theory via comparisons with test data from Pratt & Whitney, Allison, and Boeing test fans and by parametric variations to explore effects of turbulence scale, flow Mach number, stagger, solidity, vane lean & sweep, vane and blade count, and rotor sweep. Appendices A and B give details of coordinate and wavenumber transformations required for the analysis. Appendix C provides a list of notation.

SECTION 2

BACKGROUND ON GLEGG'S HARMONIC CASCADE THEORY

Previous noise models for turbulence/stator interaction have been based on simplifying assumptions some of which are no longer necessary. Some examples: treatment of the blades or vanes as isolated airfoils (as opposed to cascades), 2 dimensional theory, incompressible flow for airfoil loading response, and compact (as opposed to distributed) radiation theory for the acoustic sources. A recent analysis by Glegg^(ref 5) overcomes these limitations but still is tractable enough for calculations on ordinary computers. Furthermore, it can be adapted to leaned and/or swept cascades by virtue of a spanwise velocity component included with the mean flow.

As shown in Figure 3, geometry is constant in the z direction and the background flow is uniform: $U=(U,0,W)$. Airfoils are unloaded flat plates. Cascade gap, chord, and stagger angle are s , c , and χ .

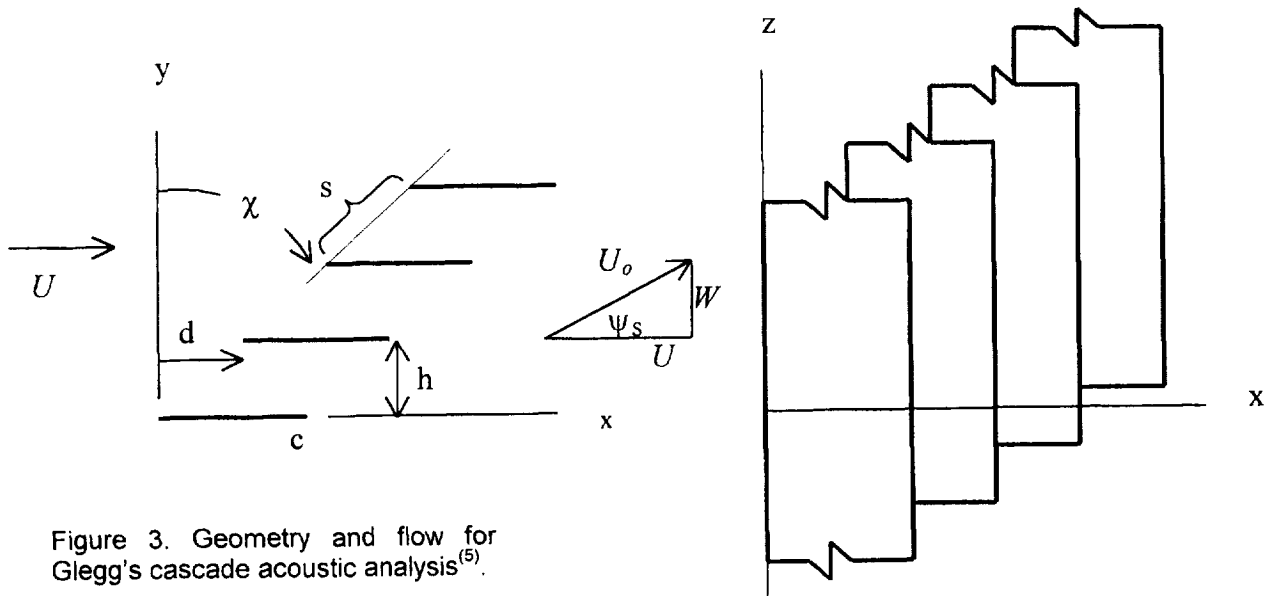


Figure 3. Geometry and flow for Glegg's cascade acoustic analysis⁽⁵⁾.

The unsteady flow is harmonic in space and time with upwash given by Equation 1

$$w(\mathbf{x}, t) = w_o e^{i(\gamma_o x + \alpha y + \nu z - \tilde{\omega} t)} \quad (1)$$

This represents a plane wave that is harmonic in time with frequency $\tilde{\omega} / 2\pi$ and upwash complex amplitude w_o . It is also harmonic in space with x , y , and z wavenumbers equal to γ_o , α , and ν . By use of Wiener-Hopf analysis, Glegg derived an equation equivalent to the following for the velocity potential of acoustic waves scattered by the cascade in response to the input wave of Equation 1

$$\phi^\pm(\mathbf{x}, t) = \pm \frac{\pi w_o c^2}{\beta s_e} \sum_{k=-\infty}^{\infty} \frac{\zeta_k^\pm D(\lambda_k^\pm)}{\sqrt{\kappa_e^2 - f_k^2}} e^{i[-\lambda_k^\pm(x-yd/h) + (\sigma - 2\pi k)y/h + \nu z]} e^{-i\tilde{\omega} t} \quad (2)$$

where the \pm signs refer to upstream/downstream going waves and

$$M = U / a \quad \beta = \sqrt{1 - M^2} \quad \omega_g = \tilde{\omega} - Wv \quad (3)$$

$$s_e = \sqrt{d^2 + \beta^2 h^2} \quad \tan \chi_e = d / \beta h \quad \lambda_k^\pm = \kappa M + \eta_k^\pm \quad (4)$$

$$\zeta_k^\pm = \beta \sqrt{\kappa_e^2 - (\eta_k^\pm)^2} \quad \kappa_e^2 = \kappa^2 - (v / \beta)^2 \quad \kappa = \omega_g / (a\beta^2) \quad (5)$$

$$\eta_k^\pm = -f_k \sin \chi_e \pm \cos \chi_e \sqrt{\kappa_e^2 - f_k^2} \quad f_k = (\sigma - 2\pi k + \kappa M d) / s_e \quad (6)$$

and $\sigma = \gamma_o d + \alpha h$ is the interblade phase angle. D is the Fourier transform of the discontinuity in potential across the blade and wakes (in the form of an infinite product) and is the major result of Glegg's derivation. The velocity, pressure, and density perturbations associated with the acoustic wave can be obtained from Equation 2 via

$$\mathbf{u} = \nabla \phi \quad p = -\rho_o D\phi / Dt \quad \rho' = p / a^2 \quad (7)$$

where ρ_o and a are the ambient density and speed of sound. We adhere to Glegg's notation closely. However, he used ω' for the radian frequency (our $\tilde{\omega}$), ω for the shifted frequency (our ω_g), and m for the scattering index (our k). Also, the D function of this report (and of Glegg's code) is non-dimensional; to obtain the D function of Glegg's report, multiply the non-dimensional version by $\omega_o c^2$.

The formulation above gives the acoustic waves scattered by a cascade for a single planar wave input per Equation 1. Scattering index k runs over an infinite range but, as usual in this kind of formulation, only a finite number of waves are cut on (propagate undiminished); the remaining waves decay exponentially and, thus, carry no acoustic energy. Cuton is governed by the argument of the square root $\sqrt{\kappa_e^2 - f_k^2}$; when the frequency is high enough, the argument is positive and the waves are cut on. The exponential dependence of the space and time variables in Equation 1 permits treatment of any inflow field via standard Fourier transform methods, as shown in Section 4.

SECTION 3

COORDINATE TRANSFORMATIONS AND GEOMETRY FOR LEAN AND SWEEP

This report requires several coordinate systems for the different parts of the analysis. One is aligned with the fan duct for the lean/sweep definition, one is aligned with the mean flow and the fan radius to define a turbulence symmetry axis, and one is aligned with the cascade geometry to apply Glegg's theory. Furthermore, rotating coordinates are needed for the rotor and stationary coordinates for the stator. The required transformations are treated in detail in Appendix A. In this section, we define the transformations and lean/sweep conventions and we summarize the most important geometrical relations between chord, gap, and stagger in the duct system and in the cascade system. We also define lean and sweep in 2 different conventions.

The coordinate systems connecting duct coordinates to Glegg's coordinates are shown in Figure 4. Stagger, lean, and sweep angles are defined via an ordered sequence of rotations about coordinate axes as follows. The sketch at the top represents the stator or rotor cut at constant radius and unwrapped onto the plane of the paper. The z_d and z_o axes are coincident with each other and with a fan radius. Mean flow U_o is aligned with the x_o direction and has no radial component. The following explanation of Figure 4 is in the context of vanes in a stator but it applies to rotors as well. In the transformations, the reference vane (vane #0, which passes through the origin) and vane #1 are handled differently. To visualize the rotations, think of rotating the reference vane and then rotating the coordinate system to re-align the z axis with the leading edge of the reference vane. For the other vanes, think of them as having hooks on their leading edges attaching them to the y_d axis with a separation g that does not change. Thus, throughout the lean and sweep rotations, the vanes always penetrate the constant radius plane ($z_o = 0$) at the location and orientation given by the gap g and the stagger θ at the top right of Figure 4.

Lean is an *out of plane of the vane* rotation about the x_o axis through angle ψ_l . Note that lean does not change the component of inflow mean velocity normal to the leading edge. Sweep is then an *in plane* rotation about the y' axis through angle ψ_s . This *does* reduce the flow component normal to the leading edge by the factor $\cos \psi_s$. Thus, transformation from duct coordinates (x_d, y_d, z_d) to Glegg's cascade coordinates (x, y, z) requires an ordered sequence of rotations (stagger, lean, sweep) about the $z_d, x_o,$ and y' axes. The net transformation, derived in Appendix A, is represented by

$$\begin{bmatrix} x \\ y \\ z \end{bmatrix} = [Q] \times \begin{bmatrix} x_d \\ y_d \\ z_d \end{bmatrix} \quad (8)$$

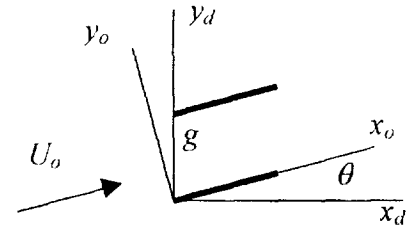
where

$$[Q] = \begin{bmatrix} \cos \theta \cos \psi_s + \sin \theta \sin \psi_l \sin \psi_s & \sin \theta \cos \psi_s - \cos \theta \sin \psi_l \sin \psi_s & -\cos \psi_l \sin \psi_s \\ -\sin \theta \cos \psi_l & \cos \theta \cos \psi_l & -\sin \psi_l \\ \cos \theta \sin \psi_s - \sin \theta \sin \psi_l \cos \psi_s & \sin \theta \sin \psi_s + \cos \theta \sin \psi_l \cos \psi_s & \cos \psi_l \cos \psi_s \end{bmatrix} \quad (9)$$

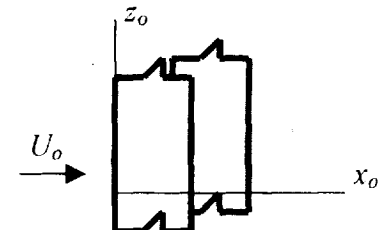
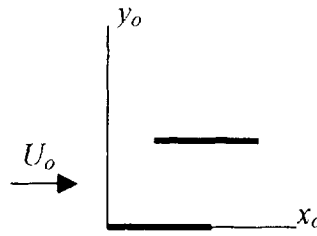
STAGGER ANGLE θ

Vane sections at constant radius unwrapped onto x_d, y_d plane (duct coordinates).

x_o, y_o coordinates aligned with vanes at stagger angle θ . z_d and z_o axes aligned with leading edge of reference vane.

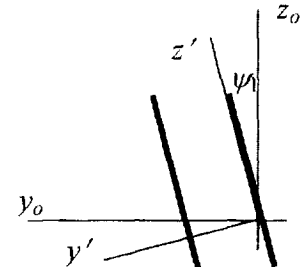
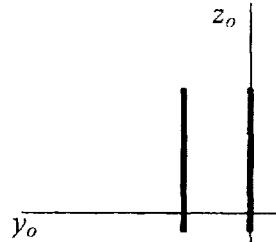


Other views in the x_o, y_o, z_o system. For the lean and sweep operations to follow, consider the vanes attached to the y_d axis with "hooks". Coordinate systems follow the reference vane; vane #1 stays parallel to ref. vane (hooked at $y_d = g$).



LEAN ANGLE ψ_l

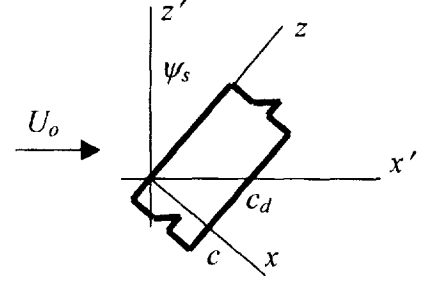
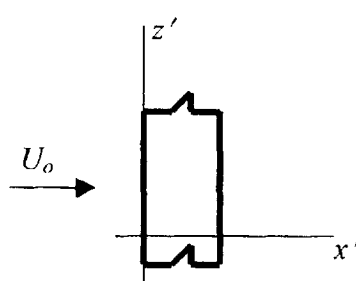
Lean the reference vane about the x_o axis through angle ψ_l . z' axis follows leading edge, x' axis coincides with x_o axis. Because of the "hook", the gap in the x_d, y_d system is not changed.



SWEEP ANGLE ψ_s

Sweep the vane in its own plane through angle ψ_s . Velocity vector does not change. c_d is the chord measured at constant radius in the fan.

$$c = c_d \cos \psi_s$$



The x, y, z coordinates are now Glegg's cascade coordinate system.

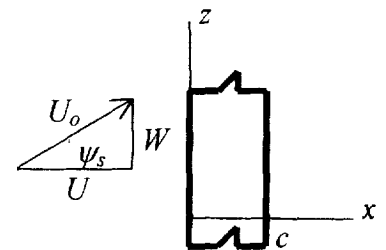
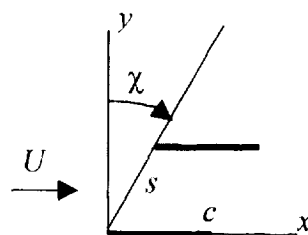


Figure 4. Sequence of rotations to relate cascade coordinates (x, y, z) to duct coordinates (x_d, y_d, z_d) and intermediate systems.

Relationships between the velocity components in cascade-fixed coordinates are easy to deduce from the figure

$$\begin{aligned} U &= U_o \cos \psi_s \\ W &= U_o \sin \psi_s \end{aligned} \quad (10)$$

where U_o is the total mean inflow velocity (in cascade-fixed coordinates).

If we say that the geometry descriptors in the duct system are chord c_d , stagger θ , gap g , lean angle ψ_l , and sweep angle ψ_s and in the cascade system are chord c , gap s , stagger angle χ , and sweep angle $\psi_s = \arctan(W/U)$, then the connection between the 2 systems is given by the following equations. The relation between the chords c and c_d is simply

$$c = c_d \cos \psi_s \quad (11)$$

where c_d is chord measured at constant radius (along the flow direction). Appendix A shows that Glegg's stagger dimensions in Figure 3 are given by

$$\begin{aligned} d &= Q_{12} g = (\sin \theta \cos \psi_s - \cos \theta \sin \psi_l \sin \psi_s) g \\ h &= Q_{22} g = (\cos \theta \cos \psi_l) g \end{aligned} \quad (12)$$

From these, his gap and stagger angle are

$$s = \sqrt{d^2 + h^2} = g \sqrt{Q_{12}^2 + Q_{22}^2} \quad (13)$$

$$\tan \chi = d/h = Q_{12}/Q_{22} \quad (14)$$

We can also define lean and sweep angles via a convention more suitable to viewing from the point of view of mechanical design. Consider the sketch below where the cascade is viewed along the fan axis for lean (on the left) and from the side for sweep (on the right).

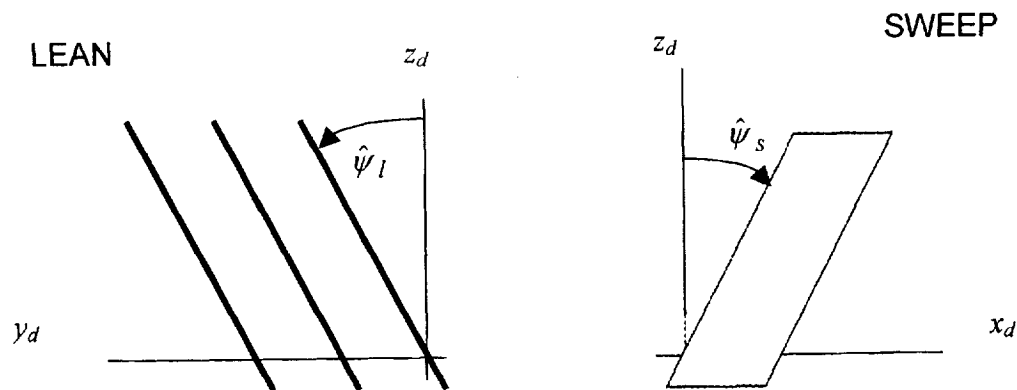


Figure 5. Lean and sweep angles defined via front and side views of stator

Here the lean and sweep angles have hats to distinguish them from the angles used in Figure 4. The relationship between the 2 systems is derived in Appendix A and is repeated below.

$$\begin{aligned}\tan \psi_l &= \cos \theta \tan \hat{\psi}_l - \sin \theta \tan \hat{\psi}_s \\ \tan \psi_s &= \cos \psi_l (\sin \theta \tan \hat{\psi}_l + \cos \theta \tan \hat{\psi}_s)\end{aligned}\tag{15}$$

Equations 13 must be solved sequentially. Thus, given lean and sweep angles in the “duct system” above, they can be converted to the “no hat” system for use with Equations 9 – 12. The inverse of Equations 15 giving $\hat{\psi}_l$ and $\hat{\psi}_s$ as functions of ψ_l and ψ_s can also be found in Appendix A.

SECTION 4

DERIVATION OF EQUATIONS FOR SOUND POWER SPECTRUM

In developing the theory of this report, the derivation was made as general as possible. The result is a single analysis that applies to noise from rotors and stators with lean and sweep. Turbulence is represented by a 3D wavenumber spectrum defined in a manner to include inhomogeneity and anisotropy. It will be seen that the general expression for acoustic *intensity* is too cumbersome for numerical work. Intensity varies with radial and gapwise position of the field point in the duct. However, when intensity is integrated (or averaged) over the duct area to compute *sound power*, the formulas simplify dramatically and tractable equations are found that treat inhomogeneity rigorously. It turns out that averaging in the field coordinates permits an averaging over the turbulence properties in the gapwise direction and an integration of the turbulence in the radial direction. Thus, the turbulence spectrum needed for input to the theory must represent the gapwise average of the field; for stator inflow, this is what would be measured by probes at the stator inlet with time averages over many rotor revolutions automatically giving the correct gapwise averaging of the turbulence field.

The sketches below show the general case analyzed and how it can be applied to rotor and stator problems. Rotors can be analyzed with axial inflow or swirling outflow, but not both.

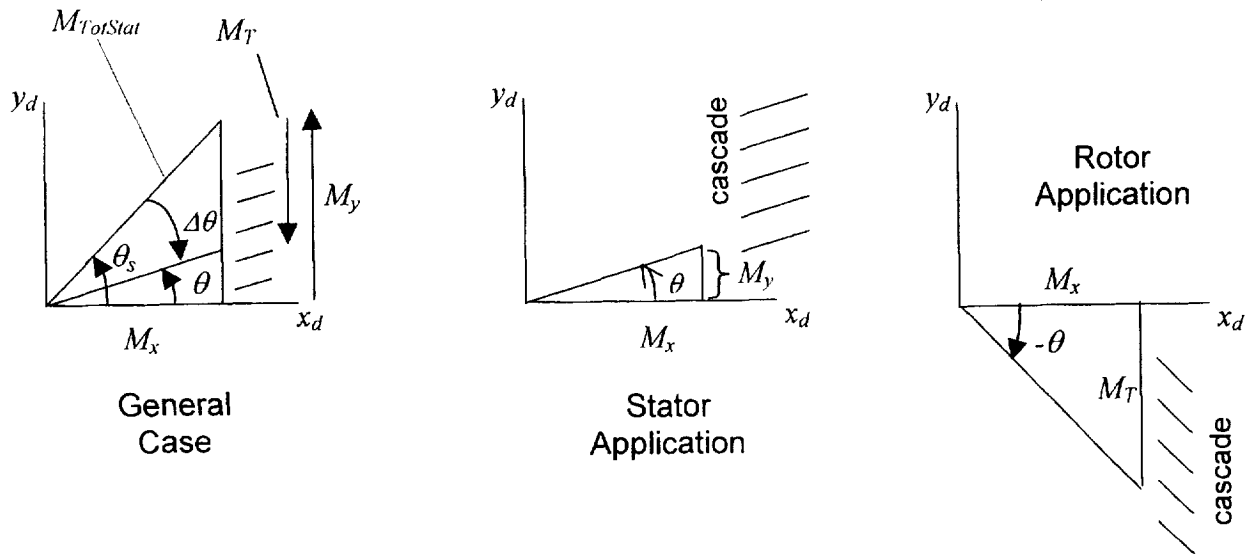


Figure 6. Mean flow viewed in constant radius "plane". General case with swirl and rotor rotation plus 2 specialized applications: stator with swirling inflow and rotor with axial inflow.

4.1 Generalization for Random Inflow

Glegg's formulation described in Section 2 was written for 3D planar, harmonic waves. His theory can be extended to an input upwash $\tilde{w}(\tilde{\mathbf{x}}, t)$ with any waveform and spatial distribution via the Fourier transform

$$w(\tilde{\mathbf{x}}, t) = \iint W(\mathbf{K}, \tilde{\omega}) e^{i(\mathbf{K} \cdot \tilde{\mathbf{x}} - \tilde{\omega} t)} d\mathbf{K} d\tilde{\omega} \quad (16)$$

where here, and throughout this paper, integration limits are from $-\infty$ to ∞ unless otherwise specified. We placed a tilde (\sim) on the ω to denote frequency in the cascade frame. Most of the derivation below uses this source frequency; at the end this is shifted to observer frequency in the stator frame to obtain the desired acoustic spectrum. Vector wavenumber \mathbf{K} is shorthand for (γ_0, α, ν) and $\tilde{\mathbf{x}}$

denotes position in a coordinate system fixed to the cascade being analyzed (rotor or stator) and replaces Glegg's coordinates. For later use, the inverse of Equation 16 is

$$W(\mathbf{K}, \tilde{\omega}) = \frac{1}{(2\pi)^4} \iint w(\tilde{\mathbf{x}}, t) e^{-i(\mathbf{K} \cdot \tilde{\mathbf{x}} - \tilde{\omega}t)} d\tilde{\mathbf{x}} dt \quad (17)$$

With the application of Equation 17 to Equation 2, we can generalize Glegg's potential immediately to

$$\tilde{\phi}^{\pm}(\tilde{\mathbf{x}}, t) = \pm \frac{\pi c^2}{\beta s_e} \iint W(\mathbf{K}, \tilde{\omega}) \sum_{k=-\infty}^{\infty} \frac{\zeta_k^{\pm} D(\lambda_k^{\pm})}{\sqrt{\kappa_e^2 - f_k^2}} e^{i[-\lambda_k^{\pm} \tilde{x} + (\lambda_k^{\pm} \frac{d}{h} + \frac{\sigma - 2\pi k}{h}) \tilde{y} + \nu \tilde{z} - \tilde{\omega}t]} d\mathbf{K} d\tilde{\omega} \quad (18)$$

where the tilde on $\tilde{\phi}^{\pm}$ means that the expression for potential applies in the cascade-fixed frame.

4.4 Transformation to Stationary Coordinate System

We are interested in computing the spectrum of sound power scattered by the cascade. The starting point is the expression for the acoustic energy flux vector applicable to waves in a uniformly moving medium with mean properties given by the density ρ_o , speed of sound a , and velocity \mathbf{U} (ref. 8)

$$\mathbf{I} = \left(\frac{p}{\rho_o} + \mathbf{U} \cdot \mathbf{u} \right) (\rho_o \mathbf{u} + \mathbf{U} p') \quad (19)$$

This is the time dependent power per unit area in terms of the acoustic pressure, density, and velocity, p , p' , and \mathbf{u} . Since it depends on the mean velocity \mathbf{U} , it must be computed in the stationary reference frame (fixed with respect to the duct and observer) whereas Glegg's expressions for the scattered acoustic field apply in a frame fixed to the cascade. The coordinate shift, expressed in duct coordinates (with subscript d in Figure 4), is $\tilde{y}_d = y_d - \Omega R t$. Parameter R is the effective radius of the source and is also used for scaling later in the derivation. The transformation matrix Q defined in Section 3 rotates this to Glegg's system so that the coordinate increments for the transformation, $\tilde{\mathbf{x}} = \mathbf{x} + \Delta \tilde{\mathbf{x}}$, to the stator frame are

$$\begin{bmatrix} \Delta \tilde{x} \\ \Delta \tilde{y} \\ \Delta \tilde{z} \end{bmatrix} = \begin{bmatrix} & & \\ & Q & \\ & & \end{bmatrix} \times \begin{bmatrix} 0 \\ -\Omega R t \\ 0 \end{bmatrix} = - \begin{bmatrix} Q_{12} \\ Q_{22} \\ Q_{32} \end{bmatrix} \Omega R t \quad (20)$$

Adding these deltas in the exponent of Equation 18 results in the frequency shift

$$\omega_k = -[(-Q_{12} + \frac{d}{h} Q_{22}) \lambda_k^{\pm} + Q_{22} (\frac{\sigma - 2\pi k}{h}) + Q_{32} \nu] \Omega R \quad (21)$$

However, by use of Equation 12, the first 2 terms cancel, leaving

$$\omega_k = -[(\frac{\sigma - 2\pi k}{g}) + Q_{32} \nu] \Omega R \quad (22)$$

An alternative expression for ω_k can be obtained by inserting $\sigma = \gamma_o d + \alpha h$ for interblade phase angle and by noting that $2\pi R/g = B$ is the blade count in the rotor (or vane count in the stator) and by again using Equation 12.

$$\omega_k = -[Q_{12} \gamma_o + Q_{22} \alpha + Q_{32} \nu] \Omega R + kB\Omega \quad (23)$$

In the stationary frame, the acoustic potential is now

$$\phi^{\pm} = \pm \frac{\pi c^2}{\beta s_e} \iint W(\mathbf{K}, \tilde{\omega}) \sum_{k=-\infty}^{\infty} \frac{\zeta_k^{\pm} D(\lambda_k^{\pm})}{\sqrt{k_e^2 - f_k^2}} e^{i[-\lambda_k^{\pm} x + (\lambda_k^{\pm} \frac{d}{h} + \frac{\sigma - 2\pi k}{h}) y + vz - (\tilde{\omega} - \omega_k) t]} d\mathbf{K} d\tilde{\omega} \quad (24)$$

expressed as an integral over the turbulence wavenumber vector \mathbf{K} and the turbulence frequency $\tilde{\omega}$. Recall that $\tilde{\omega}$ is turbulence frequency *in the rotor frame*; this form is convenient for now but will eventually be replaced by one with integration over observer frequency to obtain the desired spectrum. Coordinates x , y , and z are the same as Glegg's for stator problems and are parallel to Glegg's (but moving) for rotor problems.

4.3 Acoustic Intensity

The expression for power flux in Equation 19 can be written in terms of potential using Equations 7 as follows

$$\mathbf{I} = -\rho_o \frac{\partial \phi}{\partial t} \left(\nabla \phi - \frac{\mathbf{U}}{a^2} \frac{D\phi}{Dt} \right) \quad (25)$$

For convenience in the ensuing manipulations, we can rewrite this as

$$\mathbf{I} = -\rho_o \frac{\partial \phi^*}{\partial t} \left(\nabla \phi - \frac{\mathbf{U}}{a^2} \frac{D\phi}{Dt} \right) \quad (26)$$

where * denotes complex conjugate. This is permitted because the potential expressed in Equation 24 is pure real as a result of using a double sided summation and double sided integrals. (The imaginary parts in the upper and lower halves of the summation and integration ranges cancel.) There is no need to imply "real part of" with the notation. Thus, since ϕ is pure real, it follows that $\phi = \phi^*$.

To find the acoustic power leaving the cascade, we will compute the component of intensity normal to the cascade

$$I^{\pm} = \hat{\mathbf{n}}^{\pm} \cdot \mathbf{I} \quad (27)$$

and then later integrate it over the frontal area of the blade row. Here, $\hat{\mathbf{n}}^{\pm}$ are upstream/downstream unit vectors normal to planes containing the cascade leading edges or trailing edges

$$\hat{\mathbf{n}}^{\pm} = \pm \left(-\frac{h}{s}, \frac{d}{s}, 0 \right) \quad (28)$$

Formally, Equations 26 and 27 must be evaluated in the coordinate system fixed relative to the observer (or stator) and it is helpful to establish the role of blade row motion in the required dot products and derivatives. For example, $\partial \phi^* / \partial t$ yields $i(\tilde{\omega} - \omega_k)$, which explicitly contains the frequency shift due to the relative motion of the rotor. $\hat{\mathbf{n}}^{\pm} \cdot \nabla$ is the same in the rotor and stator frames. $\hat{\mathbf{n}}^{\pm} \cdot \mathbf{U}$ can be evaluated in the rotor frame since the relative motion is perpendicular to $\hat{\mathbf{n}}^{\pm}$. Finally, since $D\phi/Dt$ is the convective derivative, it must give the same result regardless of coordinate system used for its evaluation. Hence, $\hat{\mathbf{n}}^{\pm} \cdot \left(\nabla \phi - \frac{\mathbf{U}}{a^2} \frac{D\phi}{Dt} \right)$ might as well be evaluated in the rotor frame since the process is easier. The result is

$$\begin{aligned}
I^{\pm} = & \frac{\pm \rho_o \pi^2 c^4}{\beta^2 s_e^2} \iiint \int W^*(\mathbf{K}, \tilde{\omega}) W(\mathbf{K}', \tilde{\omega}') \sum_k \sum_{k'} (\tilde{\omega} - \omega_k) \frac{\zeta_k^{\pm} \zeta_{k'}^{\pm} D^*(\lambda_k^{\pm}) D(\lambda_{k'}^{\pm})}{\sqrt{\kappa_e^2 - f_k^2} \sqrt{\kappa_e'^2 - f_{k'}^2}} \\
& \times \left\{ \frac{h}{s} \lambda_{k'}^{\pm} + \frac{d}{s} \left(\lambda_{k'}^{\pm} \frac{d}{h} + \frac{\sigma' - 2\pi k'}{h} \right) - \frac{h}{s} \frac{U}{a^2} (\tilde{\omega}' + U \lambda_{k'}^{\pm} - v' W) \right\} \\
& \times e^{-i\{-(\lambda_k^{\pm} - \lambda_{k'}^{\pm})x + [(\lambda_k^{\pm} \frac{d}{h} + \frac{\sigma - 2\pi k}{h}) - (\lambda_{k'}^{\pm} \frac{d}{h} + \frac{\sigma' - 2\pi k'}{h})]y + (v - v')z - [(\tilde{\omega} - \omega_k) - (\tilde{\omega}' - \omega_{k'})]t\}} \\
& \times d\mathbf{K} d\mathbf{K}' d\tilde{\omega} d\tilde{\omega}'
\end{aligned} \tag{29}$$

where now the sums and integrals are over the limited ranges of k and k' and wavenumbers corresponding to cut on (energy carrying) modes. Glegg's found that the term in curly brackets $\{ \}$ is equal to $\frac{\pm \beta s_c}{s} \sqrt{\kappa_e'^2 - f_{k'}^2}$, which simplifies Equation 29 considerably. Since we are dealing with turbulence statistics, we take the expected value of both sides, bringing Equation 29 to

$$\begin{aligned}
\langle I^{\pm} \rangle = & \frac{\rho_o \pi^2 c^4}{\beta s s_e} \iiint \int \langle W^*(\mathbf{K}, \tilde{\omega}) W(\mathbf{K}', \tilde{\omega}') \rangle \sum_k \sum_{k'} (\tilde{\omega} - \omega_k) \frac{\zeta_k^{\pm} \zeta_{k'}^{\pm} D^*(\lambda_k^{\pm}) D(\lambda_{k'}^{\pm})}{\sqrt{\kappa_e^2 - f_k^2}} \\
& \times e^{-i\{-(\lambda_k^{\pm} - \lambda_{k'}^{\pm})x + [(\lambda_k^{\pm} \frac{d}{h} + \frac{\sigma - 2\pi k}{h}) - (\lambda_{k'}^{\pm} \frac{d}{h} + \frac{\sigma' - 2\pi k'}{h})]y + (v - v')z - [(\tilde{\omega} - \omega_k) - (\tilde{\omega}' - \omega_{k'})]t\}} \\
& \times d\mathbf{K} d\mathbf{K}' d\tilde{\omega} d\tilde{\omega}'
\end{aligned} \tag{30}$$

Equation 30 represents power per unit area of cascade face. It is still a function of the space variables x , y , z and time. For further simplification, we will analyze the upwash spectrum $\langle W^*(\mathbf{K}, \tilde{\omega}) W(\mathbf{K}', \tilde{\omega}') \rangle$ in the next section where we show that the expected value operation produces delta functions that enable some of the integrals in Equation 30.

4.4 Reduce Upwash Spectrum to Standard Form for Turbulence Spectrum

In this section we examine the flows typical of fans and develop an expression for $\langle W^*(\mathbf{K}, \tilde{\omega}) W(\mathbf{K}', \tilde{\omega}') \rangle$ in terms of a 3D turbulence spectrum while retaining as much generality as possible with respect to inhomogeneity and anisotropy. We will address the most difficult type of inhomogeneity, namely the rotor wake entering the stator, and the other applications (duct boundary layer/rotor interaction, etc.) will follow. Figure 7 (at the left) is a view looking radially in the fan indicating the discrete nature of the wakes and the stator vanes. At the right is an axial view indicating a band of turbulence, so that we must deal with inhomogeneity in the radial direction.

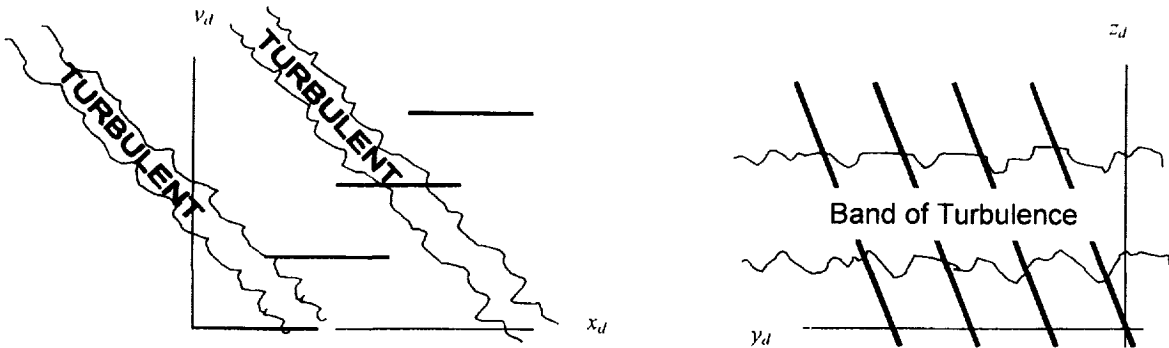


Figure 7. Sketches showing types of inhomogeneity in wakes of rotor entering the stator. Left: view along radius. Right: view along fan axis.

The procedure for evaluating $\langle W^*W \rangle$ is to substitute the inverse transforms from Equation 17 and perform some of the integrals using generalized function theory. Thus,

$$\langle W^*(\mathbf{K}, \tilde{\omega})W(\mathbf{K}', \tilde{\omega}') \rangle = \frac{1}{(2\pi)^8} \iiint \iiint \langle w(\tilde{\mathbf{x}}, t)w(\tilde{\mathbf{x}}', t') \rangle e^{i(\mathbf{K} \cdot \tilde{\mathbf{x}} - \tilde{\omega}t)} e^{-i(\mathbf{K}' \cdot \tilde{\mathbf{x}}' - \tilde{\omega}'t')} d\tilde{\mathbf{x}} d\tilde{\mathbf{x}}' dt dt' \quad (31)$$

At this point we adopt Taylor's hypothesis, treating the turbulence as a frozen gust pattern convected past the cascade. We use the notation \tilde{w} for the frozen turbulence field, which is time-independent in the fluid-fixed frame. Its convection in the x_o direction (see Figure 4) would normally be expressed as $w(\tilde{\mathbf{x}}, t) = \tilde{w}(x_o - U_o t, y_o, z_o)$. However, at this point we employ a device for the treatment of inhomogeneity. We insert a random time offset T representing the fact that we do not know what point in the wake passing cycle corresponds to $t = 0$. Thus, we write (noting that $z_o = z_d$)

$$w(\tilde{\mathbf{x}}, t) = \tilde{w}[x_o - U_o(t - T), y_o, z_d] \quad (32)$$

Random variable T eventually disappears from the equations. Now we display the coordinates x_o, y_o, z_d explicitly in the integrals

$$\langle W^*W \rangle = \frac{1}{(2\pi)^8} \iiint \iiint \iiint \iiint \iiint \langle \tilde{w}[x_o - U_o(t - T), y_o, z_d] \tilde{w}[x'_o - U_o(t' - T), y'_o, z'_d] \rangle \times e^{i(k_x x_o + k_y y_o + k_z z_d - \tilde{\omega}t)} e^{-i(k'_x x'_o + k'_y y'_o + k'_z z'_d - \tilde{\omega}'t')} dx_o dy_o dz_d dx'_o dy'_o dz'_d dt dt' \quad (33)$$

To proceed, we first shift back to fluid-fixed coordinates via $x_o = \tilde{x} + U_o t$ and $x'_o = \tilde{x}' + U_o t'$. Then we change from using 2 independent points to represent the function (e.g. y_o and y'_o , etc.) to an "anchor" point and a spacing (e.g. y_o and s_y) via the following coordinate shifts.

$$\begin{aligned} \tilde{x}' &= \tilde{x} + s_x \\ y'_o &= y_o + s_y \\ z'_d &= z_d + s_z \\ t' &= t + \tau \end{aligned} \quad (34)$$

In Equation 33, k_x, k_y, k_z are associated with the x_o, y_o, z_d axes. With these substitutions,

$$\begin{aligned} \langle W^*W \rangle &= \frac{1}{(2\pi)^8} \iiint \iiint \iiint \iiint \iiint \langle \tilde{w}(\tilde{x} + U_o T, y_o, z_d) \tilde{w}(\tilde{x} + s_x + U_o T, y_o + s_y, z_d + s_z) \rangle \\ &\times e^{-i(k'_x s_x + k'_y s_y + k'_z s_z)} e^{i(k_z - k'_z)z_d} e^{i(k_x - k'_x)\tilde{x}} e^{i(k_y - k'_y)y_o} \\ &\times e^{i[(k_x U_o - \tilde{\omega}) - (k'_x U_o - \tilde{\omega}')]\tau} e^{-i(k'_x U_o - \tilde{\omega}')\tau} d\tilde{x} dy_o dz_d ds_x ds_y ds_z dt d\tau \end{aligned} \quad (35)$$

There follows now a critical step regarding inhomogeneity of the turbulence. The expected value of the velocity product on the right side of Equation 35 is expressed as a function of the fluid-fixed position variables \tilde{x} and y_o , as if we knew the $t = 0$ point for the velocity pattern. However, recall that we inserted the random variable T to represent the fact that we do not know this point. Hence, if the expected value symbol $\langle \rangle$ denotes an ensemble average, then the ensemble is all values of T in a blade passing period. Since these are equally probable, the average is independent of \tilde{x} . Once we have averaged out this \tilde{x} dependence, it is easy to see that the expected value $\langle \tilde{w}\tilde{w} \rangle$ is also

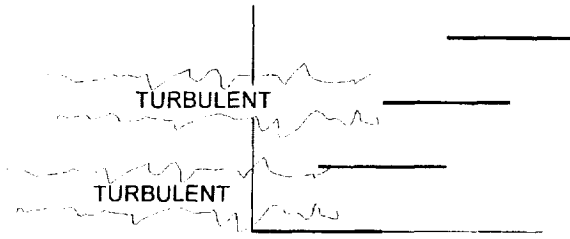


Figure 8. Sketch showing degenerate case not covered by analysis.

independent of y_o (but still dependent on the radial coordinate z_d). Note that, if the 2 blade rows were not in relative motion, then the left side of Figure 7 would look like the sketch in Figure 8. In this case, the ensemble average would not be independent of the transverse coordinate and the ensuing analysis would have to be modified.

$\langle \tilde{w}\tilde{w} \rangle$ as the velocity covariance function

In light of the above discussion, we recognize

$$\overline{\mathfrak{R}}(\mathbf{s}, z_d) = \langle \tilde{w}(\mathbf{x})\tilde{w}(\mathbf{x} + \mathbf{s}) \rangle \quad (36)$$

where the overbar on $\overline{\mathfrak{R}}$ denotes the averaging just discussed. It is explicitly shown to be dependent on z_d and, by implication, independent of \tilde{x} and y_o . With this notation

$$\begin{aligned} \langle W^*W \rangle = & \int \left[\frac{1}{(2\pi)^3} \iiint \overline{\mathfrak{R}}(\mathbf{s}, z_d) e^{-i(k'_x s_x + k'_y s_y + k'_z s_z)} ds_x ds_y ds_z \right] e^{i(k_z - k'_z)z_d} dz_d \\ & \times \frac{1}{(2\pi)^5} \int e^{i(k_x - k'_x)\tilde{x}} d\tilde{x} \int e^{i(k_y - k'_y)y_o} dy_o \int e^{i[(k_x U_o - \tilde{\omega}) - (k'_x U_o - \tilde{\omega}')]t} dt \int e^{-i(k'_x U_o - \tilde{\omega}')\tau} d\tau \end{aligned} \quad (37)$$

The expression in square brackets [] is an extension for radial-dependence of the standard 3D Fourier transform (Ref. 9) defining the turbulence spectrum function

$$\overline{\phi}_{22}(\mathbf{K}', z_d) = \frac{1}{(2\pi)^3} \iiint \overline{\mathfrak{R}}(\mathbf{s}, z_d) e^{-i\mathbf{K}' \cdot \mathbf{s}} ds \quad (38)$$

The integrals on the bottom line of Equation 37 are all delta functions so that we arrive at

$$\langle W^*W \rangle = \frac{1}{2\pi} \delta(k_x - k'_x) \delta(k_y - k'_y) \delta(\tilde{\omega} - \tilde{\omega}') \delta(k'_x U_o - \tilde{\omega}') \int \overline{\phi}_{22}(\mathbf{K}', z_d) e^{i(k_z - k'_z)z_d} dz_d \quad (39)$$

Because the \tilde{x}, y_o, z_d and x_d, y_d, z_d systems share an axis, $\delta(k_x - k'_x) \delta(k_y - k'_y)$ specifies a point in the k_x, k_y plane that can just as well be denoted by $\delta(k_{xd} - k'_{xd}) \delta(k_{yd} - k'_{yd})$. Hence, Equation 39 can be written alternatively

$$\langle W^*W \rangle = \frac{1}{2\pi} \delta(k_{xd} - k'_{xd}) \delta(k_{yd} - k'_{yd}) \delta(\tilde{\omega} - \tilde{\omega}') \delta(k'_x U_o - \tilde{\omega}') \int \overline{\phi}_{22}(\mathbf{K}', z_d) e^{i(k_z - k'_z)z_d} dz_d \quad (40)$$

To simplify notation, we have left the argument of the last delta function unchanged but note that

$$k'_x = k'_{xd} \cos \theta + k'_{yd} \sin \theta \quad (41)$$

4.5 Integral of Intensity for Sound Power

We can now insert the expression, just derived, for the generalized upwash spectrum $\langle W^*W \rangle$ into Equation 30 for intensity and then integrate over planes parallel to the face of the cascade according to $\Pi^\pm = \langle I^\pm \rangle dA$ to get sound power upstream and downstream.

Combining Equations 30 and 40 and performing the $\tilde{\omega}'$ integral give

$$\begin{aligned} \langle I^\pm \rangle &= \frac{\rho_o \pi^2 c^4}{2\pi \beta s s_e} \iiint \delta(k_{xd} - k'_{xd}) \delta(k_{yd} - k'_{yd}) \delta(k'_x U_o - \tilde{\omega}) \int \bar{\phi}_{22}(\mathbf{K}', z_d) e^{i(k_z - k'_z)z_d} dz_d \\ &\times \sum_k \sum_{k'} (\tilde{\omega} - \omega_k) \frac{\zeta_k^\pm \zeta_{k'}^\pm D^*(\lambda_k^\pm) D(\lambda_{k'}^\pm)}{\sqrt{\kappa_e^2 - f_k^2}} \\ &\times e^{-i\{(\lambda_k^\pm - \lambda_{k'}^\pm)x + [(\lambda_k^\pm \frac{d}{h} + \frac{\sigma - 2\pi k}{h}) - (\lambda_{k'}^\pm \frac{d}{h} + \frac{\sigma' - 2\pi k'}{h})]y + (v - v')z + (\omega_k - \omega_{k'})t\}} d\mathbf{K} dk' d\tilde{\omega} \end{aligned} \quad (42)$$

Integration over the face of the cascade is best done in the “hat” coordinates of Figure 9 in which the \hat{y}, \hat{z} plane contains the leading edges of the cascade and \hat{y} is the tangential coordinate (at constant radius) coincident with the y_d axis. Appendix B shows that rotation of the x, y, z system into the “hat” system changes the long exponential in Equation 42 to the following (in which we have used the fact that $k_{yd} = \hat{k}_{yd}$)

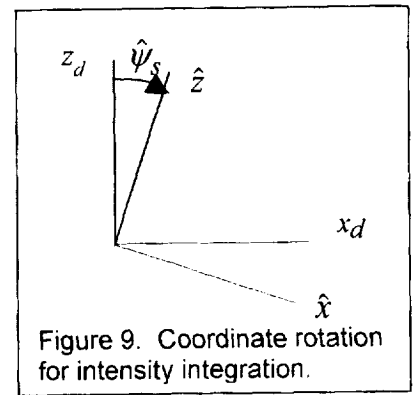


Figure 9. Coordinate rotation for intensity integration.

$$e^{-i\{(\hat{k}_{xk}^a - \hat{k}_{xk'}^a)\hat{x} + [(k_{yd} - k'_{yd}) - \frac{2\pi}{g}(k - k')]\hat{y} + [(\hat{k}_{zd} - \hat{k}'_{zd}) - \frac{2\pi \hat{Q}_{23}}{h}(k - k')]\hat{z} - [(k_{yd} - k'_{yd})R - (k - k')B]\Omega t\}} \quad (43)$$

It will be seen below that the form of the axial wavenumber of the response waves \hat{k}_{xk}^a need not be known for the derivation; we only need know that it depends on k and the excitation wavenumber. Recognizing that the primed wavenumber vector differential can be expanded as $d\mathbf{K}' = dk'_{xd} dk'_{yd} dk'_{zd}$, we can replace the long exponential in Equation 42 with Equation 43 and perform the k'_{yd} integration via the delta function $\delta(k_{yd} - k'_{yd})$

$$\begin{aligned} \langle I^\pm \rangle &= \frac{\rho_o \pi^2 c^4}{2\pi \beta s s_e} \iiint \delta(k_{xd} - k'_{xd}) \delta(k'_x U_o - \tilde{\omega}) \int \bar{\phi}_{22}(\mathbf{K}', z_d) e^{i(k_z - k'_z)z_d} dz_d \\ &\times \sum_k \sum_{k'} (\tilde{\omega} - \omega_k) \frac{\zeta_k^\pm \zeta_{k'}^\pm D^*(\lambda_k^\pm) D(\lambda_{k'}^\pm)}{\sqrt{\kappa_e^2 - f_k^2}} \\ &\times e^{-i\{(\hat{k}_{xk}^a - \hat{k}_{xk'}^a)\hat{x} - \frac{2\pi}{g}(k - k')\hat{y} + [(\hat{k}_{zd} - \hat{k}'_{zd}) - \frac{2\pi \hat{Q}_{23}}{h}(k - k')]\hat{z} - (k - k')B\Omega t\}} d\mathbf{K} dk'_{xd} dk'_{zd} d\tilde{\omega} \end{aligned} \quad (44)$$

Now, we can do the first step in the area integration, namely the integration over the \hat{y} coordinate. To obtain the desired sound power, we integrate in this direction over B blades (or vanes), or for a distance of Bg where g is the gap between blades. This integral involves

$$\int_0^{Bg} e^{-i\frac{2\pi}{g}(k-k')\hat{y}} d\hat{y} = Bg\delta_{kk'} \quad (45)$$

Kroncker delta $\delta_{kk'}$ enables the k' summation, leaving

$$\begin{aligned} \int \langle I^\pm \rangle d\hat{y}_d &= \frac{\rho_o Bg\pi^2 c^4}{2\pi\beta s s_e} \iiint \delta(k_{xd} - k'_{xd}) \delta(k'_x U_o - \tilde{\omega}) \int \bar{\phi}_{22}(\mathbf{K}', z_d) e^{i(k_z - k'_z)z_d} dz_d \\ &\times \sum_k (\tilde{\omega} - \omega_k) \frac{\zeta_k^\pm \zeta_k'^\pm D^*(\lambda_k^\pm) D(\lambda_k'^\pm)}{\sqrt{\kappa_e^2 - f_k^2}} e^{-i[(\hat{k}_{xk}^a - \hat{k}'_{xk}^a)\hat{x} + (\hat{k}_{zd} - \hat{k}'_{zd})\hat{z}]} d\mathbf{K} dk'_{xd} dk'_{zd} d\tilde{\omega} \end{aligned} \quad (46)$$

Note that the time dependence has disappeared. We want to do the k'_{xd} integration next via the delta function $\delta(k_{xd} - k'_{xd})$. However, the wavenumbers in the exponential are in a different coordinate system. The rotation for the wavenumbers is the same as for the coordinates shown in Figure 9 from which we determine

$$\hat{k}_{zd} - \hat{k}'_{zd} = (k_{xd} - k'_{xd}) \sin \hat{\psi}_s + (k_{zd} - k'_{zd}) \cos \hat{\psi}_s \quad (47)$$

since $k_{yd} = \hat{k}_{yd}$ is common to both systems. Now we can do the k'_{xd} integration with the result

$$\begin{aligned} \int \langle I^\pm \rangle d\hat{y}_d &= \frac{\rho_o Bg\pi^2 c^4}{2\pi\beta s s_e} \iiint \delta(k_x U_o - \tilde{\omega}) \int \bar{\phi}_{22}(\mathbf{K}', z_d) e^{i(k_z - k'_z)z_d} dz_d \\ &\times \sum_k (\tilde{\omega} - \omega_k) \frac{\zeta_k^\pm \zeta_k'^\pm D^*(\lambda_k^\pm) D(\lambda_k'^\pm)}{\sqrt{\kappa_e^2 - f_k^2}} e^{-i[(\hat{k}_{xk}^a - \hat{k}'_{xk}^a)\hat{x} + (k_{zd} - k'_{zd}) \cos \hat{\psi}_s \hat{z}]} d\mathbf{K} dk'_{zd} d\tilde{\omega} \end{aligned} \quad (48)$$

And we complete the area integration of intensity to get sound power via

$$\Pi^\pm = \iint \langle I^\pm \rangle d\hat{z} \quad (49)$$

We interpret the outer integral as running from $-\infty$ to $+\infty$ so as to capture all of the radiated energy. This integral involves only an exponential and thus produces another delta function

$$\int e^{-i(k_{zd} - k'_{zd})\hat{z} \cos \hat{\psi}_s} d\hat{z} = \frac{2\pi}{\cos \hat{\psi}_s} \delta(k_{zd} - k'_{zd}) \quad (50)$$

The term $\cos \hat{\psi}_s$ in the denominator is in the direction of sweep *increasing* noise. It appears here because sweep increases the length of leading edge exposed to a band of turbulent flow. Later, it will be seen that this undesired tendency will be overcome by the reduction in effective Mach number due to sweep. Equation 50 enables the k'_{zd} integration leading to

$$\Pi^{\pm} = \frac{\rho_o B g \pi^2 c^4}{\beta s s_e \cos \hat{\psi}_s} \int \int \delta(k_x U_o - \tilde{\omega}) \bar{\phi}_{22}(\mathbf{K}, z_d) dz_d \sum_k (\tilde{\omega} - \omega_k) \frac{|\zeta_k^{\pm} D(\lambda_k^{\pm})|^2}{\sqrt{\kappa_e^2 - f_k^2}} d\mathbf{K} d\tilde{\omega} \quad (51)$$

Note that the exponential has disappeared entirely, including the term $(\hat{k}_{xk}^a - \hat{k}_{xk'}^{a'}) \hat{x}$. This occurs because we have arrived at the point where $\mathbf{K}=\mathbf{K}'$ and $k=k'$ so that $\hat{k}_{xk}^a = \hat{k}_{xk'}^{a'}$.

Equation 51 has gap g in the duct system and gap s in the cascade system. This can be eliminated by using the result from Appendix A which shows that

$$\frac{g}{s \cos \hat{\psi}_s} = \frac{1}{\cos \psi_l \cos \psi_s} \quad (52)$$

so that, with a change in order of integration,

$$\Pi^{\pm} = \frac{B \rho_o \pi^2 c^4}{\beta s_e \cos \psi_l \cos \psi_s} \int \int \int \bar{\phi}_{22}(\mathbf{K}, z_d) dz_d \sum_k \delta(k_x U_o - \tilde{\omega}) (\tilde{\omega} - \omega_k) \frac{|\zeta_k^{\pm} D(\lambda_k^{\pm})|^2}{\sqrt{\kappa_e^2 - f_k^2}} d\tilde{\omega} d\mathbf{K} \quad (53)$$

The integration order can be shifted without concern for integration limits if we take all the ranges to be $-\infty$ to $+\infty$ and consider the integrand to be zero whenever the square root in the denominator becomes imaginary (i.e. for cut off waves). Equation 53 represents the upstream and downstream sound power integrated over all frequencies rather than the sound power spectrum. Recall that the frequency integration variable $\tilde{\omega}$ is *source* frequency rather than observer frequency. This can be shifted to an integral over observer frequency ω via

$$\tilde{\omega} = \omega + \omega_k \quad (54)$$

which is now permitted with the ω integral inside the \mathbf{K} integral. But, then, with the infinite limits, the integration order can be changed back again so that the power is in the form

$$\Pi^{\pm} = \int_{-\infty}^{+\infty} \Pi_{\omega}^{\pm} d\omega \quad (55)$$

where

$$\Pi_{\omega}^{\pm} = \frac{B \rho_o \pi^2 c^4 \omega}{\beta s_e \cos \psi_l \cos \psi_s} \int \left[\int \bar{\phi}_{22}(\mathbf{K}, z_d) dz_d \right] \sum_k \delta(k_x U_o - \omega - \omega_k) \frac{|\zeta_k^{\pm} D(\lambda_k^{\pm})|^2}{\sqrt{\kappa_e^2 - f_k^2}} d\mathbf{K} \quad (56)$$

Recall that the Doppler frequency shift from Equation 22 is

$$\omega_k = -\left[\frac{\sigma - 2\pi k}{g} \right] + Q_{32} \nu \Omega R \quad (57)$$

Equation 56 is the spectrum of sound power distributed over observer frequency, as desired. It is expressed as an integral over the wavenumber vector \mathbf{K} of the turbulence. The final delta function

still needs to be dealt with to reduce the wavenumber integration from 3 wavenumber components to 2, but that step is postponed.

Our current form for the spectrum is not efficient for computation because Glegg's D function is inside the integration *and* summation. Another shift in integration variable can be used to move D out from under the sum at the expense of moving the turbulence spectrum under the sum. This is advantageous because $\bar{\phi}_{22}$ will normally be computed from a simple algebraic expression whereas D requires considerable computational effort. Note that $d\mathbf{K}$ can be expressed in various wavenumber coordinate systems but, for the present purposes, it is considered to be $d\mathbf{K}=d\gamma_o d\alpha d\nu$. Also, note in all of the expressions for the acoustic response functions and in the frequency shift ω_k that α always appears with the scattering index k in the combination $\alpha h - 2\pi k$. Thus, if we shift the α wavenumber variable to α' via

$$\alpha h - 2\pi k = \alpha' h \quad (58)$$

we achieve the desired result

$$\Pi_{\omega}^{\pm} = \frac{B\rho_o\pi^2c^4\omega}{\beta s_e \cos\psi_l \cos\psi_s} \iiint \delta(k_x U_o - \omega - \omega_o) \frac{|\zeta_o^{\pm} D(\lambda_o^{\pm})|^2}{\sqrt{\kappa_e^2 - f_o^2}} \sum_k \left[\int \bar{\phi}_{22}(\mathbf{K}, z_d) dz_d \right]_k d\gamma_o d\alpha' d\nu \quad (59)$$

where the scattering index k has disappeared from the frequency shift:

$$\omega_o = -(Q_{12}\gamma_o + Q_{22}\alpha' + Q_{32}\nu)\Omega R \quad (60)$$

The delta function cannot be used for integration until the wavenumber k_x is expressed in the γ_o, α', ν system. Appendix B shows that

$$k_x = \gamma_o \cos\psi_s + \nu \sin\psi_s \quad (61)$$

Substitution of this and Equation 60 into the argument of the delta function gives, with some rearrangement

$$\delta \rightarrow \delta[(U + Q_{12}\Omega R)\gamma_o - (\omega - W\nu) + (Q_{22}\alpha' + Q_{32}\nu)\Omega R] \quad (62)$$

This is functionally equivalent to

$$\delta \rightarrow \frac{1}{U + Q_{12}\Omega R} \delta \left[\gamma_o - \frac{(\omega - W\nu) - (Q_{22}\alpha' + Q_{32}\nu)\Omega R}{U + Q_{12}\Omega R} \right] \quad (63)$$

This enables the γ_o integration, so that finally

$$\Pi_{\omega}^{\pm} = \frac{B\rho_o\pi^2c^4\omega}{\beta s_e (U + Q_{12}\Omega R) \cos\psi_l \cos\psi_s} \iint \frac{|\zeta_o^{\pm} D(\lambda_o^{\pm})|^2}{\sqrt{\kappa_e^2 - f_o^2}} \sum_k \left[\int \bar{\phi}_{22}(\mathbf{K}, z_d) dz_d \right]_k d\alpha' d\nu \quad (64)$$

and, in evaluation of Glegg's acoustic response function, the values used for γ_o and $\tilde{\omega}$ are

$$\gamma_o = \frac{(\omega - Wv) - (Q_{22}\alpha' + Q_{32}v)\Omega R}{U + Q_{12}\Omega R} \quad (65)$$

and

$$\tilde{\omega} = \omega - (Q_{12}\gamma_o + Q_{22}\alpha' + Q_{32}v)\Omega R \quad (66)$$

Finally, recall that in evaluation of the turbulence spectrum that the α wavenumber must be shifted according to

$$\alpha = \alpha' + 2\pi k/h \quad (67)$$

The equations just derived provide the transfer function from the turbulence spectrum as input to the output spectrum of sound power. In the following sections, we establish forms for the turbulence spectrum and non-dimensionalize the equations for coding.



SECTION 5

TURBULENCE SPECTRA FOR BBCASCADE

The theoretical acoustic spectra derived above, when applied to inhomogeneous, anisotropic turbulence, require that the turbulence spectrum be averaged properly in the gapwise direction. If this kind of test data is available, then it should be used. However, for predictions based on theory, turbulence spectra are not yet available for this general kind of flow. Out of necessity BBCascade uses spectra for homogeneous turbulence available from the literature. Thus, the $\bar{\phi}_{22}$ of Section 4 will be replaced simply by ϕ_{22} , as given in this section. Two options are provided: one for isotropic turbulence and one for axi-symmetric turbulence. For the isotropic case, we use Leipmann's spectrum (ref. 10). For axi-symmetric turbulence, we use theory given in a paper by Kerschen and Gliebe (ref. 11). This section presents the algebraic forms of the spectra, shows how to rotate wavenumber coordinates to make the functional dependence of the spectra compatible with the noise equations, and normalizes the spectra for use in the computer code. Both spectra are coded in normalized form Φ_{22} based on the local radius R and the mean flow velocity in the stationary frame U_{stat} . The normalization is defined by

$$\phi_{22} = R^3 U_{stat}^2 \Phi_{22} \quad (68)$$

Wavenumbers will also be normalized based on R so that $K_1 = k_1 R$, etc.

5.1 Liepmann Spectrum

This is one of the standard 3D spectra often used for acoustic and unsteady air loading analysis

$$\phi_{22} = \frac{2\overline{w^2}\Lambda^5}{\pi^2} \frac{k_1^2 + k_3^2}{[1 + \Lambda^2(k_1^2 + k_2^2 + k_3^2)]^3} \quad (69)$$

It applies the velocity component in the "2" direction whose mean square value is $\overline{w^2}$. Λ is the integral scale of the turbulence. Because this is a spectrum for isotropic turbulence, it does not matter how the coordinates are oriented in space except that the "2" direction must be normal to the airfoil surfaces (Glegg's y direction). Since we are free to select the orientation of the other axes, we make the most convenient choice and align the turbulence coordinates with Glegg's x, y, z . Thus, in application of Liepmann's spectrum, we set

$$\begin{aligned} k_1 &= \gamma_0 \\ k_2 &= \alpha \\ k_3 &= \nu \end{aligned} \quad (70)$$

and recall that we have shifted the α integration in Equation 56 according to $\alpha = \alpha' + 2\pi k/h$.

The normalized form for the Liepmann spectrum is

$$\Phi_{22} = \frac{\overline{w^2}}{U_{stat}^2} \frac{2L^3}{\pi^2} \frac{L^2(K_1^2 + K_3^2)}{[1 + L^2(K_1^2 + K_2^2 + K_3^2)]^3} \quad (71)$$

where $L=A/R$. In the Glegg routines, wavenumbers are normalized by chord c so that the parameter $\bar{c} = c/R$ appears in the formulas connecting the cascade wavenumbers and the turbulence wavenumbers:

$$\begin{aligned} K_1 &= \bar{\gamma}_o / \bar{c} \\ K_2 &= \bar{\alpha} / \bar{c} = \alpha' / \bar{c} + kB / Q_{22} \\ K_3 &= \bar{v} / \bar{c} \end{aligned} \quad (72)$$

where for K_2 , we have used $2\pi R/g = B$ and $h/g = Q_{22}$. Glegg's wavenumbers are normalized by chord, i.e. $\bar{\gamma}_o = \gamma_o c$, etc.

5.2 Axi-symmetric Spectrum

When external turbulence is drawn into an engine inlet, it is distorted in the axial direction, producing elongated eddies at low forward speed and flattened eddies at high flight speed. For this kind of flow, Kerschen and Gliebe developed a model for axi-symmetric turbulence ^(ref. 11). They gave the following general form for the axi-symmetric turbulence spectrum

$$\phi_{ij}(\mathbf{k}) = [k^2 \delta_{ij} - k_i k_j] F + [(k^2 - (\mathbf{k} \cdot \lambda)^2) \delta_{ij} - k_i k_j - k^2 \lambda_i \lambda_j + \mathbf{k} \cdot \lambda (\lambda_i k_j + k_i \lambda_j)] G \quad (73)$$

where λ is a unit vector in the direction of symmetry and F and G are given below in terms of the wavenumber component k_a aligned with the symmetry direction and the polar transverse wavenumber component $k_t = \sqrt{k_{ty}^2 + k_{tz}^2}$.

$$F = \frac{2u_a^2}{\pi^2} \frac{\ell_a \ell_t^4}{(1 + \ell_a^2 k_a^2 + \ell_t^2 k_t^2)^3} \quad (74)$$

and

$$G = \left[2 \frac{u_t^2}{u_a^2} - \frac{\ell_t^2}{\ell_a^2} - 1 \right] F \quad (75)$$

The axial and transverse length scales ℓ_a and ℓ_t are independent as are the axial and transverse intensities u_a^2 and u_t^2 . However, they are subject to the restriction

$$2 \frac{u_t^2}{u_a^2} \geq \frac{\ell_t^2}{\ell_a^2} \quad (76)$$

We assume the turbulence symmetry coordinates to have their x axis aligned with the flow in stationary coordinates and their z axis radial. To apply Equation 73 directly in Glegg's cascade coordinates, we must establish the relation between symmetry coordinates of the turbulence and Glegg's cascade coordinates. Transformation from one system to the other involves a sequence of rotations just like those shown in Figure 4 except that the starting coordinates are already rotated about the z_d axis to the θ_s direction. Thus, the rotation matrix \tilde{Q} is the same as Q in

Equation 9 but with θ replaced by $\Delta\theta = -(\theta_s - \theta)$. Then, the transformation of wavenumber components is given by the inverse, i.e.

$$\begin{aligned} k_a &= \tilde{Q}_{11}\gamma_o + \tilde{Q}_{21}\alpha + \tilde{Q}_{31}\nu \\ k_{ly} &= \tilde{Q}_{12}\gamma_o + \tilde{Q}_{22}\alpha + \tilde{Q}_{32}\nu \\ k_{lz} &= \tilde{Q}_{13}\gamma_o + \tilde{Q}_{23}\alpha + \tilde{Q}_{33}\nu \end{aligned} \quad (77)$$

where

$$\begin{aligned} \tilde{Q}_{11} &= \cos\Delta\theta\cos\psi_s + \sin\Delta\theta\sin\psi_l\sin\psi_s \\ \tilde{Q}_{12} &= \sin\Delta\theta\cos\psi_s - \cos\Delta\theta\sin\psi_l\sin\psi_s \\ \tilde{Q}_{13} &= -\cos\psi_l\sin\psi_s \\ \tilde{Q}_{21} &= -\sin\Delta\theta\cos\psi_l \\ \tilde{Q}_{22} &= \cos\Delta\theta\cos\psi_l \\ \tilde{Q}_{32} &= -\sin\psi_l \\ \tilde{Q}_{31} &= \cos\Delta\theta\sin\psi_s - \sin\Delta\theta\sin\psi_l\cos\psi_s \\ \tilde{Q}_{32} &= \sin\Delta\theta\sin\psi_s + \cos\Delta\theta\sin\psi_l\cos\psi_s \\ \tilde{Q}_{33} &= \cos\psi_l\cos\psi_s \end{aligned} \quad (78)$$

$\mathbf{k}\cdot\boldsymbol{\lambda}$ in Equation 73 is most easily computed in the turbulence symmetry coordinates where $\boldsymbol{\lambda}=(1, 0, 0)$. Then $\mathbf{k}\cdot\boldsymbol{\lambda} = k_a$. Otherwise in Equation 73, we need $\boldsymbol{\lambda}$ in cascade coordinates, i. e.

$$\begin{bmatrix} \lambda_x \\ \lambda_y \\ \lambda_z \end{bmatrix} = \begin{bmatrix} & & \\ & \tilde{Q} & \\ & & \end{bmatrix} \times \begin{bmatrix} 1 \\ 0 \\ 0 \end{bmatrix} = \begin{bmatrix} \tilde{Q}_{11} \\ \tilde{Q}_{21} \\ \tilde{Q}_{31} \end{bmatrix} \quad (79)$$

Now, we apply Equation 73 directly in Glegg's coordinates, where $k_1=\gamma_o$, $k_2=\alpha$, and $k_3=\nu$

$$\phi_{22} = (k^2 - \alpha^2)F + [(k^2 - k_a^2) - \alpha^2 - k^2\lambda_y^2 + k_a(2\lambda_y\alpha)]G \quad (80)$$

where $k^2 = \gamma_o^2 + \alpha^2 + \nu^2$. Substituting $\lambda_y = \tilde{Q}_{21}$ and re-arranging, we find

$$\phi_{22} = (\gamma_o^2 + \nu^2)F + [(1 - \tilde{Q}_{21}^2)k^2 - k_a^2 - \alpha^2 + 2k_a\tilde{Q}_{21}\alpha]G \quad (81)$$

The non-dimensional forms for programming the axi-symmetric spectrum are

$$\Phi_{22} = (\bar{\gamma}_o^2 + \bar{\nu}^2)\bar{F} / \bar{c}^2 + [(1 - \tilde{Q}_{21}^2)K^2 - K_a^2 - \bar{\alpha}^2 / \bar{c}^2 + 2K_a\tilde{Q}_{21}\bar{\alpha} / \bar{c}] \bar{G} \quad (82)$$

$$\bar{F} = \frac{2}{\pi^2} \frac{u_a^2}{U_{stat}^2} \frac{L_a L_t^4}{(1 + L_a^2 K_a^2 + L_t^2 K_t^2)^3} \quad (83)$$

and

$$\bar{G} = \left[2 \frac{u_t^2 / U_{stat}^2}{u_a^2 / U_{stat}^2} - \frac{L_t^2}{L_a^2} - 1 \right] \bar{F} \quad (84)$$

with the requirement that

$$2 \frac{u_t^2 / U_{stat}^2}{u_a^2 / U_{stat}^2} \geq \frac{L_t^2}{L_a^2} \quad (85)$$

The normalized wavenumbers are

$$\begin{aligned} K_a &= (\tilde{Q}_{11}\bar{\gamma}_o + \tilde{Q}_{21}\bar{\alpha} + \tilde{Q}_{31}\bar{v}) / \bar{c} \\ K_{ty} &= (\tilde{Q}_{12}\bar{\gamma}_o + \tilde{Q}_{22}\bar{\alpha} + \tilde{Q}_{32}\bar{v}) / \bar{c} \\ K_{tz} &= (\tilde{Q}_{13}\bar{\gamma}_o + \tilde{Q}_{23}\bar{\alpha} + \tilde{Q}_{33}\bar{v}) / \bar{c} \end{aligned} \quad (86)$$

and finally,

$$K_t^2 = K_{ty}^2 + K_{tz}^2 \quad (87)$$

and

$$K^2 = K_a^2 + K_t^2 = (\bar{\gamma}_o^2 + \bar{\alpha}^2 + \bar{v}^2) / \bar{c}^2 \quad (88)$$

SECTION 6

APPLICATION OF THEORY & FORMULAS FOR CODE BBCASCADE

To prepare the theoretical equations from Sections 4 and 5 for programming, we first write them in non-dimensional form and then modify them for spectrum level in decibels. Also, we address the radial integral over the turbulence field and limits for the wavenumber integral corresponding to cut on waves.

6.1 Non-dimensional Forms

To obtain power in any band of frequency, we should integrate the spectral density of Equation 64 over a range of ω . For small enough bandwidth, however, we will simply multiply by $\Delta\omega$ and then multiply by 2 to account for negative frequencies. We call this integrated quantity PWR^\pm which, with the above definitions applied to Equation 64, becomes

$$PWR^\pm = \frac{2\pi^2 BM_{stat}^2 \rho_o a^2 Ra}{\beta \bar{s}_e (M + Q_{12} M_T) Q_{33}} \bar{\omega} \Delta\bar{\omega} \iint F^\pm(\bar{\alpha}, \bar{\nu}) \sum_k \left[\int \Phi_{22} dz_o \right] d\bar{\alpha}' d\bar{\nu} \quad (89)$$

where $M_T = \Omega R/a$ is tip (or local radius) rotational Mach number, and where the cascade power response function (in non-dimensional form and without the constants leading Equation 64) is

$$F^\pm(\bar{\alpha}, \bar{\nu}) = \frac{\left| \zeta_0^\pm cD(\lambda_0^\pm) \right|^2}{\sqrt{c^2 (\kappa_e^2 - f_0^2)}} \quad (90)$$

We will do the radial integration over the turbulence (the inside integral) in a strip sense so that that integral can be approximated by $\Phi_{22} \Delta R$. The result for one strip of width ΔR is

$$PWR^\pm = \frac{2\pi^2 BM_{stat}^2 \bar{\omega} \Delta\bar{\omega}}{\beta \bar{s}_e (M + Q_{12} M_T) Q_{33}} \left[\rho_o a^2 R \Delta R a \right] \iint F^\pm(\bar{\alpha}, \bar{\nu}) \sum_k \Phi_{22} d\bar{\alpha}' d\bar{\nu} \quad (91)$$

where $\bar{\omega} = \omega R/a$. The quantity in square brackets has the dimensions of power; the remainder of the expression is dimensionless.

Power level in decibels is given by

$$PWL^\pm = 10 \log_{10} \left[\frac{PWR^\pm}{PWR_{REF}} \right] \quad (92)$$

where the power reference is 10^{-12} watts or

$$PWR_{REF} = 0.73756 \times 10^{-12} \text{ ft lb / sec} \quad (93)$$

The result is that our working formula for the computer code is

$$\frac{PWR^\pm}{PWR_{REF}} = \frac{2\pi^2 B M_{stat}^2 \bar{\omega} \Delta \bar{\omega}}{\beta \bar{s}_e (M + Q_{12} M_T) Q_{33}} \left[\frac{1.4 P_o R \Delta R a}{PWR_{REF}} \right] \iint F^\pm(\bar{\alpha}, \bar{\nu}) \sum_k \Phi_{22} d\bar{\alpha}' d\bar{\nu} \quad (94)$$

We have used $\rho_o a^2 = 1.4 P_o$ where 1.4 is the ratio of specific heats for air and P_o is the ambient pressure.

For use in the Glegg algorithms representing his D function, the non-dimensional chordwise wavenumber from Equation 65

$$\bar{\gamma}_o = \frac{(\hat{\omega} - M_z \bar{\nu}) - (Q_{22} \bar{\alpha}' + Q_{32} \bar{\nu}) M_T}{M + Q_{12} M_T} \quad (95)$$

where $\hat{\omega} = \omega c/a$ is a non-dimensional frequency in the observer frame. The non-dimensional frequency (in cascade-fixed coordinates) from Equation 66 is

$$\frac{\tilde{\omega} c}{a} = \hat{\omega} - (Q_{12} \bar{\gamma}_o + Q_{22} \bar{\alpha}' + Q_{32} \bar{\nu}) M_T \quad (96)$$

and for Glegg's shifted Helmholtz frequency ω_g

$$\frac{\omega_g c}{a} = \frac{(\tilde{\omega} - W \nu) c}{a} = (\hat{\omega} - M_z \bar{\nu}) - (Q_{12} \bar{\gamma}_o + Q_{22} \bar{\alpha}' + Q_{32} \bar{\nu}) M_T \quad (97)$$

where $M_z = W/a$. Glegg's reduced frequency $\bar{\kappa}$ (normalized by chord c) is

$$\bar{\kappa} = \frac{\omega_g c}{a \beta^2} = \frac{\hat{\omega} - M_z \bar{\nu}}{\beta^2} - (Q_{12} \bar{\gamma}_o + Q_{22} \bar{\alpha}' + Q_{32} \bar{\nu}) \frac{M_T}{\beta^2} \quad (98)$$

The remaining items to be dealt with for programming are the limits on the integrals and sum in Equation 94. These are treated in the following sections.

6.2 Integration and Summation Limits

The double integral in Equation 94 is over the $\bar{\alpha}', \bar{\nu}$ wavenumber plane. There is an ellipse in that plane such that wavenumbers inside it correspond to cut on waves and wavenumbers outside correspond to cut off waves. In this section we find the equation for the ellipse and provide a scheme for determining loop limits (do-loops in the code) for the 2 wavenumber integration variables.

Cuton is governed by the square root in Equation 90. When the argument of the square root

$$E = \kappa_e^2 - f_k^2 \quad (99)$$

is positive, the waves are cut on and thus the cuton boundary is given by $E = 0$. We only need to treat $k = 0$, in which case Equations 5 and 6 from the Introduction give

$$\kappa^2 - \frac{v^2}{\beta^2} - \frac{(\sigma + \kappa M d)^2}{s_e^2} = 0 \quad (100)$$

This is the ellipse in the σ, v wavenumber plane shown below in Figure 10.

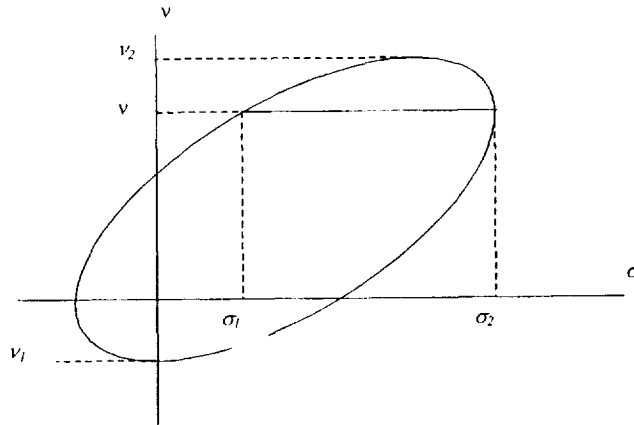


Figure 10. Sketch for discussion of wavenumber integration limits

Solution for the α and v limits for the general rotor case involves algebra too tedious to present here. Instead, we present the derivation for the stator case, which is much simpler, and illustrates the concept. Then, the formulas for the general case are simply presented as documentation for BBCascade.

Limits on Wavenumber Integral for Stator Analysis

Equation 100 can be solved for σ as follows

$$\sigma = -\kappa M d \pm s_e \sqrt{\kappa^2 - v^2/\beta^2} \quad (101)$$

where, from Equations 3 and 5

$$\kappa = \frac{\omega - vW}{a\beta^2} \quad (102)$$

We will use the outside loop for v and integrate over the range of α corresponding to $\sigma_1 < \sigma < \sigma_2$ where

$$\begin{aligned} \sigma_1 &= -\kappa M d - s_e \sqrt{\kappa^2 - v^2/\beta^2} \\ \sigma_2 &= -\kappa M d + s_e \sqrt{\kappa^2 - v^2/\beta^2} \end{aligned} \quad (103)$$

as shown in the sketch. The extremes of v occur when the square roots above are equal to 0, i.e. for

$$v_{1,2} = \frac{\omega/a}{W/a \pm \beta} \quad (104)$$

or in non-dimensional form

$$\begin{aligned}\bar{v}_1 &= \frac{-\hat{\omega}}{\beta - M_o \sin \psi_s} \\ \bar{v}_2 &= \frac{\hat{\omega}}{\beta + M_o \sin \psi_s}\end{aligned}\quad (105)$$

where $\hat{\omega} = \omega c/a$ and $M_o = U_o/a$. Finally, since $\sigma = \gamma_o d + \alpha h$ the range of α corresponding to Equation 103 is given by

$$\begin{aligned}\alpha_1 &= -(\gamma_o + \kappa M) \frac{d}{h} - \frac{s_e}{h} \sqrt{\kappa^2 - v^2 / \beta^2} \\ \alpha_2 &= -(\gamma_o + \kappa M) \frac{d}{h} + \frac{s_e}{h} \sqrt{\kappa^2 - v^2 / \beta^2}\end{aligned}\quad (106)$$

This can be re-arranged and non-dimensionalized as follows:

$$\begin{aligned}\bar{\alpha}_1 &= -(\bar{\kappa} / M) \tan \chi - \sqrt{\beta^2 \bar{\kappa}^2 - \bar{v}^2} / \cos \chi_e \\ \bar{\alpha}_2 &= -(\bar{\kappa} / M) \tan \chi + \sqrt{\beta^2 \bar{\kappa}^2 - \bar{v}^2} / \cos \chi_e\end{aligned}\quad (107)$$

where $\bar{\kappa} = \kappa c$. These are the equations used for the stator analyses in Refs. 2 and 3 before the rotor theory had been completed.

Limits on Wavenumber Integral for General Case

The limits for the rotor case were derived in separate notes and the results are presented here. Limits for v are given by

$$\bar{v}_{1,2} = \frac{\hat{\omega}}{(M_z + M_T Q_{32}) \pm \sqrt{\beta^2 - 2 M M_T Q_{12} - (Q_{12}^2 + Q_{22}^2) M_T^2}} \quad (108)$$

and the α limits for any v in the above range are

$$\begin{aligned}\bar{\alpha}_{1,2} &= \frac{1}{M Q_{22}} \left\{ -(\bar{\omega} Q_{12} + M Q_{32} \bar{v}) + \left(\frac{M + Q_{12} M_T}{\frac{g^2}{s_e^2} A_1^2 - M_T^2} \right) \times \right. \\ &\quad \left. \left[\left(\frac{g^2}{s_e^2} A_1 A_2 - \bar{\omega} M_T \right) \pm \sqrt{\frac{g^2}{s_e^2} \left[(\bar{\omega} A_1 - M_T A_2)^2 - \beta^2 \bar{v}^2 A_1^2 \right] + \beta^2 M_T^2 \bar{v}^2} \right] \right\}\end{aligned}\quad (109)$$

where

$$A_1 = \beta^2 - M M_T Q_{12} \quad (110)$$

and

$$A_2 = \beta^2 Q_{32} \bar{v} - \frac{\omega g^c}{a} M Q_{12} \quad (111)$$

These equations for the wavenumber limits are coded in BBCascade. They can be shown to reduce to the stator results above for $M_T = 0$. Also, they have been tested numerically for correct behavior by one step in $\bar{\alpha}$ or \bar{v} and verifying that the argument of the square root in Equation 90 was negative.

Summation Limits

In the code the sum is initialized by the $k = 0$ term. Then, the k loop runs from 1 to a large number (30). The positive and negative k terms are added in pairs until a convergence criterion is satisfied.

6.3 Sample Calculation – Comparison with ADP Test Data

Figure 11 shows comparisons with scaled sound power spectral data from a model test in a wind tunnel at NASA-Lewis. Note that the noise below 300 Hertz has been traced to sources other than the fan. The stator was modeled with a single geometry and mean flow appropriate for the tip stator station. Turbulence scale and intensity were back-figured to provide a good match between the noise prediction and test data. The scale, Λ , was taken at 3.5% of the radius and the intensity was 2% of the mean flow velocity. Although the turbulence properties are represented simply by the Liepmann spectrum with a single intensity and length scale, the fit is satisfactory. (Issues of turbulence inhomogeneity were discussed above where it was shown that the theoretical equations for sound power presented herein apply equally well to the case of inhomogeneous flow, provided that the turbulence spectrum is formally averaged in the gapwise direction.) The overall spectrum shape in Figure 11 is good and the high frequency slope matches that of the data. Furthermore, the split between the upstream and downstream power is excellent.

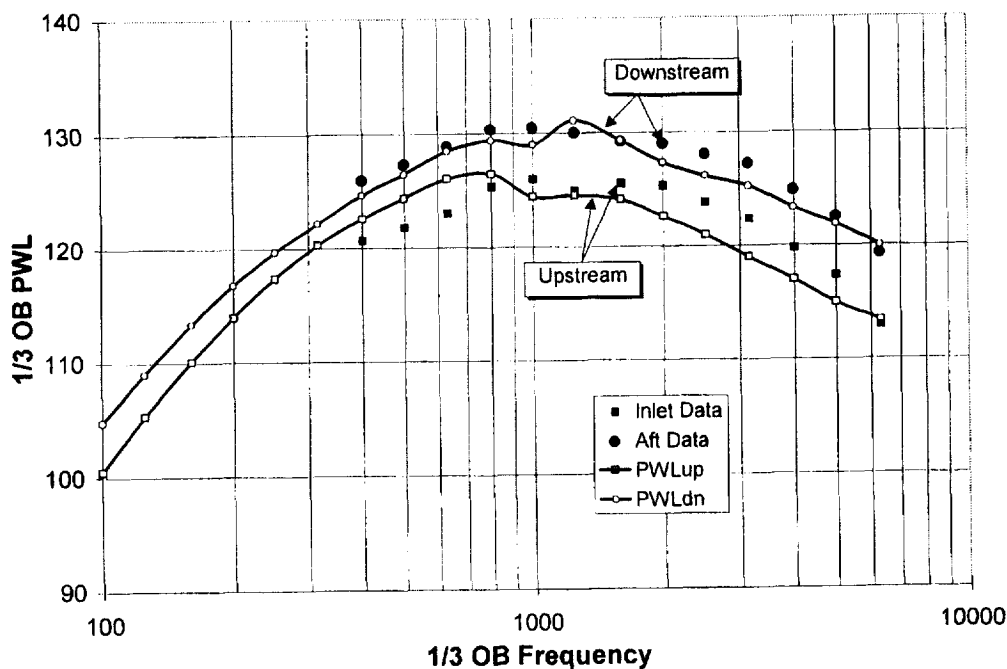


Figure 11. Comparison of theoretical and test noise spectra for scaled model data. Turbulence intensity and scale were chosen for a match to the noise data.



SECTION 7

INTERPRETATION OF THE NOISE EQUATION - SPECTRA OF TURBULENCE AND CASCADE RESPONSE

In the preceding sections we derived equations giving sound power spectra (typified by Figure 11) in terms of the turbulence and cascade response spectra. In this section, before proceeding with the series of noise calculations in Section 8, we examine the behavior of the turbulence and cascade response spectra and how they work together to produce sound. To simplify this as much as possible, we consider the case for a stator with radial vanes. Under these conditions, Equation 56 becomes

$$\Pi_{\omega}^{\pm} = \frac{V \rho_o \pi^2 c^4 \omega \Delta R}{\beta s_e} \iiint \bar{\phi}_{22}(\gamma_o, \alpha, \nu) \sum_k \delta(\gamma_o U_o - \omega) \frac{|\zeta_k^{\pm} D(\lambda_k^{\pm})|^2}{\sqrt{\kappa_e^2 - f_k^2}} d\gamma_o d\alpha d\nu \quad (112)$$

where we have assumed that the turbulence is constant over a band of radius ΔR and we are using V for vane count rather than B . The γ_o integral can be performed via the delta function with the result

$$\Pi_{\omega}^{\pm} = \frac{V \rho_o \pi^2 c^4 \omega \Delta R}{\beta s_e U_o} \iint \bar{\phi}_{22}\left(\frac{\omega}{U_o}, \alpha, \nu\right) \sum_k \frac{|\zeta_k^{\pm} D(\lambda_k^{\pm})|^2}{\sqrt{\kappa_e^2 - f_k^2}} d\alpha d\nu \quad (113)$$

The points below are best made in the context of circumferential duct modes. To simulate the duct, note that the kinematics of the excitation waves (at constant radius) would be expressed by $e^{i(k_x d x_d + \frac{n}{R} y_d)}$ rather than the form actually used in the above analysis: $e^{i(\gamma_o x + \alpha y)}$ since the input field must be periodic on the interval $0 < y_d < 2\pi R$. From the first exponential, we can see that the interblade phase angle (phase at $y_d = 2\pi R/V$) is

$$\sigma = \frac{2\pi n}{V} \quad (114)$$

for the excitation waves. Then we can deduce, say from Equations B-6 and B-9 in Appendix B that the interblade phase angle of the response waves is

$$\sigma - 2\pi k = \frac{2\pi}{V} (n - kV) \quad (115)$$

This is reminiscent of periodic rotor/stator interaction (Tyler-Sofrin) theory where wakes from the rotor with circumferential mode order nB scatter into circumferential order $m = nB - kV$ at the stator. Since Glegg's response potential depends on γ_o , α , and k only in the combination $\sigma - 2\pi k$, we can write

$$\sigma - 2\pi k = \frac{2\pi m}{V} \quad \text{where} \quad m = n - kV \quad (116)$$

Then, in simplified form, the noise equation becomes

$$\Pi_{\omega}^{\pm} = \sum_{n=-\infty}^{\infty} \int_{-\infty}^{\infty} dK_z \phi_{22} \sum_{k=-\infty}^{\infty} (PWR)_m \quad (117)$$

where we have defined $K_z = \nu R$ (the same definition as K_3). Actual computed turbulence and acoustic response spectra at a mid frequency for Figure 11 ($\omega R/a = 50$) are shown in Figure 12 for $k = 0$. This shows that the sound spectrum is obtained as the “integral” in the transverse wavenumber (n and K_z) plane of the product of the turbulence spectrum and the acoustic response spectrum. The turbulence spectrum is smooth and non-zero everywhere; the acoustic power response spectrum has a great deal of fine structure and is zero outside the cutoff ellipse.

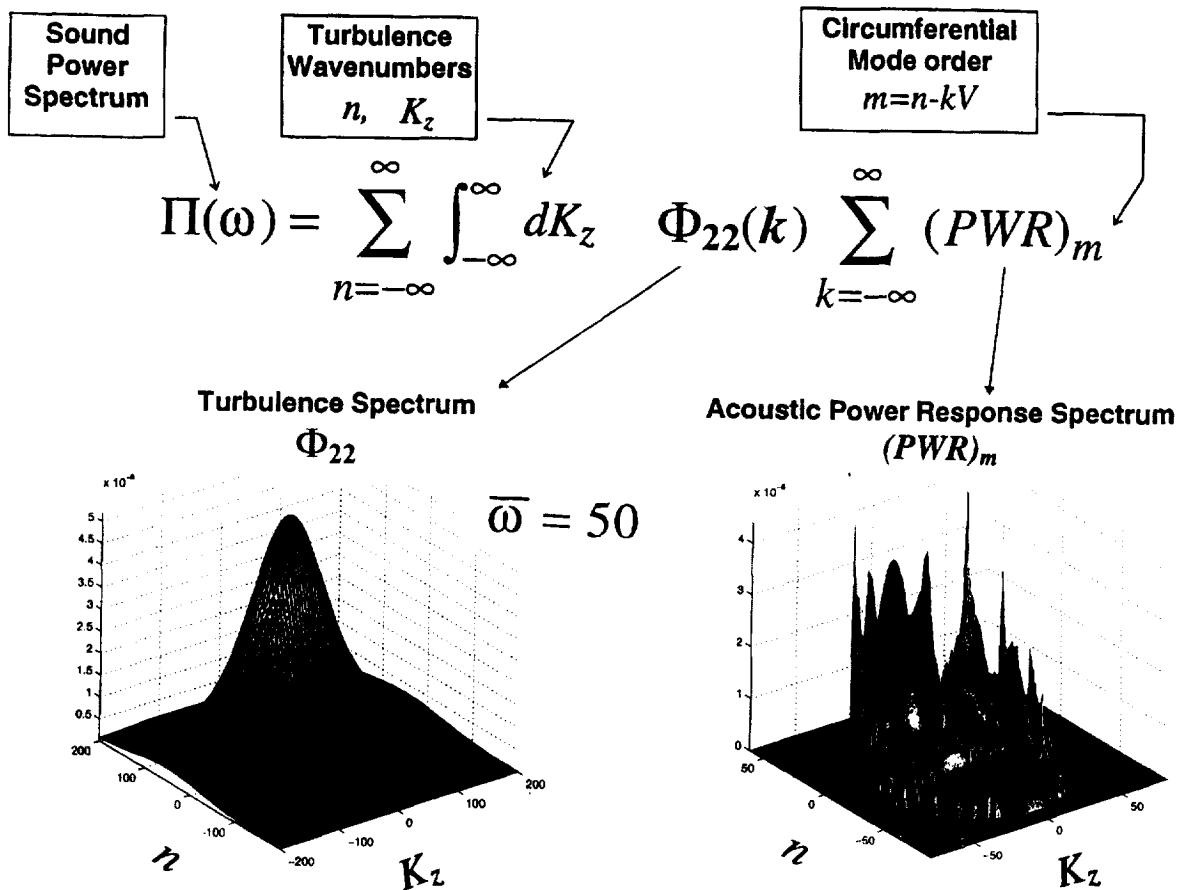


Figure 12. Examples of the turbulence spectrum and the acoustic power response spectrum (at $k=0$) for a mid-range sound frequency ($\omega R/a = 50$)

Figure 13 shows turbulence spectra at the top and acoustic response spectra at the bottom for higher and lower frequencies. It can be seen that both spectra broaden in the wavenumber plane with increasing frequency and that the acoustic response spectrum maintains its fine structure independent of frequency.

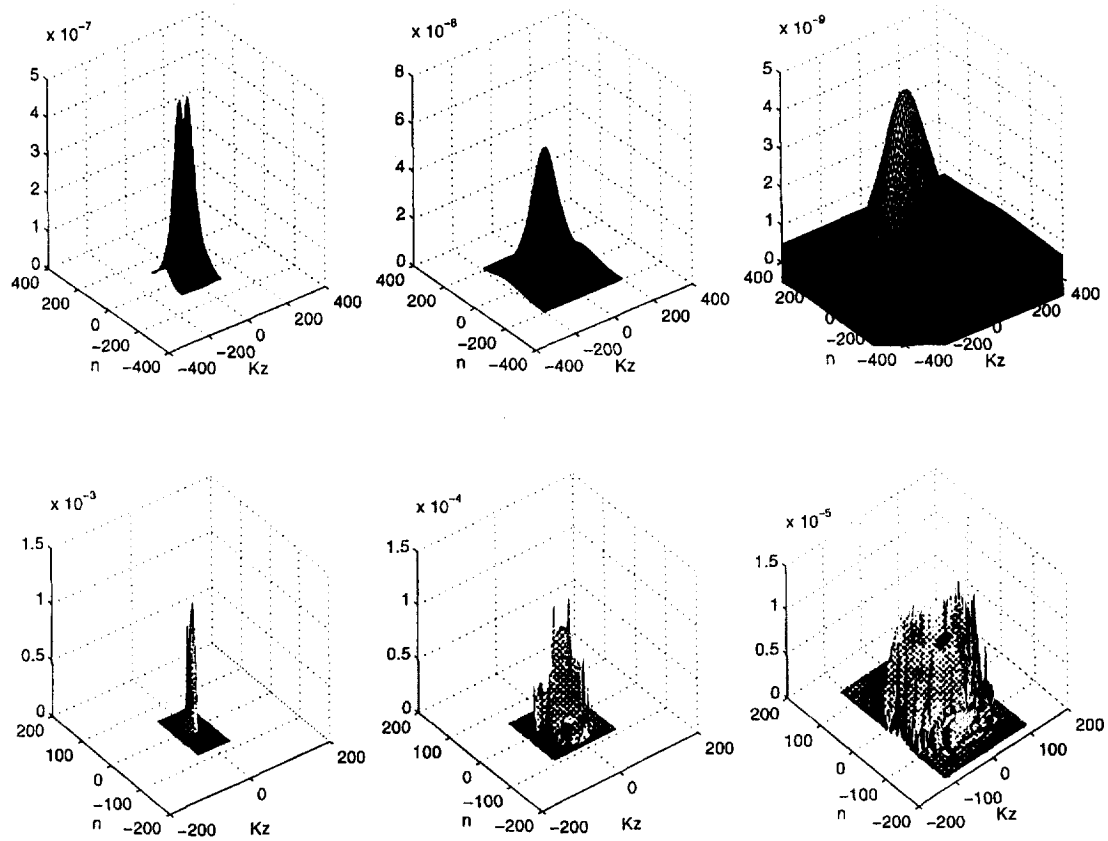


Figure 13. Turbulence spectra (top row) and acoustic spectra (bottom row) at 3 sound frequencies: $\omega R/a = 10$ (left), $\omega R/a = 50$ (center), and $\omega R/a = 100$ (right).

Figure 14 at the bottom shows the cascade response spectrum with several values of scattering index included. It can be seen that the acoustic response for each k is identical but shifted by the vane count V (30 in this example) through the mode formula $m=n-kV$. At low frequency $\bar{\omega} = 10$, the sections of the response spectrum do not overlap. Comparison with the turbulence spectrum above in the figure shows that only small portions of the wavenumber plane contribute to the sound. Specifically, response to radial wavenumbers is limited by cutoff approximately to the range ± 12 where the turbulence spectrum is near its peak. However, the response to circumferential wavenumbers is not limited by the acoustic response spectrum but by the rolloff of the turbulence spectrum.

The right hand part of Figure 14 applies to the mid-frequency point of Figure 11. In accordance with Equation 100, the "radius" of the cuton ellipse increases but the sections of the acoustic response shift only by V (independent of frequency), so that they overlap. Thus, some turbulence wavenumbers produce noise in multiple circumferential modes.

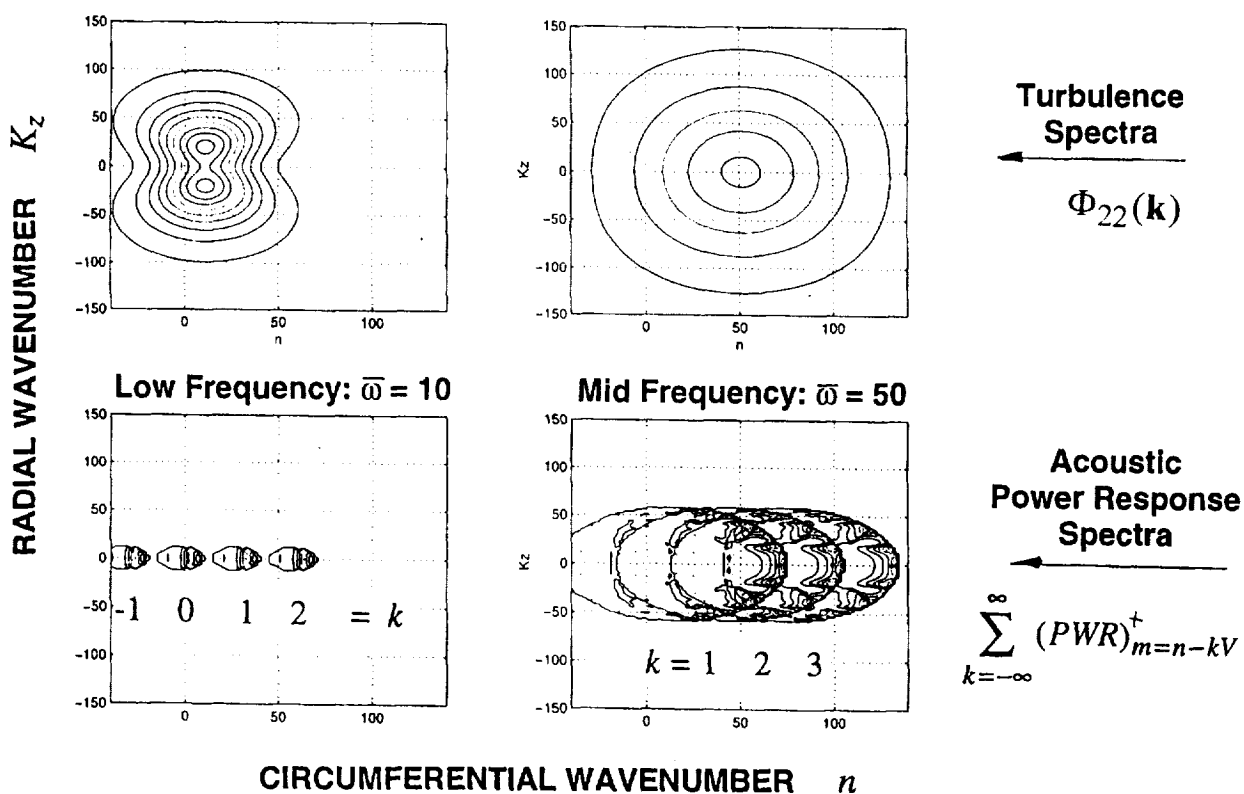


Figure 14. Contour plots of the turbulence and acoustic spectra for a several values of the scattering index k .

SECTION 8

COMPARISONS WITH TEST DATA & RELATED PARAMETRIC STUDIES

In this section we explore the capabilities of BBCascade in prediction of broadband noise of stators and rotors and establish sensitivity to design and flow parameters. Fans are represented via a single representative radius calculation rather than making any attempt to integrate over fan radius as is done in the BFaNS code. Thus, we do not expect perfect agreement but look for correct spectrum shapes and correct trends and approximate absolute levels. Three data sets are used:

ADP Fan 1 (Section 8.1)

22" low speed, adjustable pitch fan

Tested in the NASA-Glenn 9x15 tunnel

Allison Fan (Section 8.2)

22" fan with combinations of stator lean and sweep

Tested in the NASA-Glenn 9x15 tunnel

Boeing Fan (Section 8.3)

18" fan with variable geometry for noise source separation

Tested in the Boeing LSAF (Low Speed Aeroacoustic Facility)

In each of the subsections below (Sections 8.1, 8.2, 8.3), the format is to check predictions for a few data points to verify correct behavior of the theory and to establish base cases for further studies. Then we present parametric variations on the base cases to provide an understanding of the noise generation process.

8.1 Variations on ADP Fan 1 – Turbulence Scale, Mach Number, Stagger and Chord

Since noise predicted by Equation 94 depends on only a small number of input variables, it was straightforward to compute the variation of noise with turbulence properties (intensity and scale), mean flow (Mach number), and geometry (stagger, vane count, and gap). The base case for the variations was essentially the same as that for Figure 11 except that the vane count was changed to 30. Stagger was 30°, gap/chord was 0.8, Mach number was 0.5, turbulence level (upwash component) was 2% of the mean flow velocity and the integral scale was 3.5% of the fan radius.

First, recall how the curve fit in Figure 11 was obtained. Mach number, stagger, chord, solidity, radius, and area were fixed leaving only turbulence intensity and scale as free parameters. From Equation 94 it is evident that spectra simply move up and down with turbulence intensity (3 dB per doubling of turbulence energy). Turbulence scale, however, is more interesting, as shown in Figure 15. (In this and succeeding plots, the solid curve is the base, or reference case.) At high frequencies, the level varies as $1/\Lambda$, which could be deduced from the form of the turbulence spectrum in Equation 69. At high frequency, the 1 in the denominator becomes insignificant and all but one of the Λ 's cancel. At low frequencies, the effect reverses and scale has a powerful effect. Thus, to achieve the match in Figure 11, intensity was varied to move the theory curves up and down and scale was varied to change the balance between low and high frequencies.

Figure 16 shows the variation of noise with Mach number at constant *percent* turbulence, i.e. for constant $\overline{w^2}/U_{stat}^2$ in Equation 71. On the upstream side, the curves generally move up in level and frequency with increasing Mach number. Behavior on the downstream side is similar except that the spectrum tends to flatten at the higher Mach numbers. Peak levels of these curves were cross plotted against Mach number in Figure 17 to find if a simple power law (M^n) would describe the behavior. All curves were referenced to the $M=0.5$ values. On the downstream side, M^5 fits reasonably well. On the upstream side, no exponent works perfectly but 4.5 fits the points between $M = 0.5$ and 0.7.

Figure 18 shows variations with cascade stagger angle. The effect is weak on the downstream side and almost zero on the upstream side.

Finally, we look at variations with vane count and gap/chord ratio. Vane count is a major consideration for harmonic noise; large numbers lead to cutoff (exponential decay in the axial direction) of the lower harmonics. In designing stators, there is usually a preferred solidity (inverse gap/chord ratio) for performance purposes but some latitude for vane count at constant solidity. Figure 19 shows broadband noise variation with vane count at constant solidity. At the mid and high frequencies the noise is roughly proportional to vane number ($PWL \approx 10 \log V$). At lower frequencies there is little effect. Thus, we are driven in different directions for tone and broadband noise. Figure 20 shows that variations in gap/chord ratio have almost no effect for constant vane count. This was a surprise since acoustic response for individual input waves is very sensitive to gap/chord; however, when the turbulence is integrated over a broad range of wavenumbers, the sensitivity to gap/chord is much weaker.

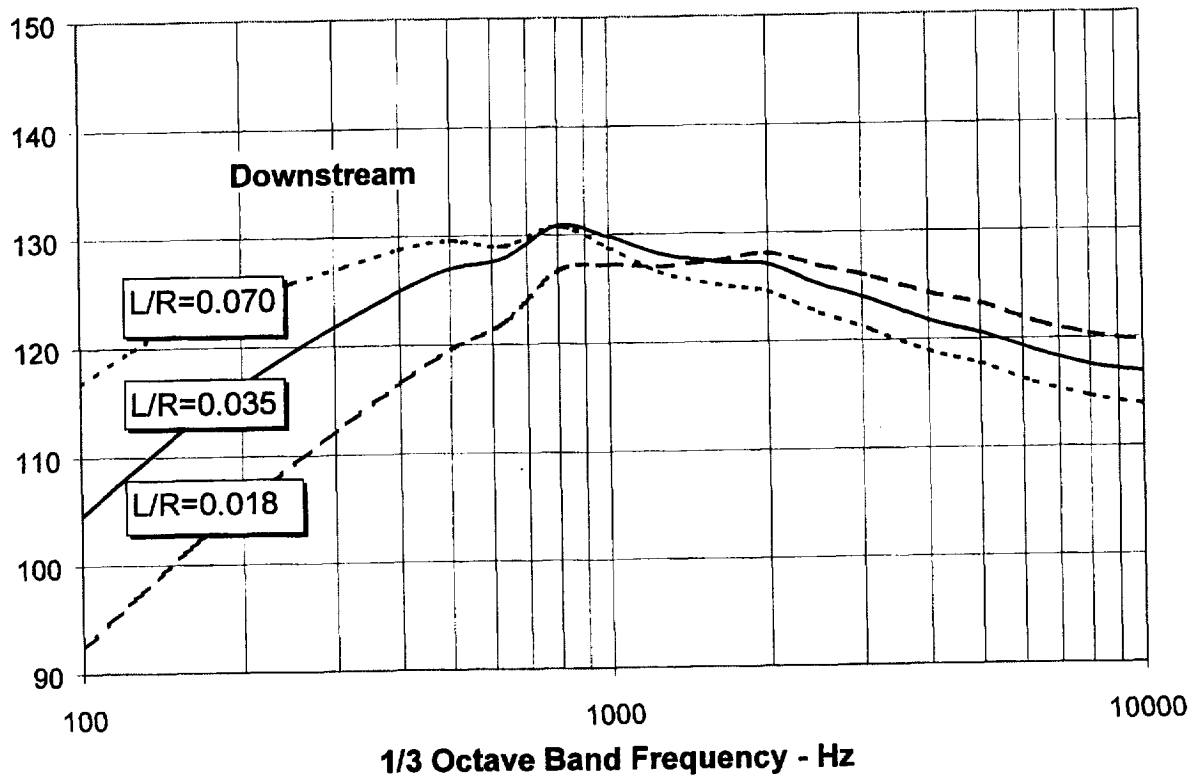
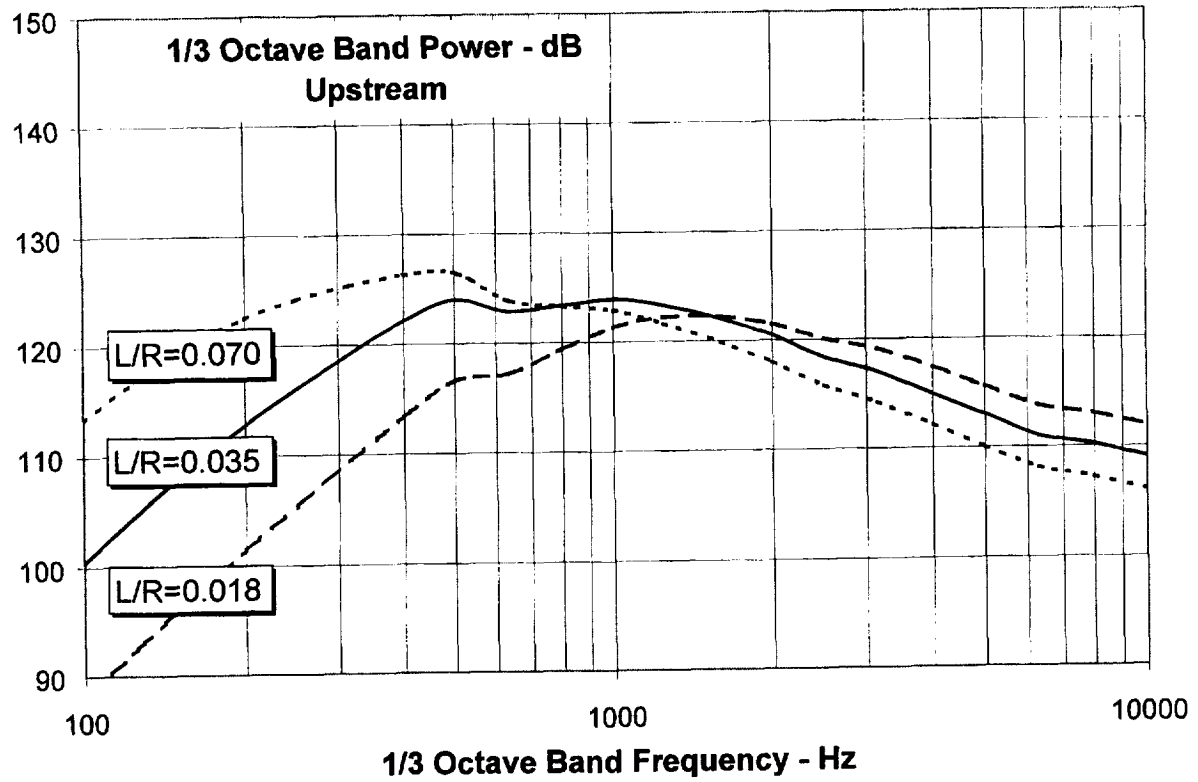


Figure 15. Variation of stator noise with turbulence scale. L/R is turbulence integral scale/fan radius.

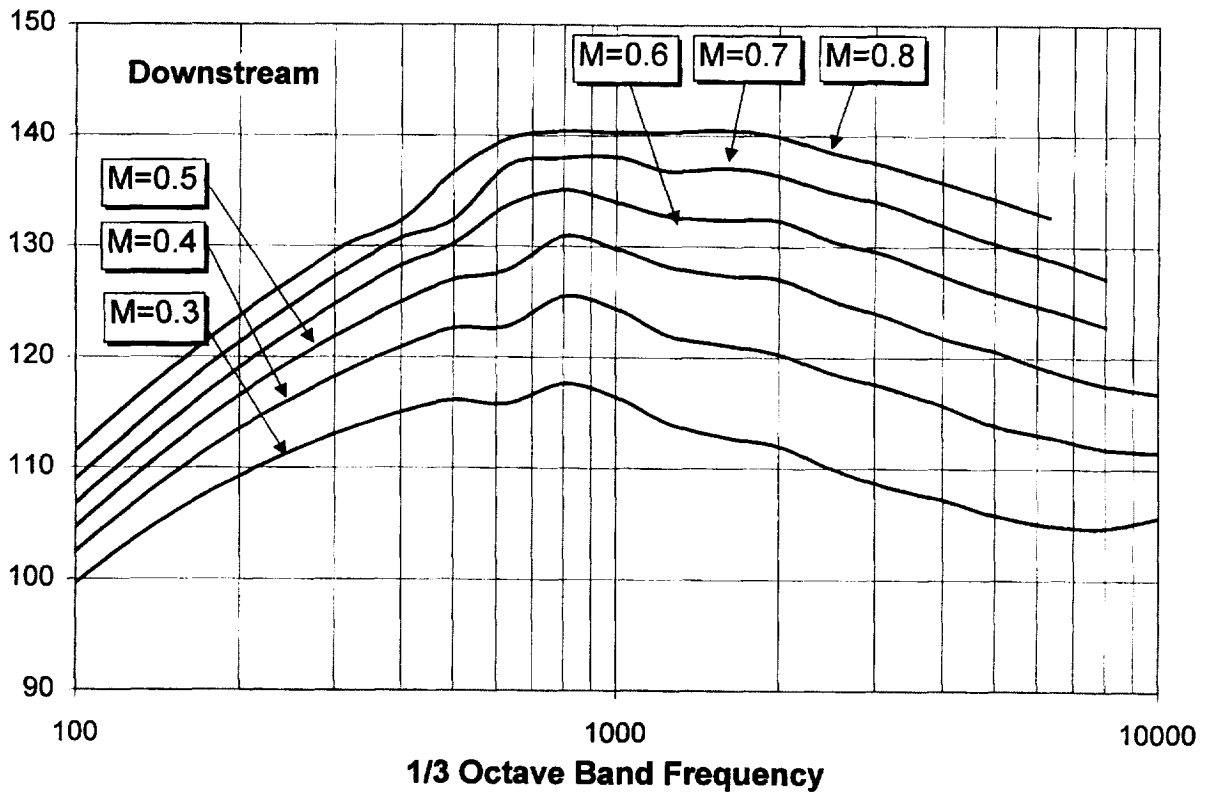
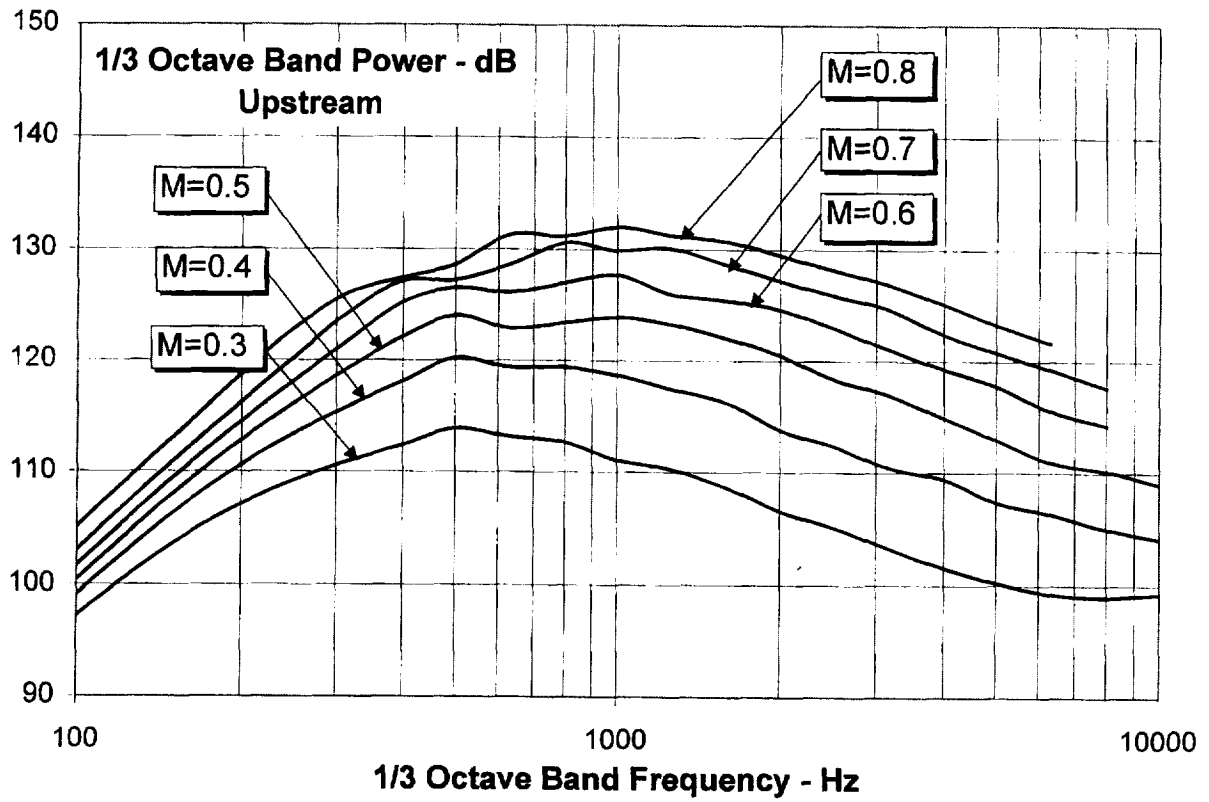


Figure 16. Variation of stator noise with inflow Mach number at constant percent turbulence.

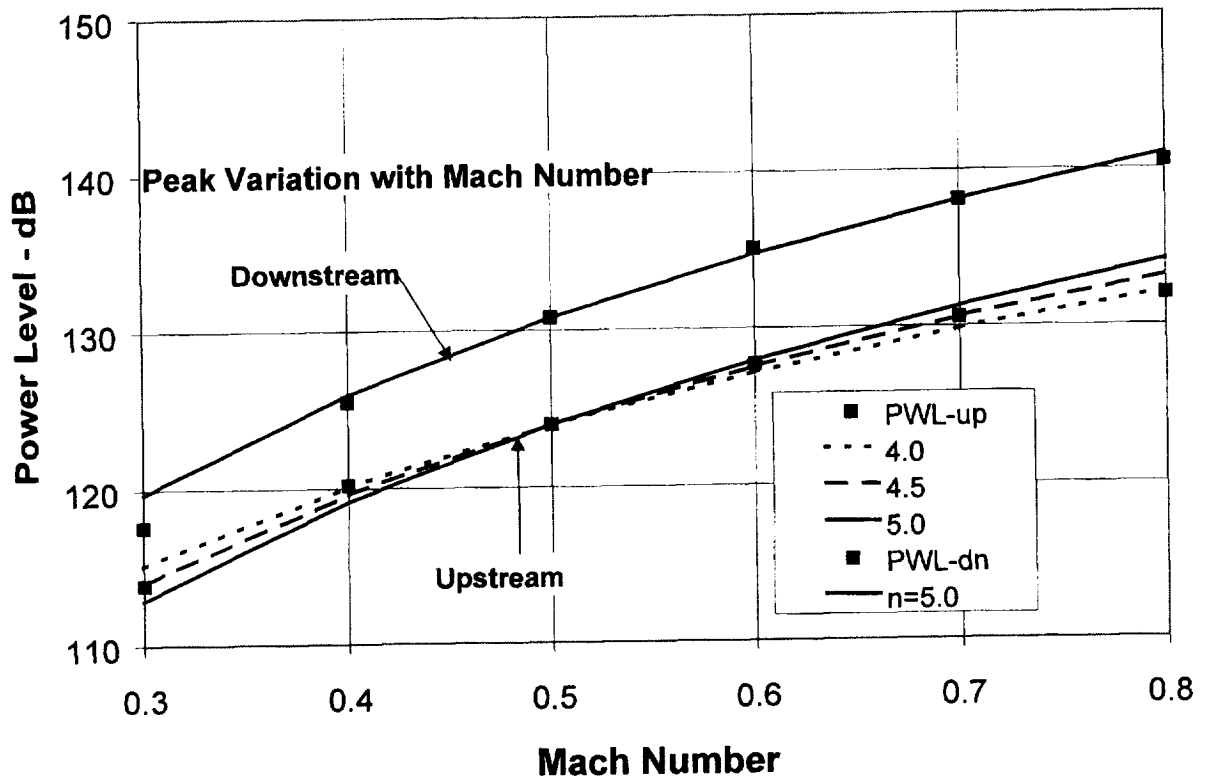


Figure 17. Variation of spectrum peak levels with Mach number. Curve fits represent $PWL \sim M^n$

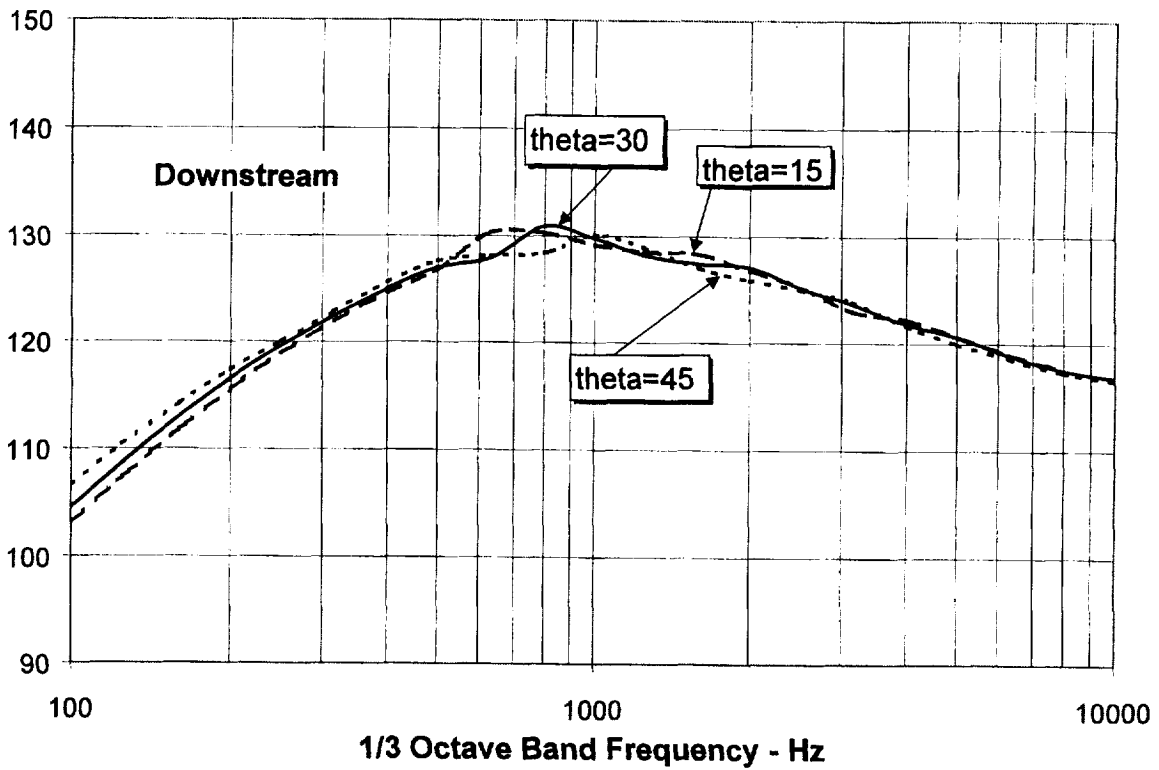
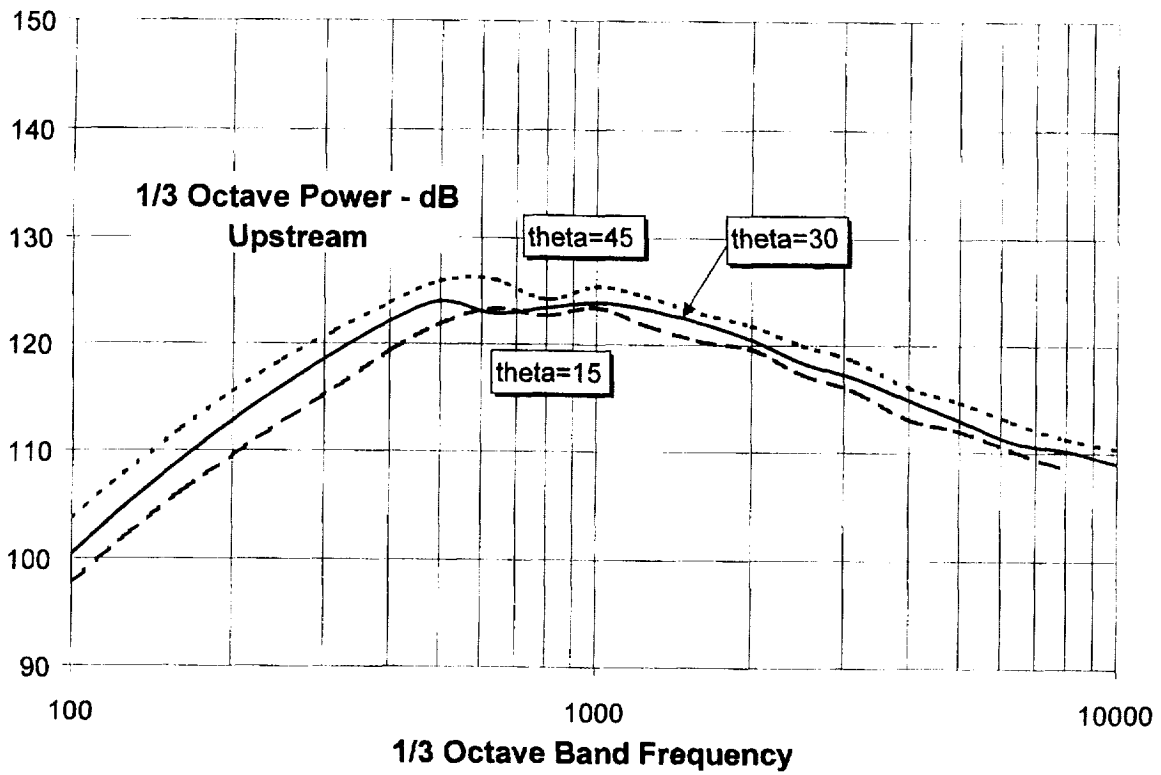


Figure 18. Variation of stator noise with cascade stagger angle.

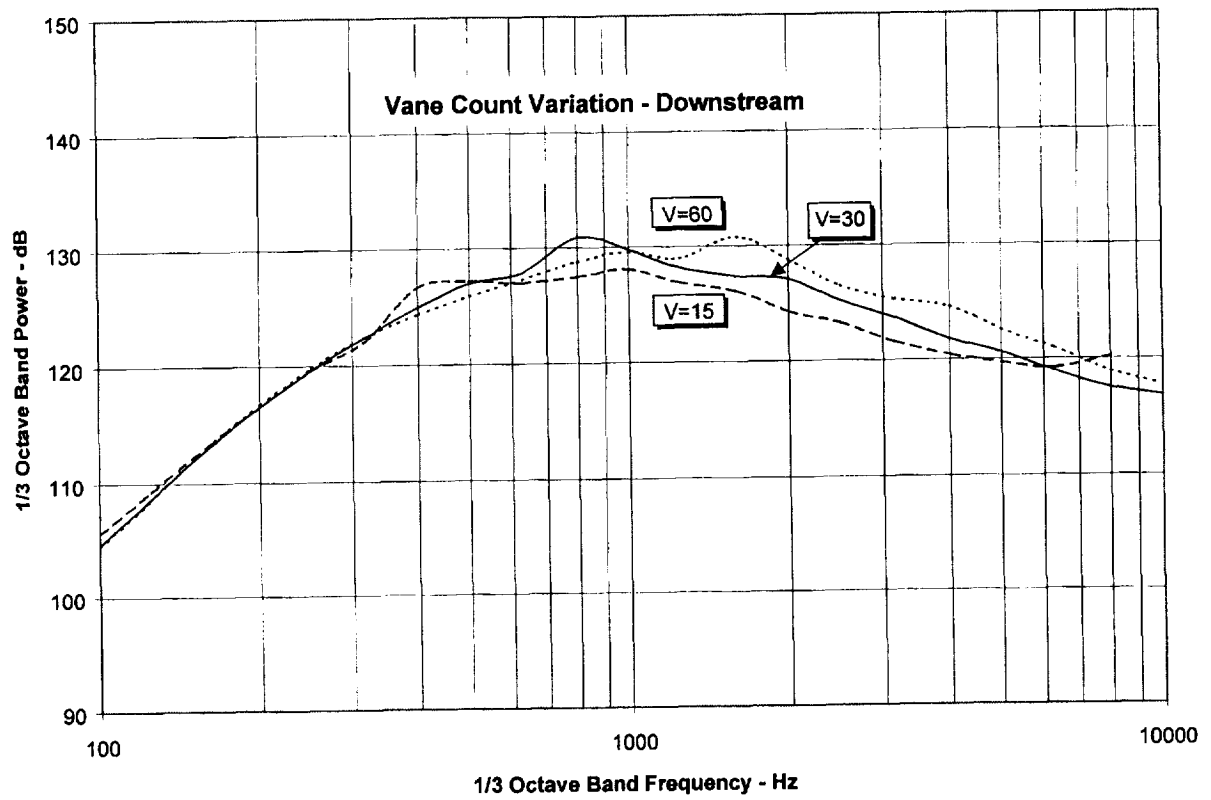
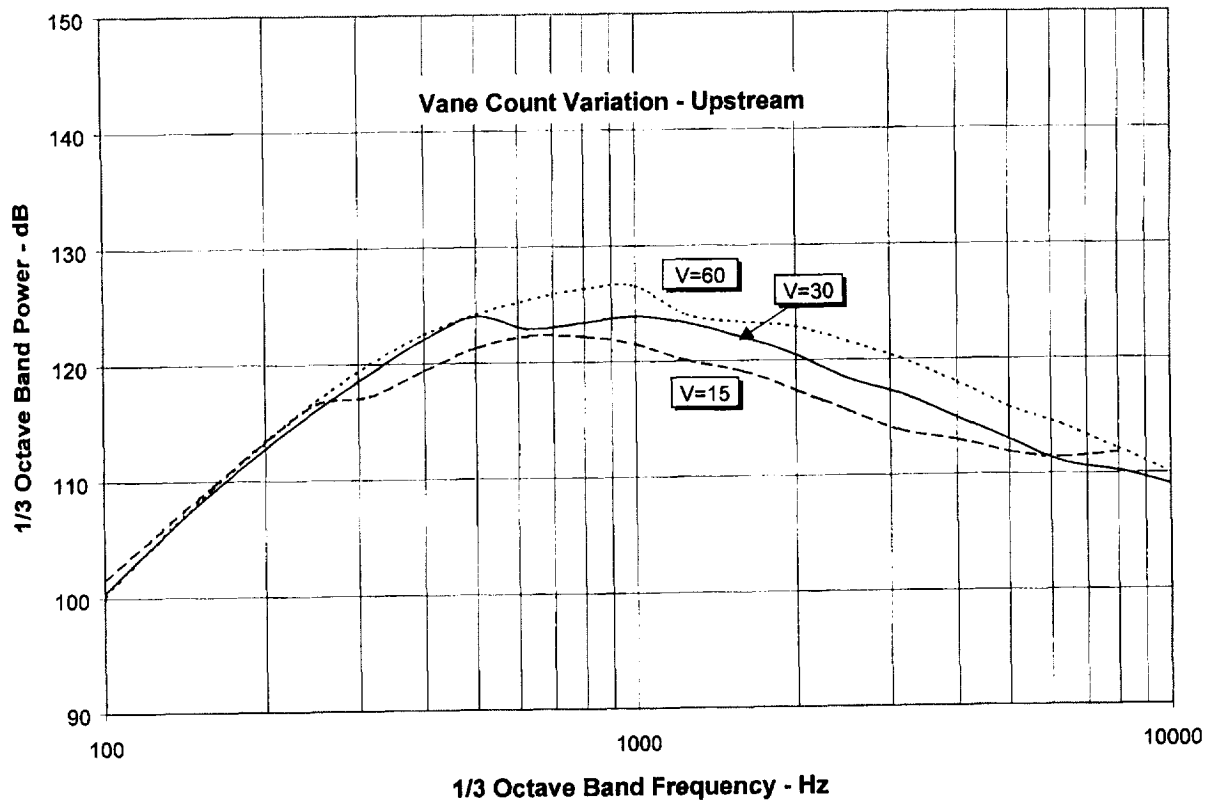


Figure 19. Variation of stator noise with vane count at constant gap/chord ratio.

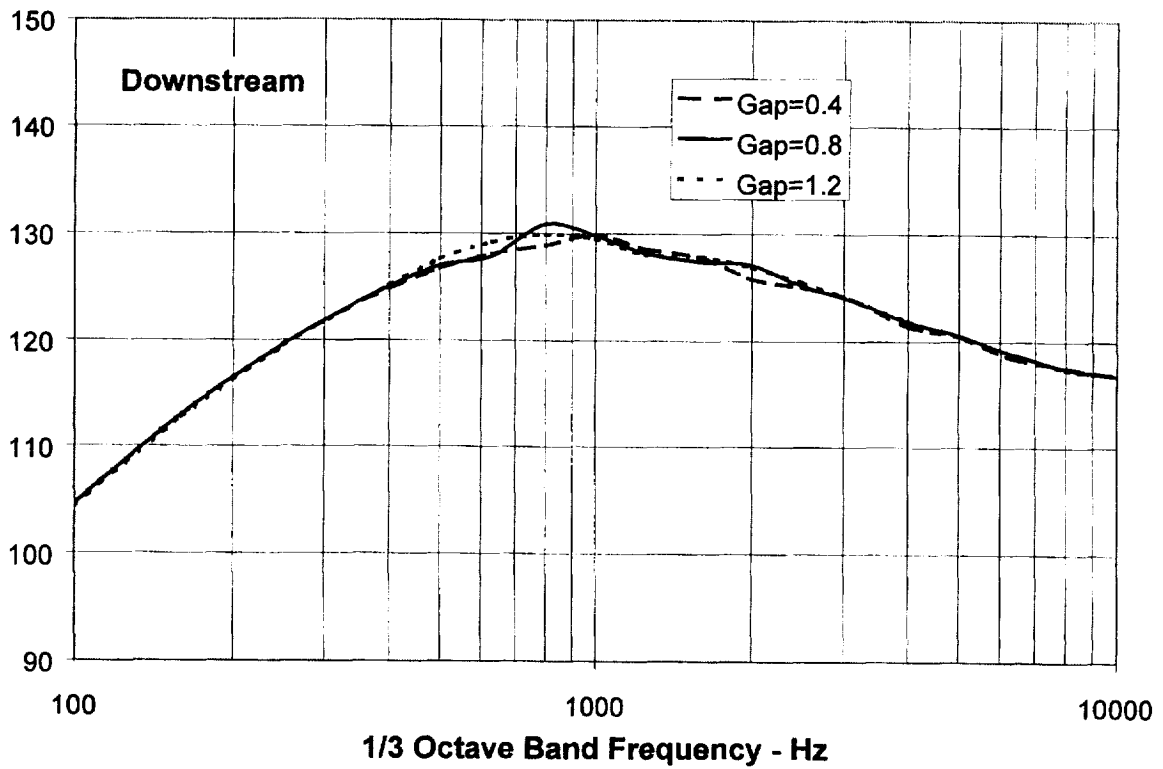
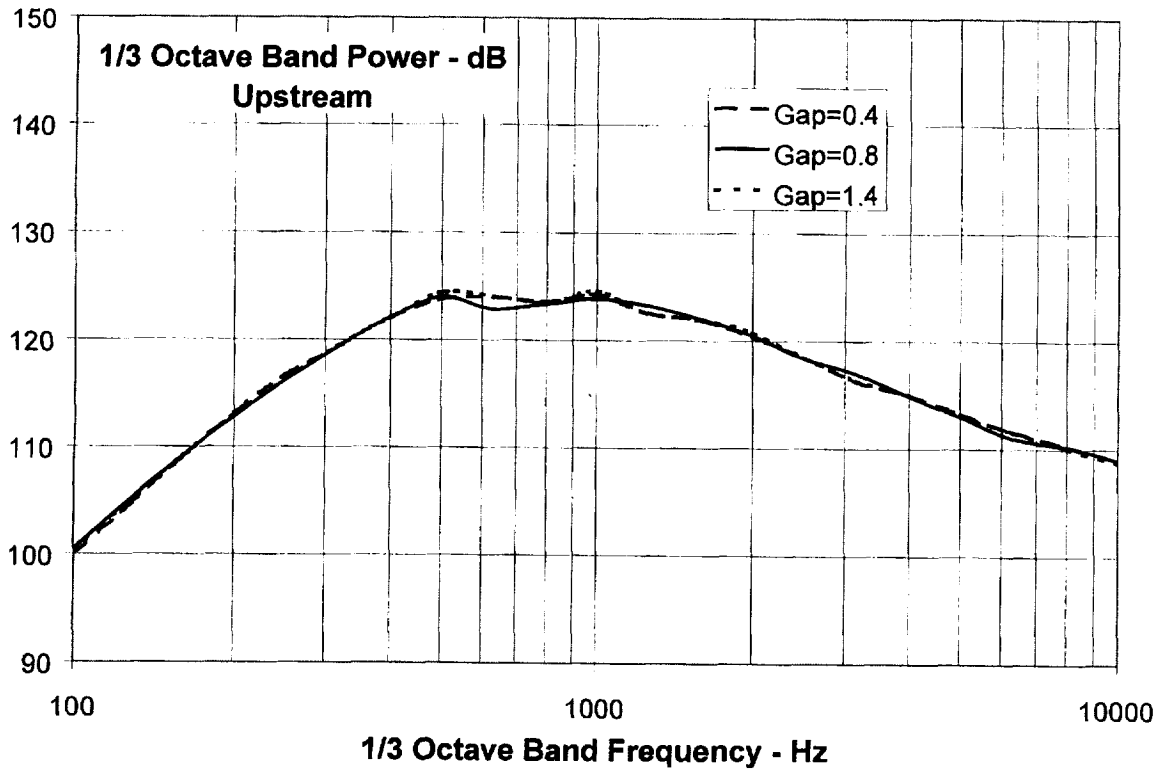


Figure 20. Variation of stator noise with gap/chord ratio. (Chord was varied at constant vane count.)

8.2 Allison Fan and the Effects of Lean and Sweep on Stator Noise

For another check of the theory, we compared calculations with the lean and sweep data from the Allison fan^{ref. 12} shown in Figure 21. The stator at the top in the figure has its tips swept axially; i.e. per the nomenclature of this report, it is swept 30° in the “duct system” ($\hat{\psi}_s = 30^\circ$). At the bottom Figure 21 shows another stator with both lean and sweep in the duct system ($\hat{\psi}_s = 30^\circ$ and $\hat{\psi}_l = 30^\circ$). Allison and NASA tested both of these stators plus radial stators at 2 axial positions. One axial position was at the root position of the swept stator and the other was at the tip position of the swept stator.

Figure 22 shows sound pressure spectra in the aft quadrant for the 4 stator configurations. Although the figure is difficult to decipher, it can be seen that sweep eliminates the tones. Furthermore, sweep provides broadband noise reduction over a wide range of frequency and lean added to sweep provides a further improvement. Reference 12 gives the vane count and the sweep and lean angles; however educated guesses had to be made for the other parameters needed for spectrum calculations. We used the same non-dimensional parameters as for Figure 11 except that the Mach number was reduced to 0.3 (based on Allison’s 50% design tip speed). Figure 22 at the bottom shows that the theory follows the Allison data very well. The spectrum shapes are good and the reductions for sweep and sweep+lean match the data as well as can be determined from the curves.

The remainder of this section explores theoretical trends with lean and sweep and explains the Allison results.

Lean and Sweep Parametric Studies

In this section we examine trends in noise reduction with various combinations of lean and sweep. This is done in the context of the 2 conventions for defining lean and sweep: the “cascade system” of Figure 4 and the “duct system” of Figure 5.

The following spectra were all computed using the same geometry, mean flow, and turbulence properties used for Figure 11. Only the downstream sound power spectra are shown since they are higher and look similar to the upstream spectra. Figure 23 shows the effect of lean and sweep for angles defined in the duct system. Lean has almost no effect except to move the dip in the spectrum. (In reference 3 it is shown that the frequency at this dip corresponds to a half wavelength fitting between 2 vanes. Leaning the vanes changes the normal gap – Glegg’s *h*.) Sweep is more effective; the slight increase at low frequency would not be seen in fan test data because of other sources. Figure 24 shows lean and sweep effects for angles defined in the cascade system. Here, again, lean is very weak but the sweep effect is stronger than in the duct system.

The previous curves were for lean alone or sweep alone. Since it is important to know how the 2 effects work together, combinations of lean and sweep were run and the peak values from the downstream spectra were plotted in Figure 25. The top of Figure 25 applies to the cascade system (sweep in the plane of the vane). It shows noise reduction versus sweep for lean angles of 0°, 15°, 30°, and 45°. The curves show that sweep is the dominant effect. In this system sweep reduces the component of Mach number normal to the leading edge; lean does not. The solid curve shown in the figure

$$\Delta dB = -30 \log_{10}(\cos \psi_s) \quad (118)$$

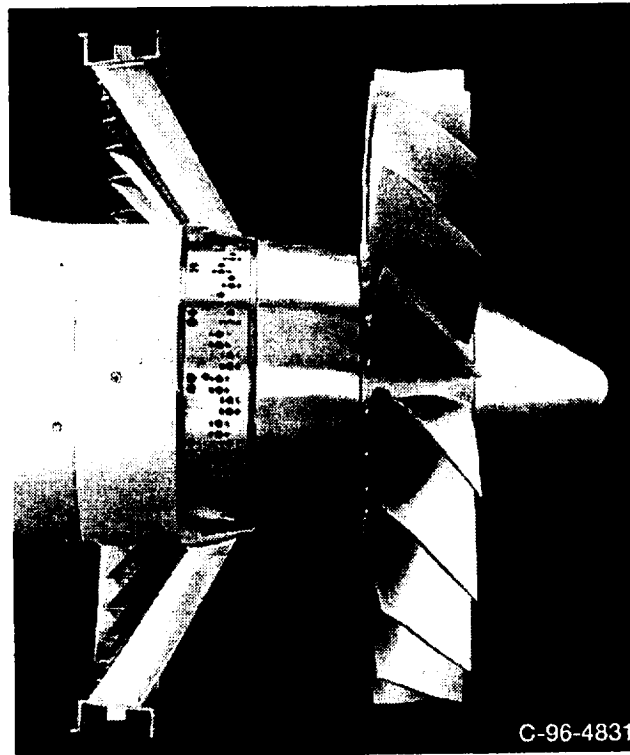
provides a reasonable fit to the theory. (Recall that the lengthening of the leading edge is included in the theory. Without this, the factor would be 40 rather than 30.) Negative lean

angles are not shown. However, the curves apply to negative lean if the signs of the sweep angles are reversed.

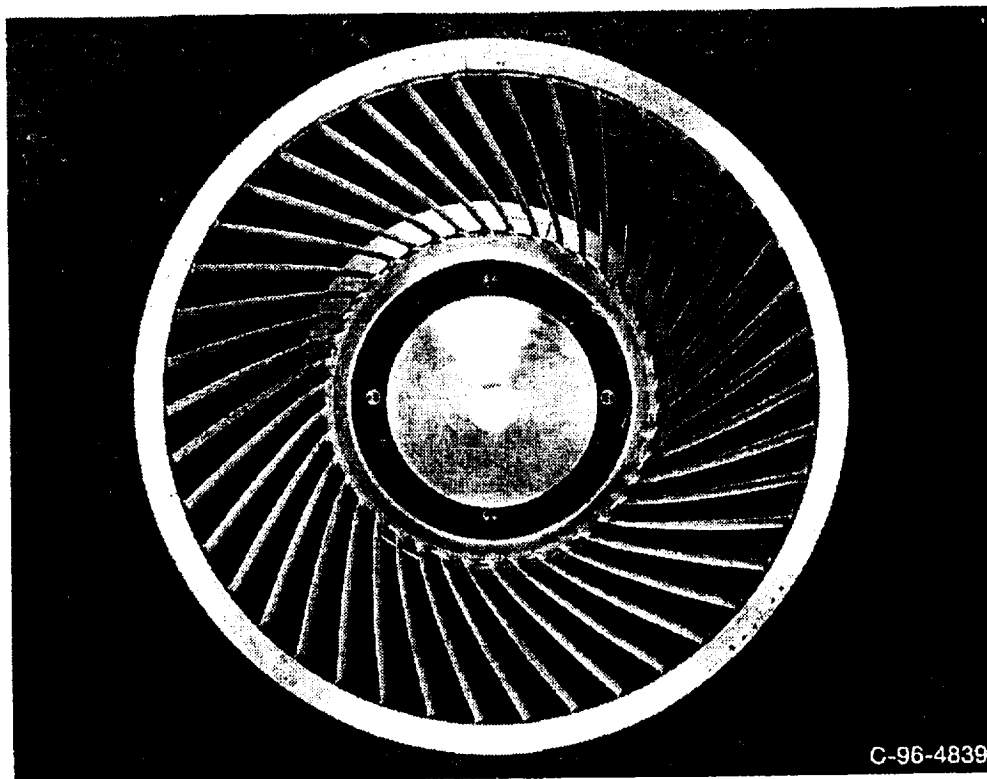
The bottom of Figure 25 applies to the duct system, i.e. lean and sweep angles defined via the front and side views of the fan. Here the picture is complicated due to a strong interaction between lean and sweep. However, $-30 \log_{10}(\cos \psi_s)$ is still valid (no hat on ψ_s). We need only apply Equations 15, which relate angles in the duct and cascade systems, to convert the solid curve from the top of Figure 25 to the multiple curves at the bottom. The curves track the theoretical peaks reasonably well and can be used for design guidance.

Finally, refer again to the Allison data in Figure 22. Sweep and lean were both 30° . Calculated results shown in Figure 25 predict that 30° sweep by itself produces about 1.1 dB benefit and that 30° lean added to the sweep brings the total reduction to 3.9dB. This is in approximate agreement with the Allison data. If they had leaned in the opposite direction, the net effect would have been near 0 dB. The curve-fit plots in Figure 25 (the solid curves) indicate slightly different results: 1.5 dB for sweep and a total of 3.0 dB. Note that it was not luck that caused Allison to lean in the more favorable direction; this is the direction preferred for tone noise reduction.

The curve fit without the BBCascade calculations is shown in Figure 26 with sketches defining the lean and sweep conventions. Note that this is simply a plot of $-30 \log_{10}(\cos \psi_s)$ in the duct (or "hat") system for 30° stagger. Details will be different for different stagger.



Photograph of the partially-assembled fan stage showing the swept-only stator.



Downstream view of the swept + leaned stator.

Figure 21. Allison fan disassembled to show swept stator (top) and swept and leaned stator (bottom).
Reproduced from Woodward, *et al*, ref. 12.

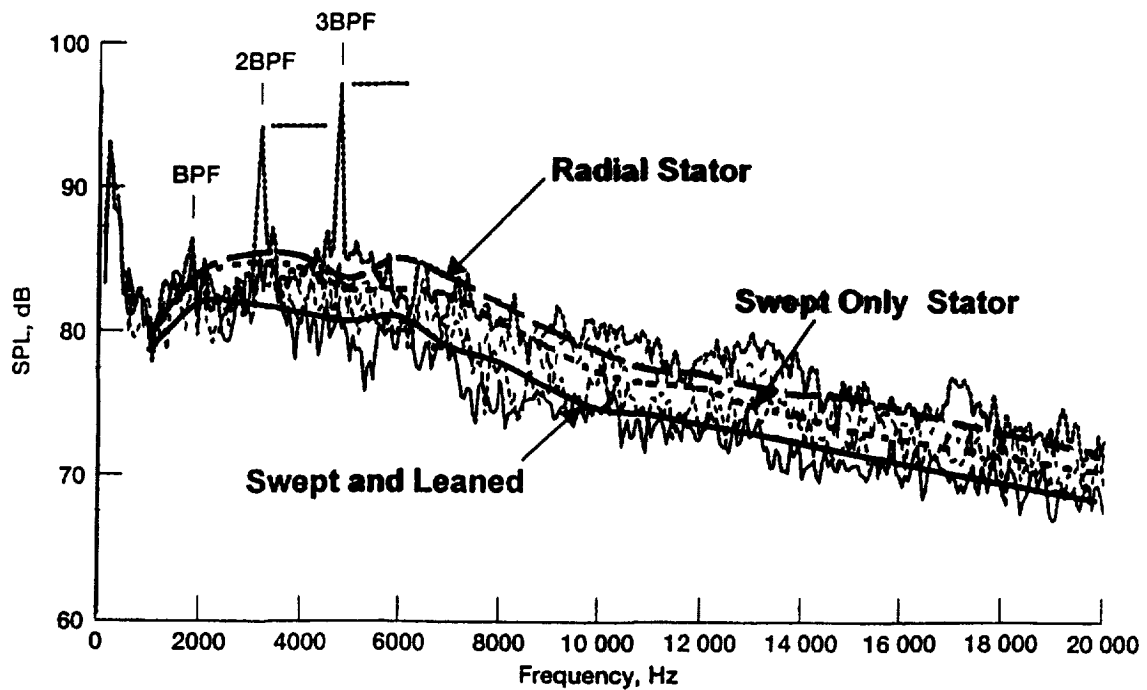
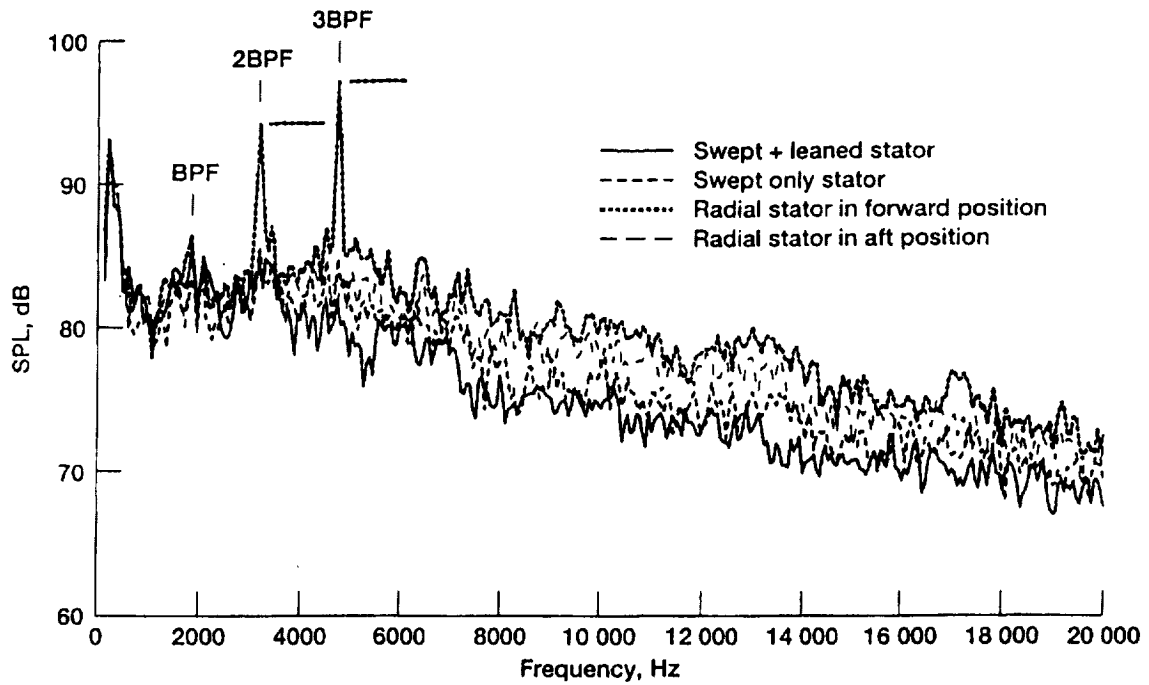


Figure 22. Top –variation in sound pressure spectra with lean, sweep, and axial position of stator. Allison fan at 50% speed/126° from inlet axis. Bottom – predictions for aft sound power spectra.

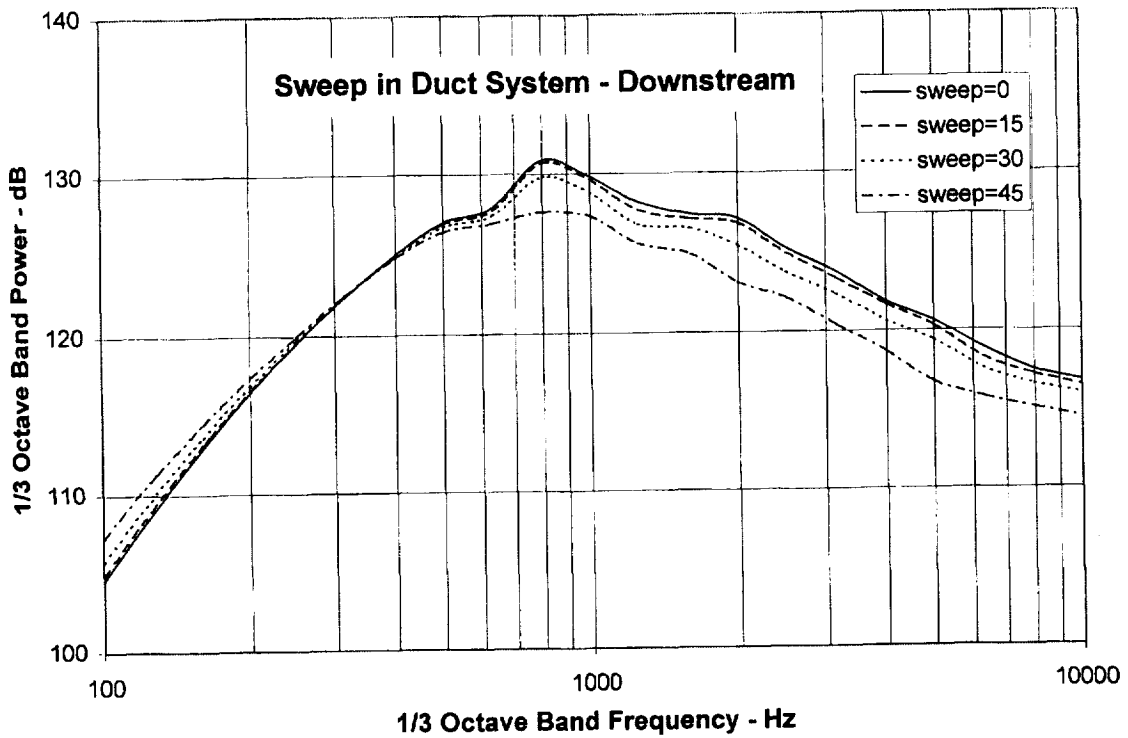
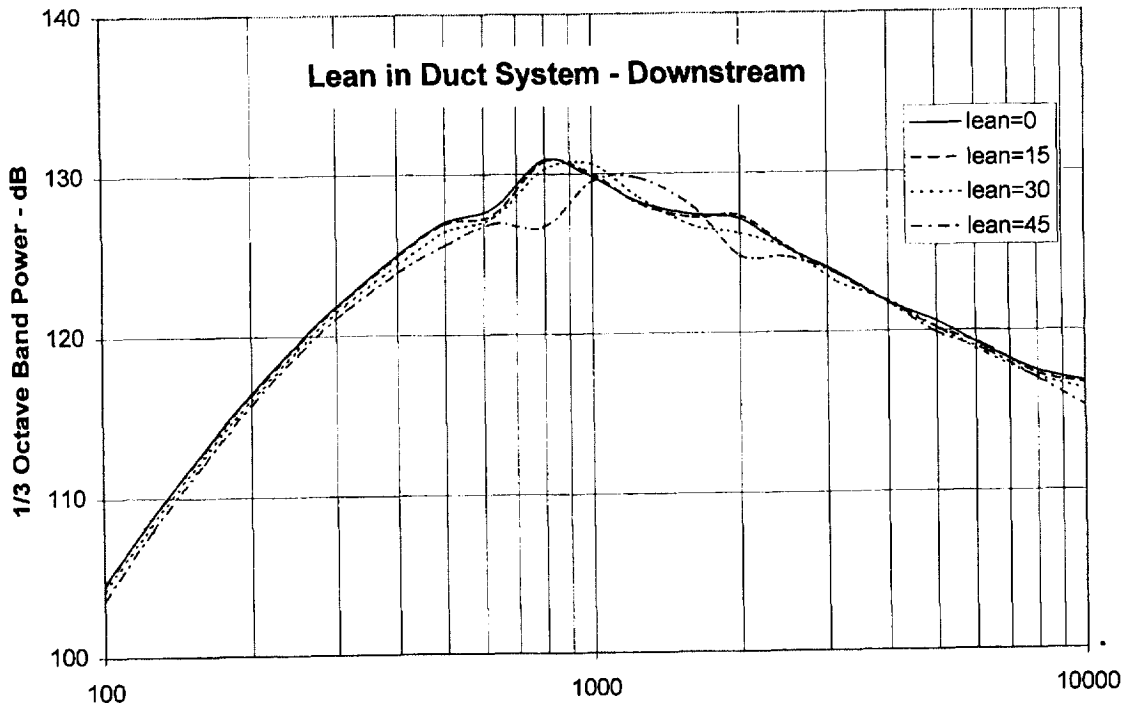


Figure 23. Variation of stator noise with lean and sweep angles as defined in duct coordinates

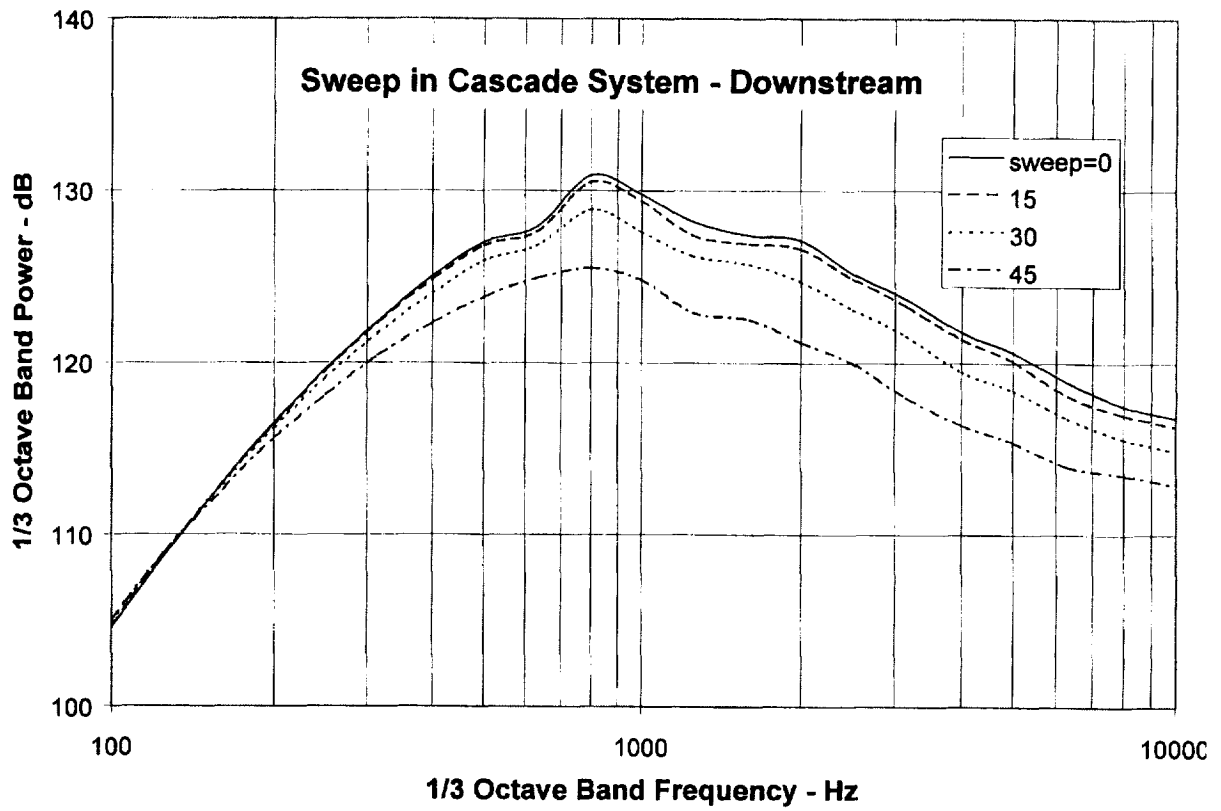
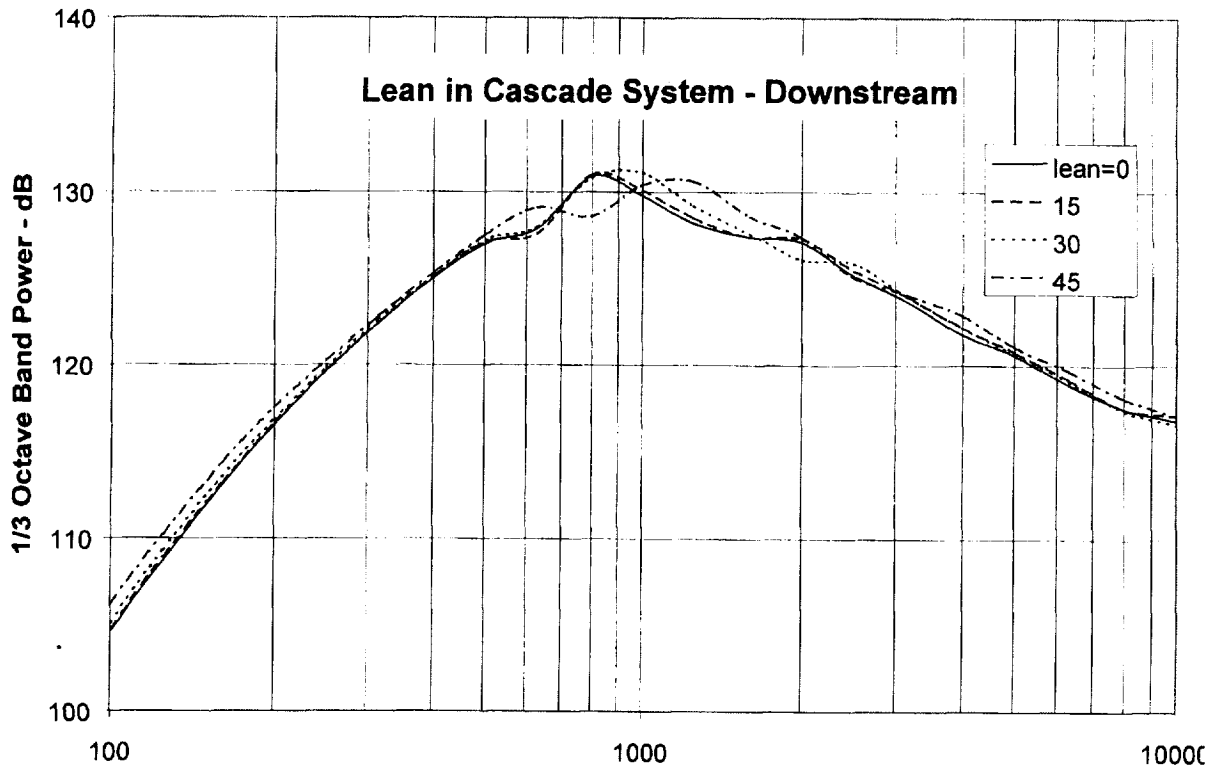


Figure 24. Variation of stator noise with lean and sweep angles as defined in cascade coordinates

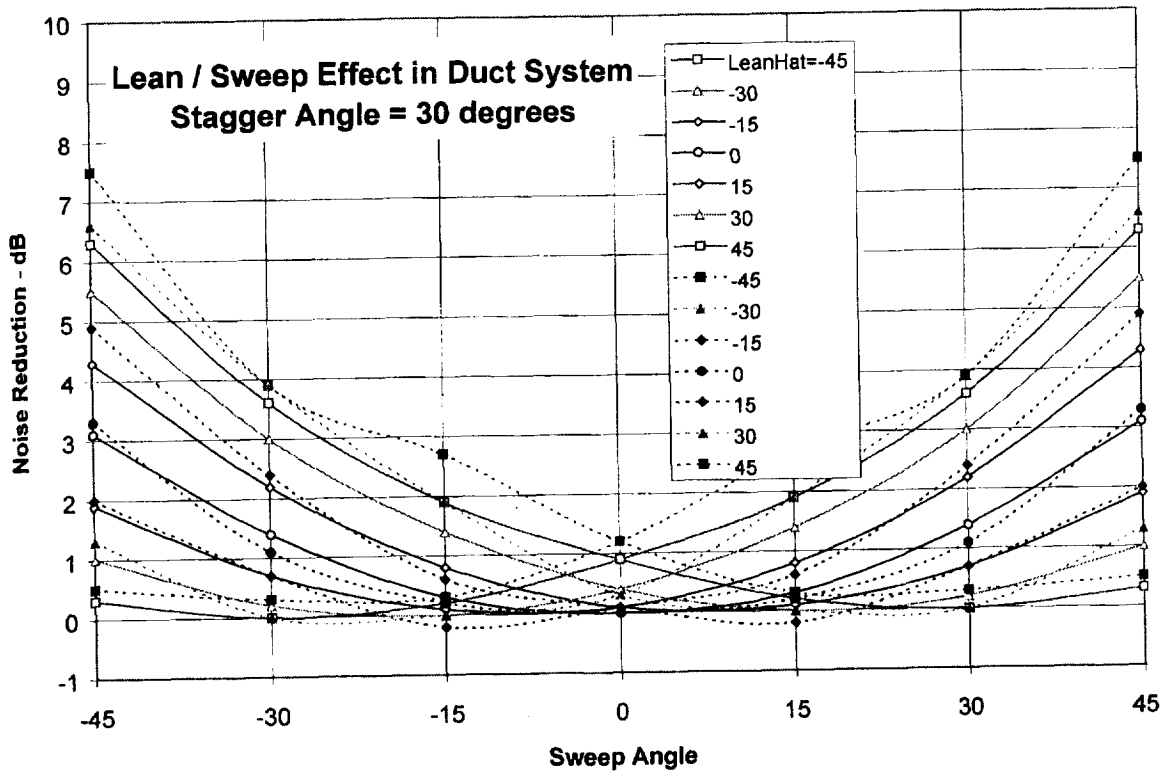
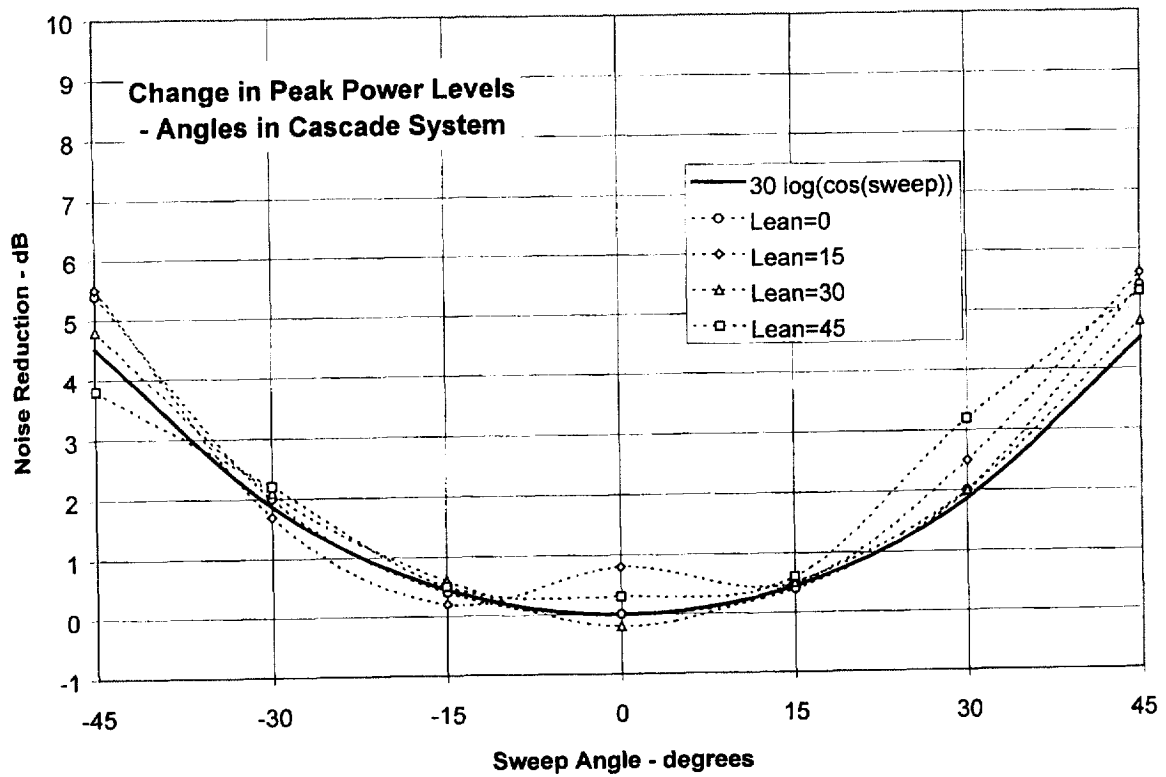


Figure 25. Variation of stator noise with combinations of lean and sweep. Top: angles defined in cascade system. Bottom: angles defined in duct system. Solid curves are $\Delta dB = -30 \log_{10}(\cos \psi_s)$.

Lean / Sweep Effect on Broadband Noise

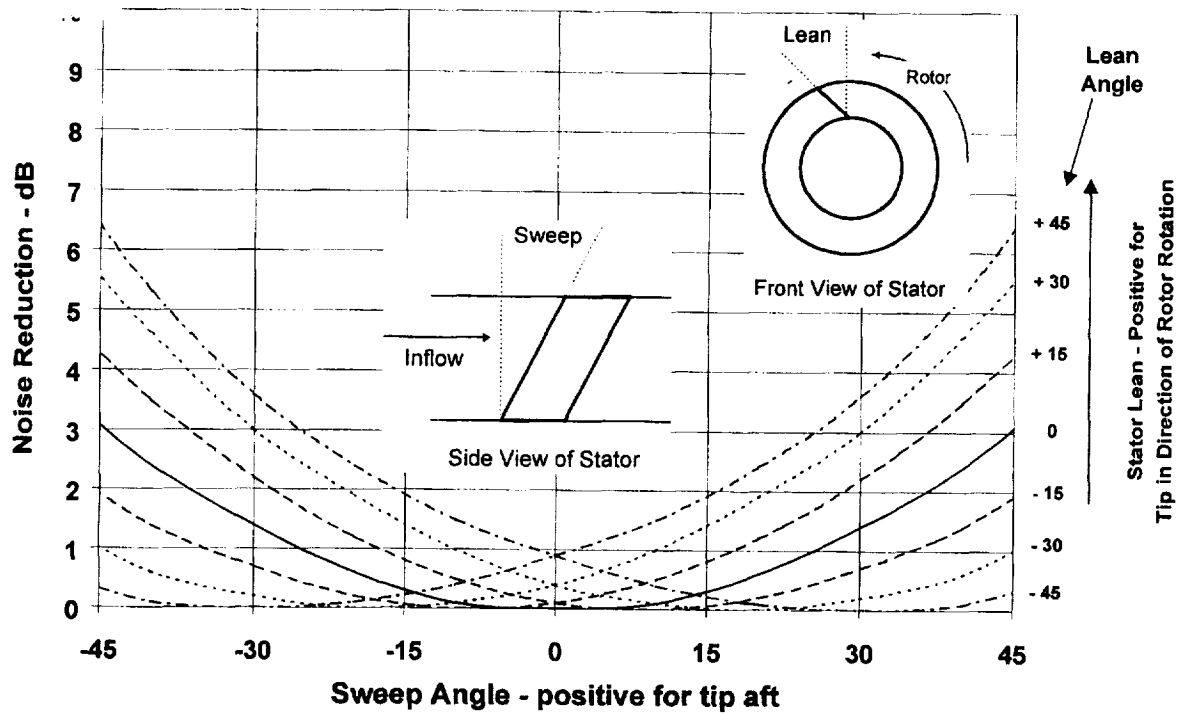


Figure 26. Plot of noise peak noise reduction from curve fit: $\Delta\text{dB} = -30 \log_{10}(\cos \psi_s)$. (Same as in preceding figure.)

8.3 Boeing Fan Analysis and Variations

This section checks BBCascade against Boeing's data for inlet turbulence/rotor noise, rotor wake/stator interaction noise, and mode order/frequency plots.

Inlet Turbulence / Rotor Noise

The Boeing 18" noise research fan was designed for source separation by experiment. It can be run without stators and with the duct boundary layer upstream of the rotor removed. By comparing rotor noise with and without the boundary layer, the contribution of boundary layer turbulence/rotor noise can be determined. Then by comparing noise without the boundary layer with and without stator, the contribution of the stator can be determined. The results of this source separation are shown in Figure 27 (reproduced from ref. 1) for inlet sound power spectra at 70% rpm and aft sound power at 55% rpm. (100% rpm was equivalent to 1300 ft/sec rotational tip speed.) The boundary layer source is not dominant but it can be seen to affect the total level in both cases over a broad range of frequency. The bold curves in Figure 28 are a test of BBCascade's rotor noise capability. These were computed using the geometry and mean flow conditions at the rotor tip. For turbulence intensities, we used the values at a distance 50% of the boundary layer thickness (δ) from the wall were used (4% / 3% for the axial / transverse components). For turbulence axial and transverse scales, we simply adjusted them to produce a good fit to the noise spectrum as shown at the bottom in Figure 28. The values that worked best were axial / transverse scale = 7% / 2% of fan radius. This is not very satisfactory since the axial scale of the streamwise component that would be deduced from ref. 1 at 50% of δ is roughly 3.5% of fan radius. We do not have an explanation for this discrepancy. Since the transverse scale was not measured, we simply comment that 2% of fan radius seems reasonable.

For the aft noise, at the bottom of Figure 28, the fit is very satisfactory. The spectrum peaks are centered at multiples of blade passing frequency. Agreement for the inlet noise is not as good; however, the Boeing report points out that there is a rotating instability that influences the spectrum. Of course, this is not accounted for in the theory.

The theoretical curve from the top of Figure 28 was used as a base case to study effects of changing turbulence length scales. Axial scale was 7% of fan tip radius and transverse scale was 2% of tip radius. Figure 29 shows variation with transverse scale in 2:1 steps. Note that this parameter is a very strong driver and must be known with some accuracy for acceptable noise estimates. Figure 30 shows variations with axial turbulence scale again in 2:1 steps. Axial scale does not change overall level strongly but instead controls the localization of energy around the blade passing frequency peaks. It can be seen that the 3.5% axial scale that would be deduced from the Boeing hot wire data produces a spectrum with peak-to-valley ratios that are too small.

Usually, we think of fan noise spectra containing pure harmonics (peaks with zero bandwidth at multiples of blade passing frequency) and a smooth broadband component. However, the results just shown are in between harmonic and broadband. The peaks are centered at the BPF harmonics but have finite bandwidth. This is caused by the rotor interfering with turbulent eddies that are long enough to be chopped by more than one rotor blade. A pure tone would be produced by an infinite number of chops but narrow band peaks are produced by finite numbers of chops. The first good model for this effect was due to Mani (ref. 13) based on isotropic turbulence. The present author brought in the essential effect of anisotropy in 1974 (ref. 14) based on a cruder model of turbulence interaction. It is interesting to see how long the axial scale must be to produce the spectrum peakiness. The sketch on the next page shows an eddy interfering with a rotor with blade gap g and stagger θ . The axial distance between chops is $\lambda = g \cot \theta$ and the gap is $g = 2\pi R/B$. Combining these formulas with the axial scale-on-radius used for Figure 28, $A/R = 0.07$ and a stagger of 60° leads to the ratio of axial scale to

axial distance $\lambda/\lambda = 0.4$. This is surprising since it indicates spectrum peaking occurs when the axial scale is shorter than the axial gap. Since Boeing obtained both noise and turbulence spectrum data supporting this result, we must conclude that it is not the mean eddies that are dominating the noise but the eddies that are larger than average.

Figure 31 shows the effect of changing blade count on turbulence/rotor interaction noise. It can be seen that doubling blade number cuts the number of peaks in half and raises their level. Also, the peak to valley ratio increases. Finally, Figure 32 shows the effect of sweeping the rotor tip 45° (in cascade system, i.e. sweep in the plane of the rotor blade). There is a significant benefit but only at the higher frequencies.

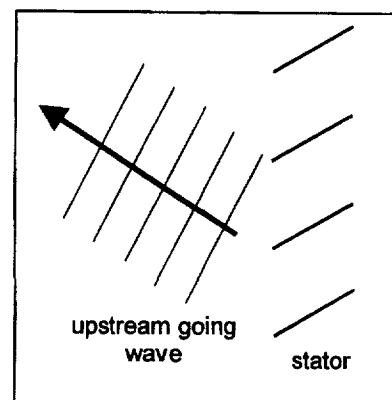
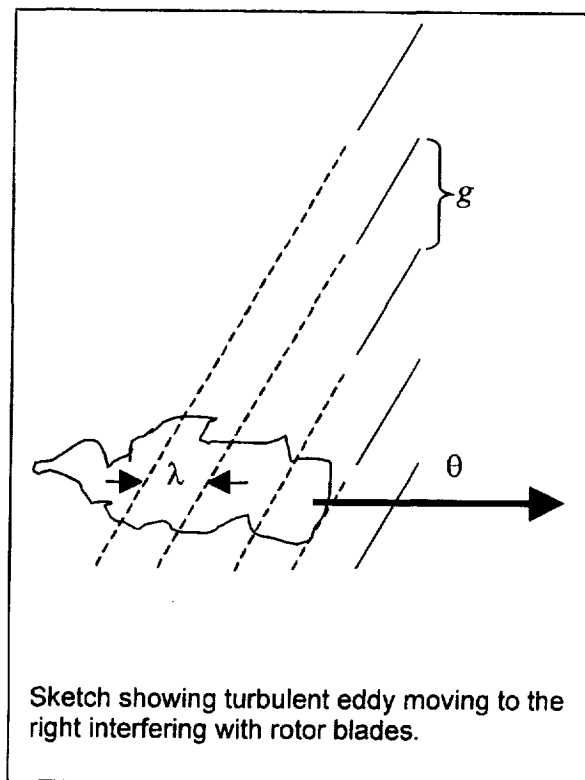
Rotor Wake / Stator Interaction Noise

For the Boeing fan data, we also look briefly at trends in stator noise with rotor tip speed and with vane count. Figure 33, copied from the Boeing report, shows inlet and aft spectra for 3 rotor speeds and 3 vane counts (15, 30, & 60). Noise increases with tip speed, as expected. Noise also increases with vane count; in fact, for the lower speeds, sound power is proportional to vane count (3 dB per doubling of vane count). At the higher speeds, the inlet noise results are more difficult to characterize, perhaps due to rotor transmission effects. Note that the solidity for the 15 and 30 vane stator were the same but that the solidity for the 60 vane stator doubled.

The corresponding theoretical curves are shown in Figure 34. To produce this figure, the geometry and mean flow from the 85% radius were matched for the 3 rpms and then turbulence intensity and scale were adjusted to fit the middle noise spectrum in the aft quadrant (78% rpm, 30 vanes). The other vane counts were computed assuming that the flow properties were unchanged. Considering that the fan is represented by a single representative radius, the trends with rpm and vane count are predicted very well. In particular, over most of the spectrum, broadband noise is proportional to vane count, an important result for design considerations.

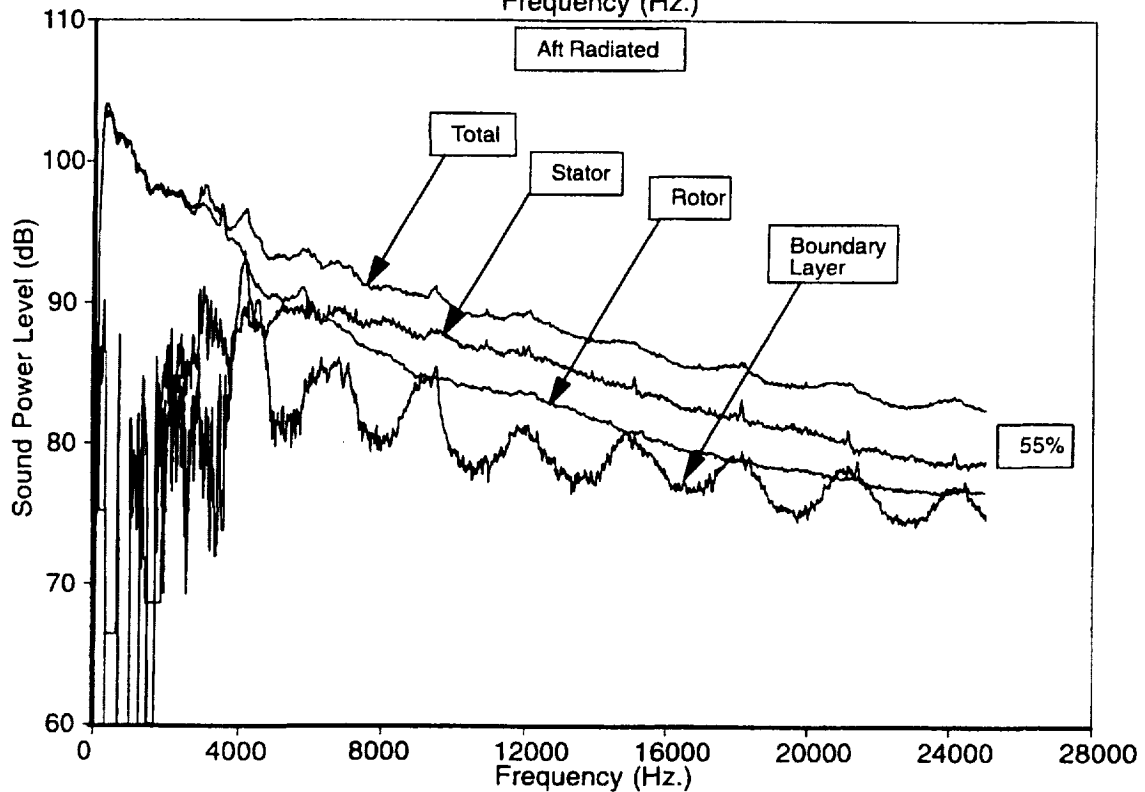
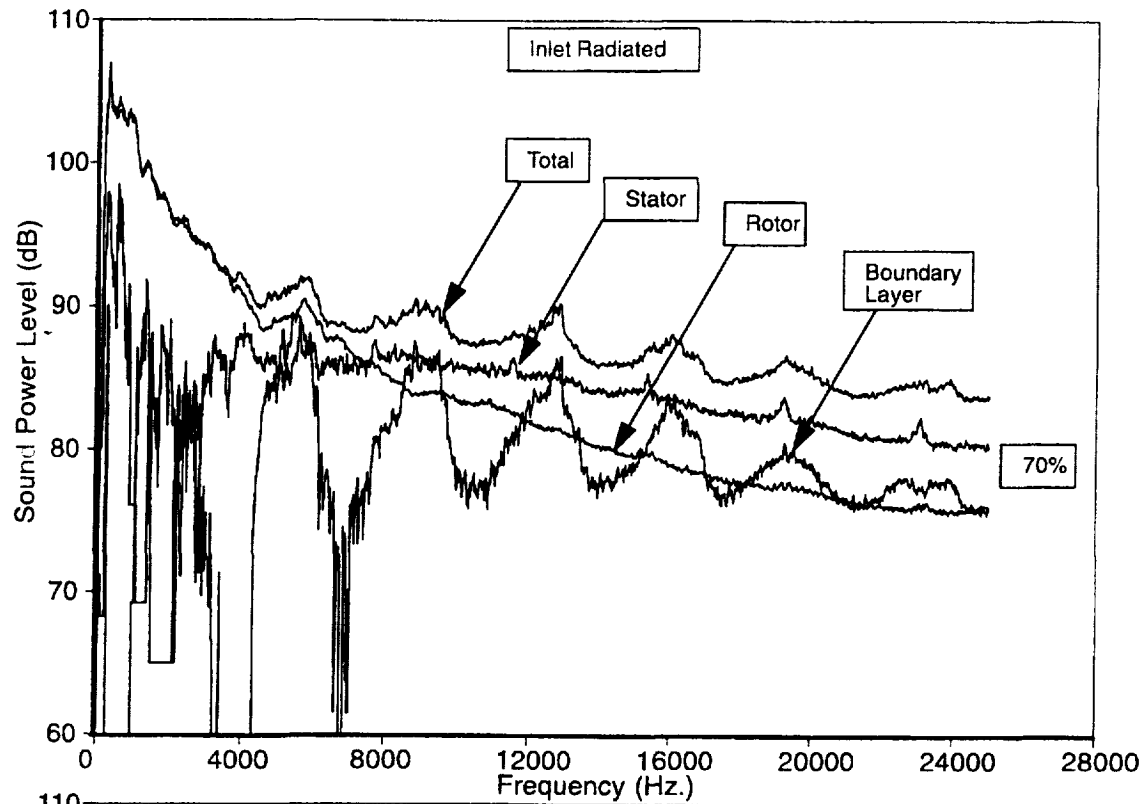
Mode Order Frequency Plots

Finally for the Boeing data, we examine mode order/frequency plots to be sure that BBCascade has the correct behavior at that level of detail. Boeing used rings of Kulite pressure transducers in their 18 inch research fan to determine the distribution over circumferential mode order (of pressure at the outer wall) as a function of frequency. Examples are shown in Figures 35 and 37, which were copied from the Boeing report (ref. 1). Figure 35 is from a ring of Kulites between rotor and stator and is believed to be dominated by stator noise. The V-shaped pattern is the cuton limit, although there are pressure modes outside this limit because of the near field location of the transducers. Co-rotating modes ($m > 0$) are dominant upstream of the stator. This is expected, based on the sketch at the right,



since waves propagating normal to the airfoil surfaces should couple most efficiently. The "cuton V" is skewed because the swirl between rotor and stator cuts on counter rotating modes at lower frequency than co-rotating modes. Figure 36 shows predicted mode order/frequency plots for sound power both up and downstream of a stator. On the upstream side (top portion of figure), the co-rotating modes clearly dominate and the cuton V is correctly skewed since the case was run with swirling input. We don't expect exact agreement with data since the experimental plots are for pressure modes and the theory is for sound power; however the correct qualitative behavior has been verified for the stator. Figure 36 also predicts downstream of the stator that the counter-rotating modes will dominate, although Boeing made no measurements at this location. Note that the cuton V is not skewed because the case was run without swirl.

What behavior do we expect upstream of the rotor? Based on a sketch analogous to the one above, we might expect that counter-rotating modes would dominate since rotor stagger has the opposite sign. However, the experimental results from Boeing indicate that again the dominant modes are co-rotating. (This issue is clouded somewhat since the data include noise from trailing edge noise as well as duct turbulence interaction.) However, the theory, shown in Figure 38 predicts dominant energy in the co-rotating modes also. Apparently, the motion of the rotor biases the energy distribution in this direction. The theory must account for this correctly via the frequency scattering, which is different for each mode order.



Sub-component spectra, radiated power, averaged over loading and tip clearance

Figure 27. Boeing's source separation results (ref. 1) showing experimentally derived rotor alone noise (no stator, no duct boundary layer), duct turbulence/rotor interaction noise, and rotor wake/stator interaction noise.

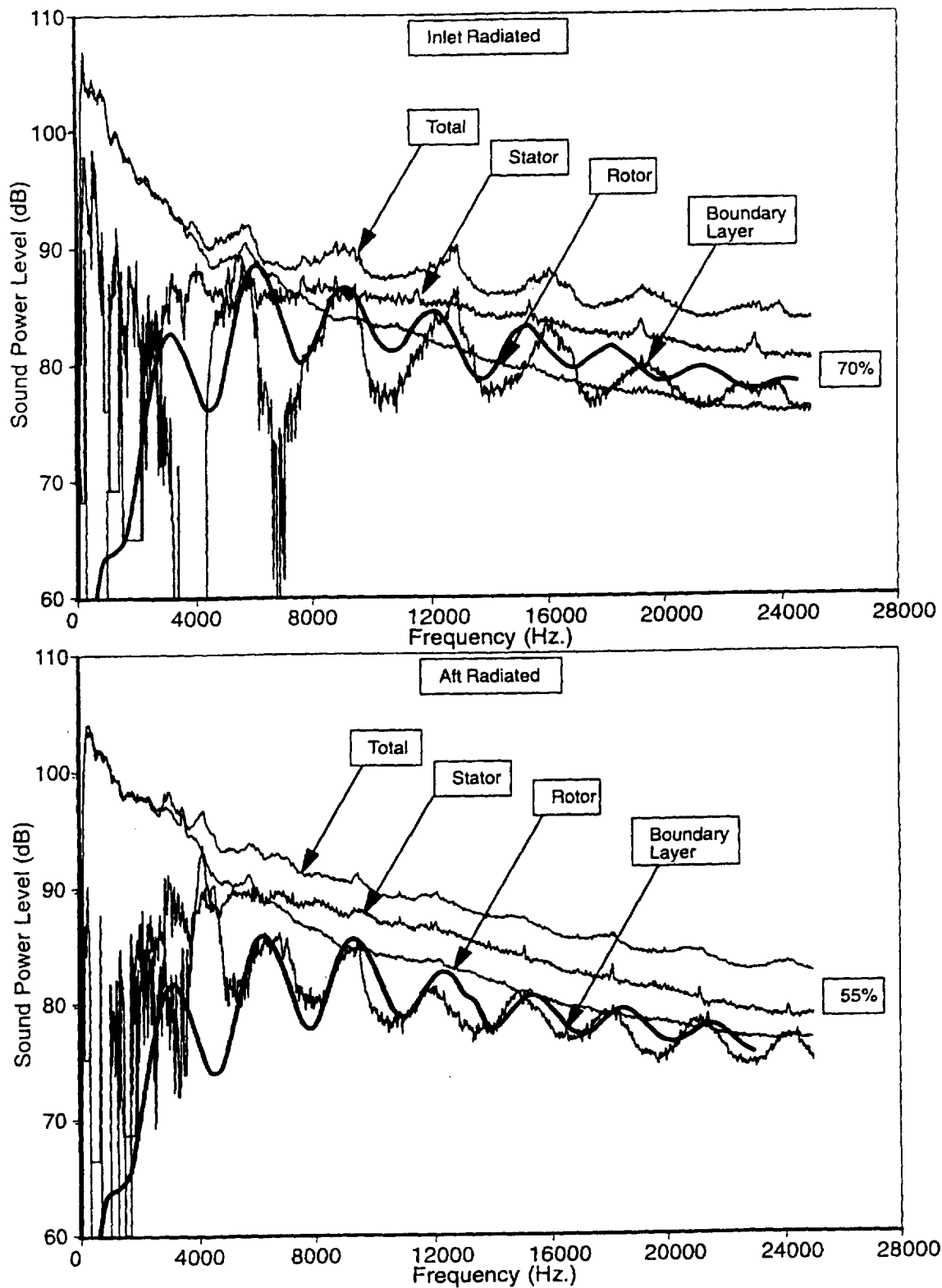


Figure 28. Calculated results from BBCascade for duct turbulence/rotor interaction superposed on Boeing's results from preceding figure.

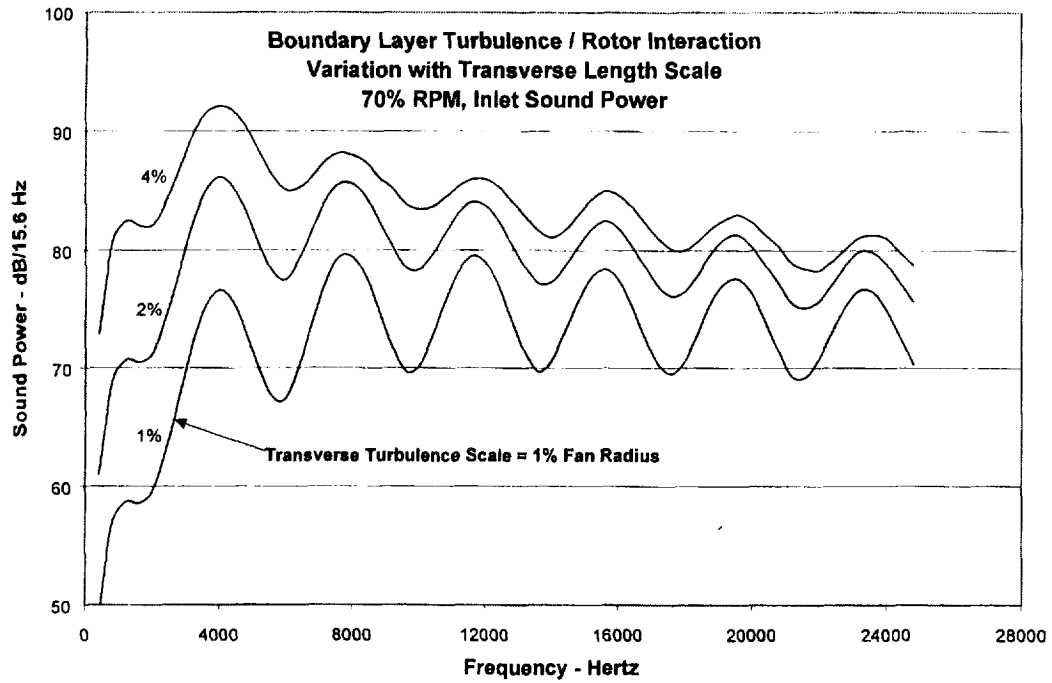


Figure 29. Variation of rotor noise with changes in transverse scale of inflow turbulence. Middle case is the match to Boeing data shown in Figure 28.

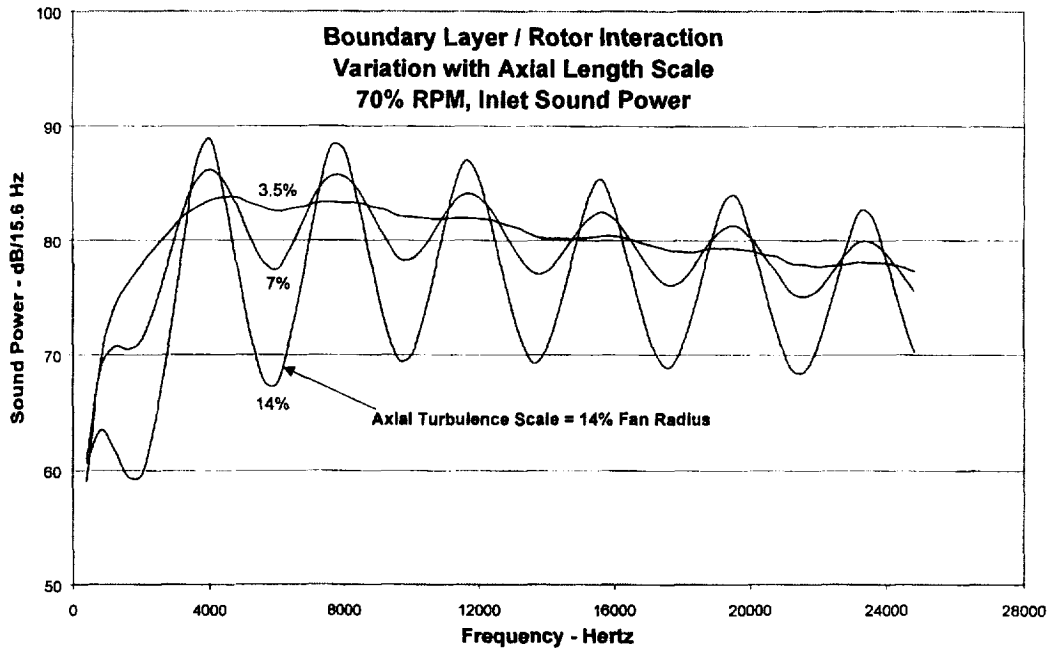


Figure 30. Variation of rotor noise with changes in axial scale of inflow turbulence. Middle case is the match to Boeing data shown in Figure 28.

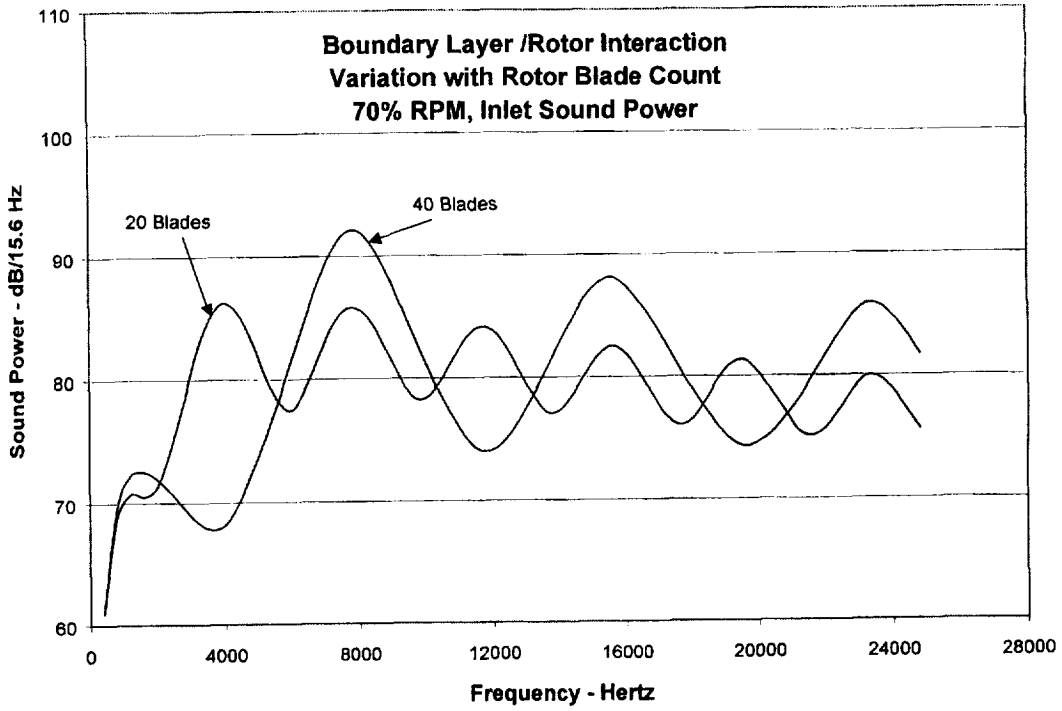


Figure 31. Variation in rotor noise with changes in blade count (at constant gap/chord).

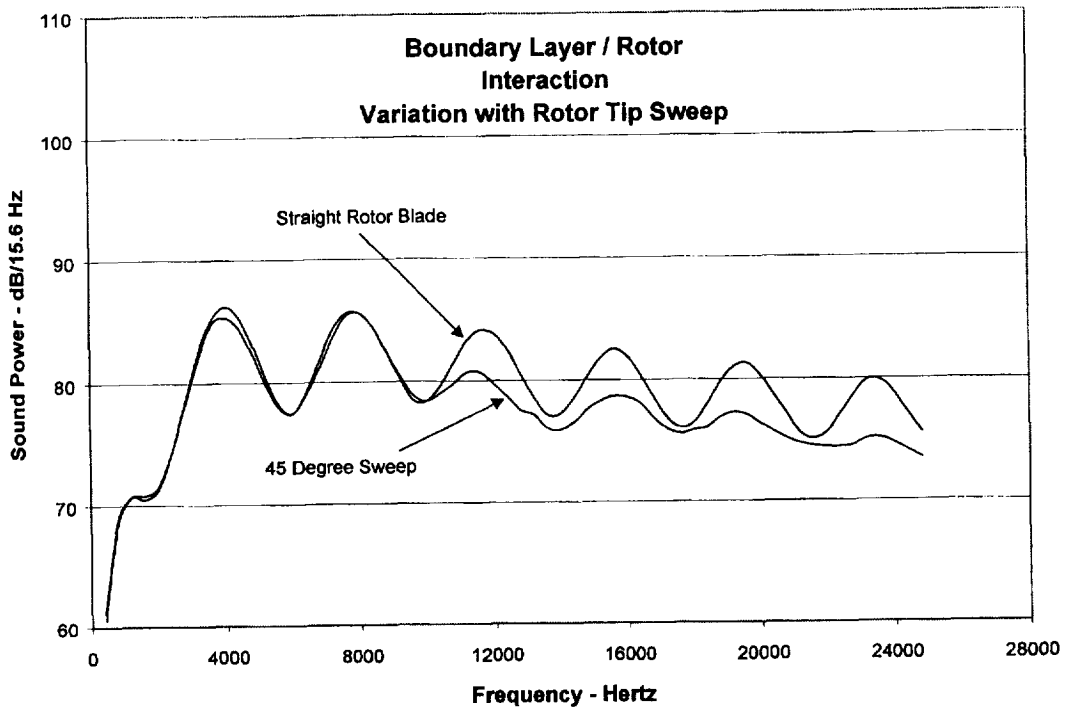


Figure 32. Variation of rotor noise with sweep. 45° sweep as defined in cascade system.

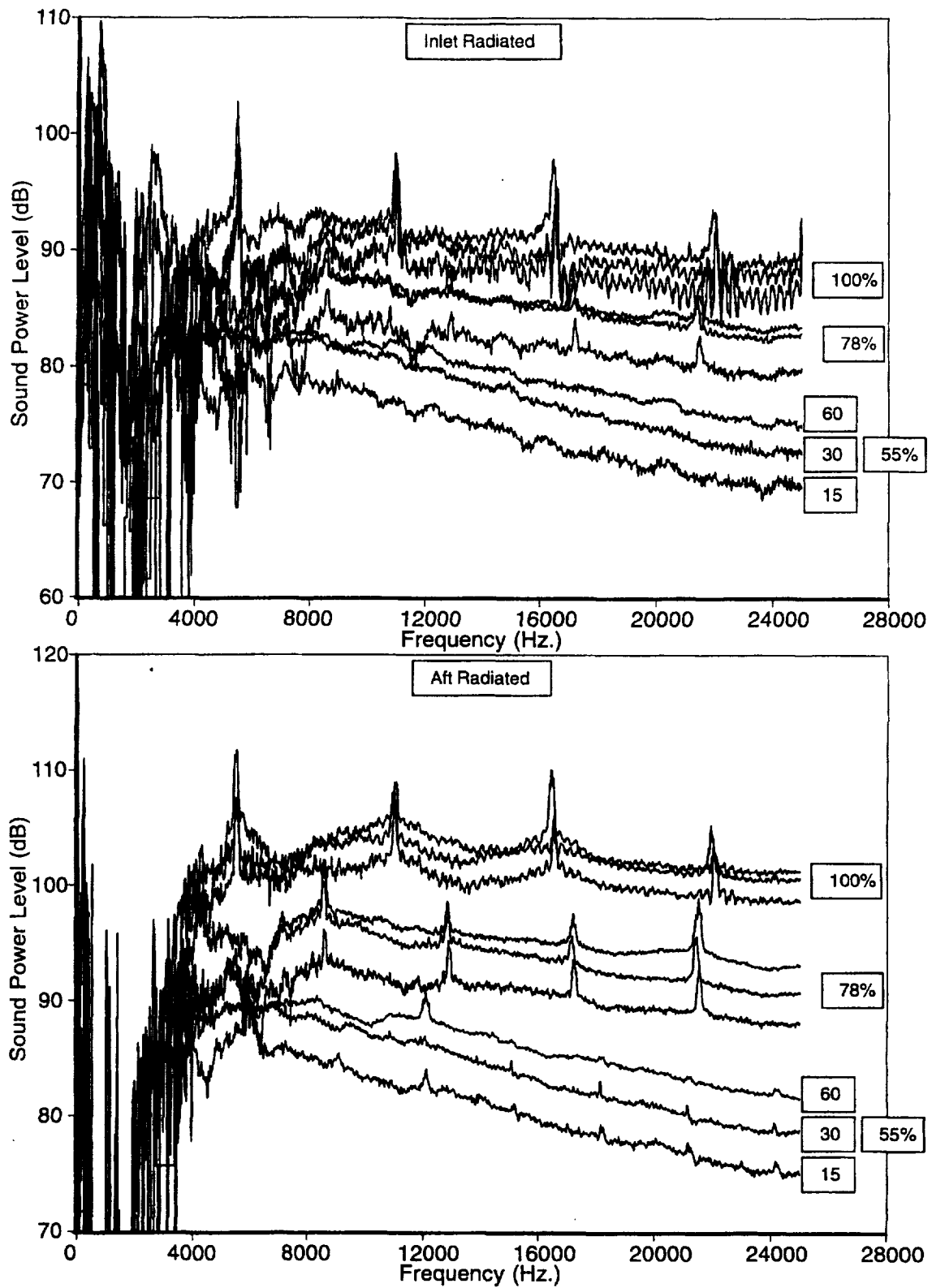


Figure 33. Figure from Boeing report (ref. 1) showing net stator noise at several fan speeds and with vane counts of 15, 30, and 60.

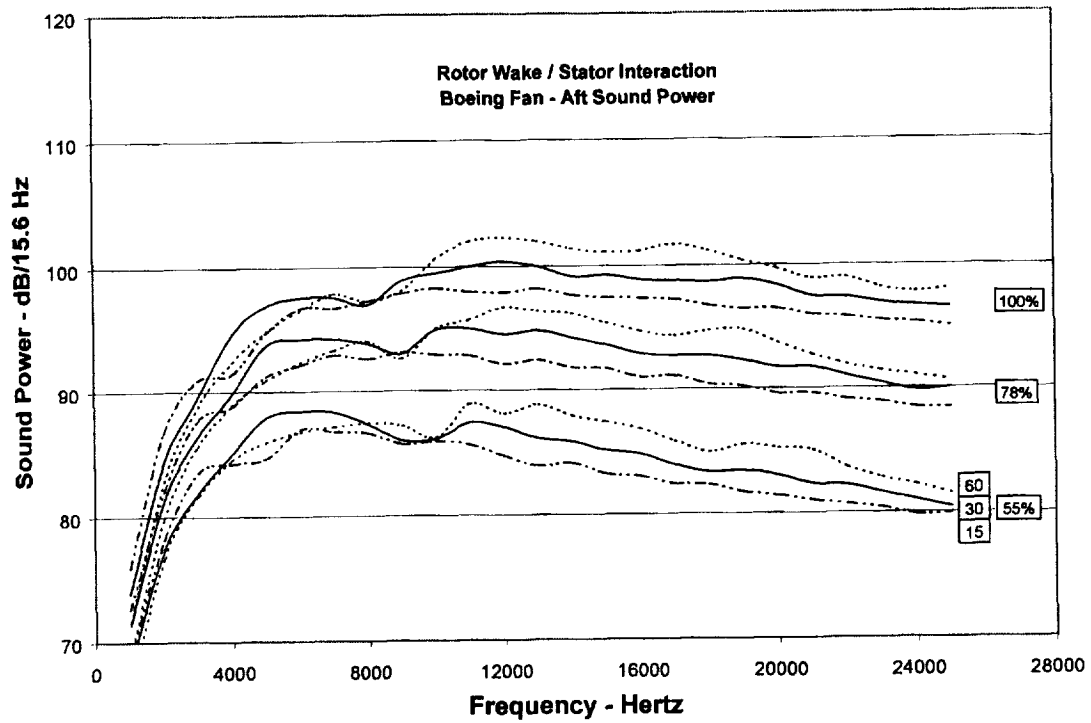
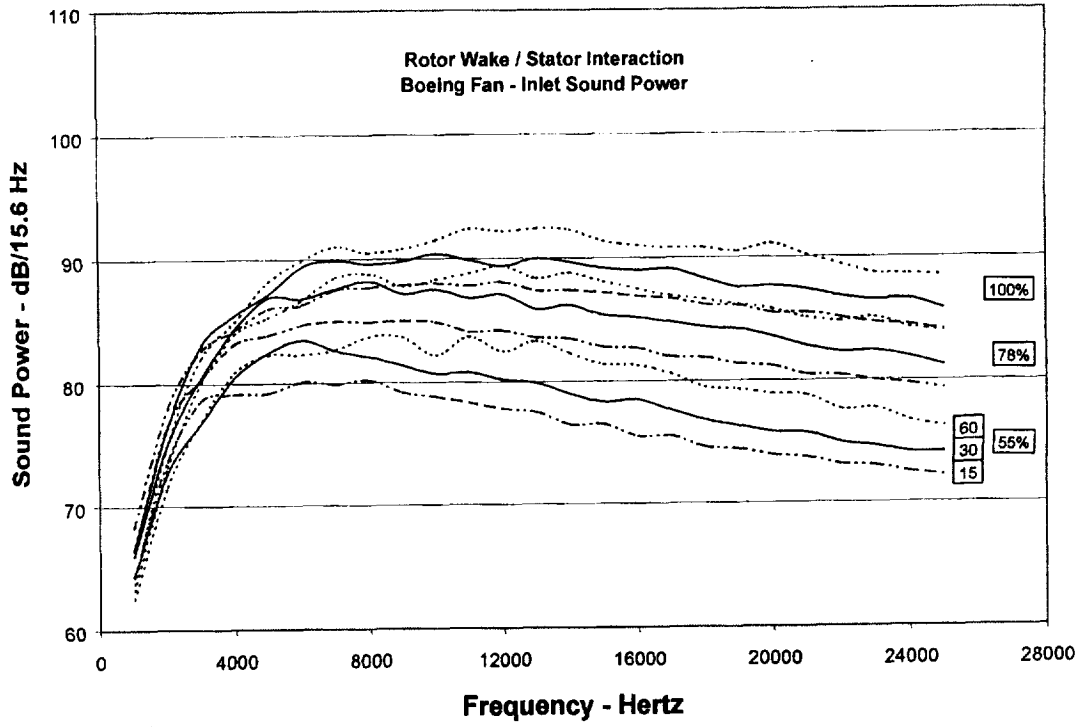


Figure 34. Calculations from BBCascade approximating conditions for Boeing fan in preceding figure.

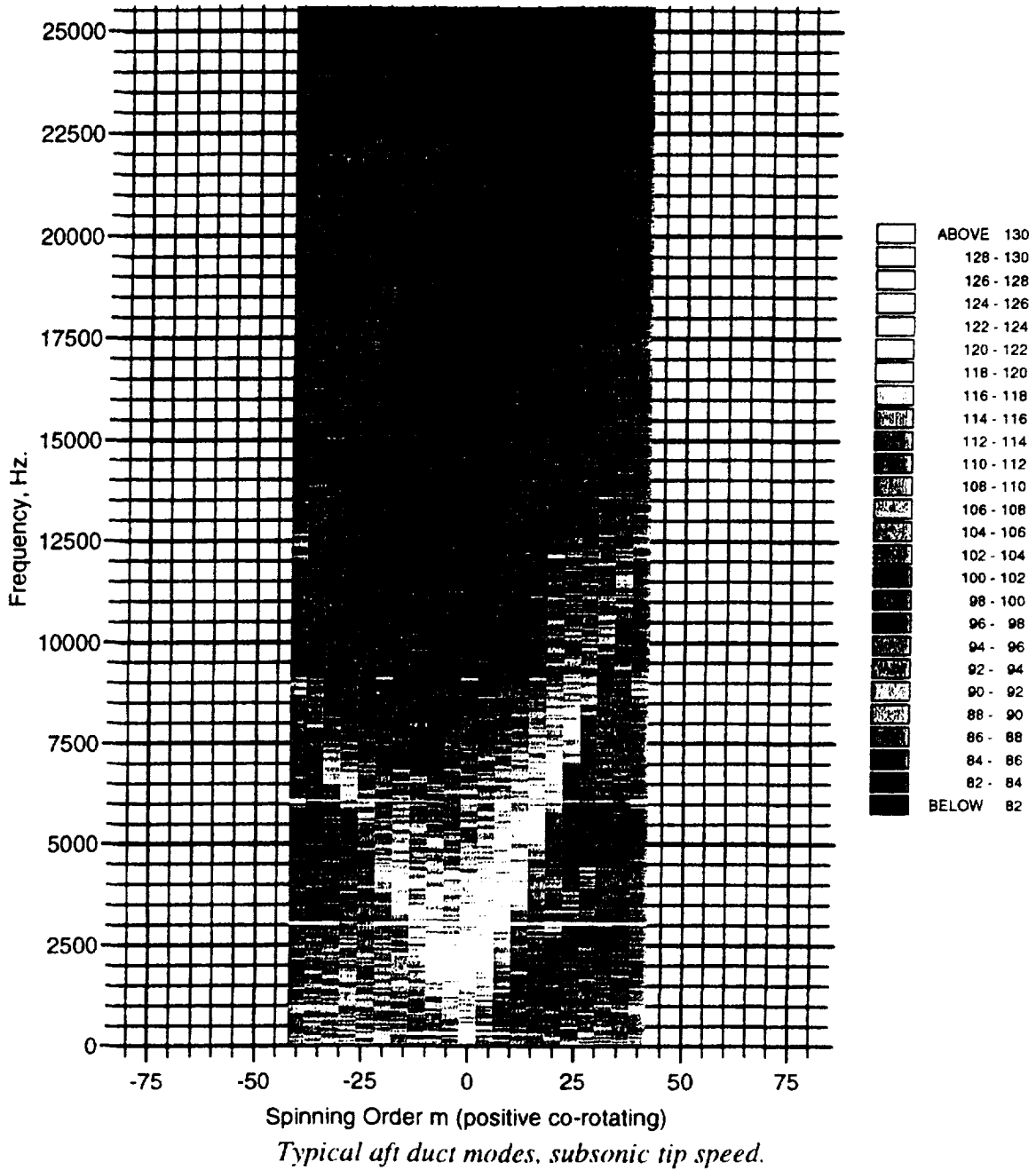


Figure 35. Mode order/frequency plot from Boeing report (ref. 1) from Kulite array between rotor and stator. Note dominance of co-rotating modes ($m > 0$). Also, note that contra-rotating modes ($m < 0$) cut on at lower frequency than co-rotating modes.

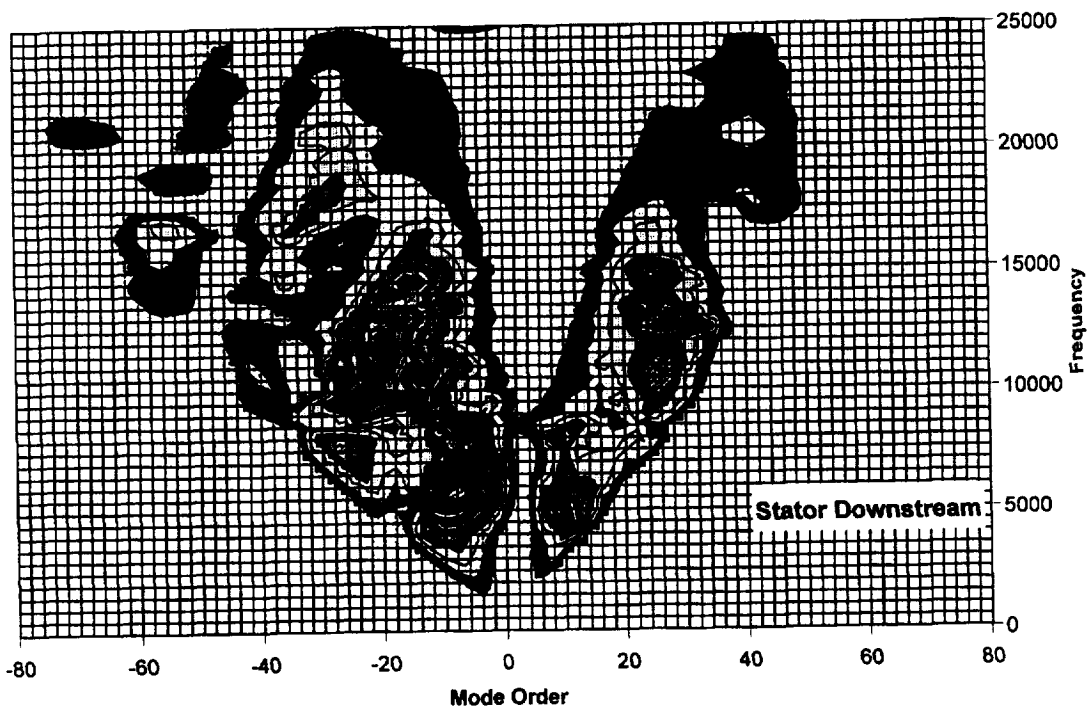
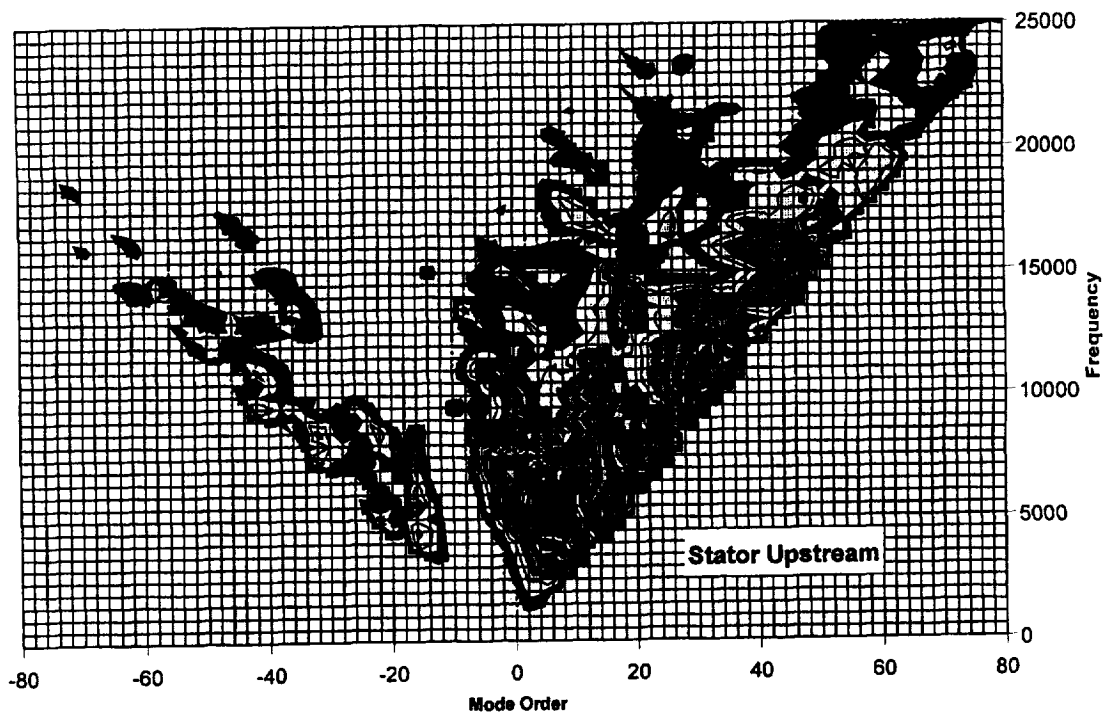


Figure 36. Mode order/frequency plots from BBCascade for stator showing distribution of sound power over circumferential order (summed over all radial wavenumbers).

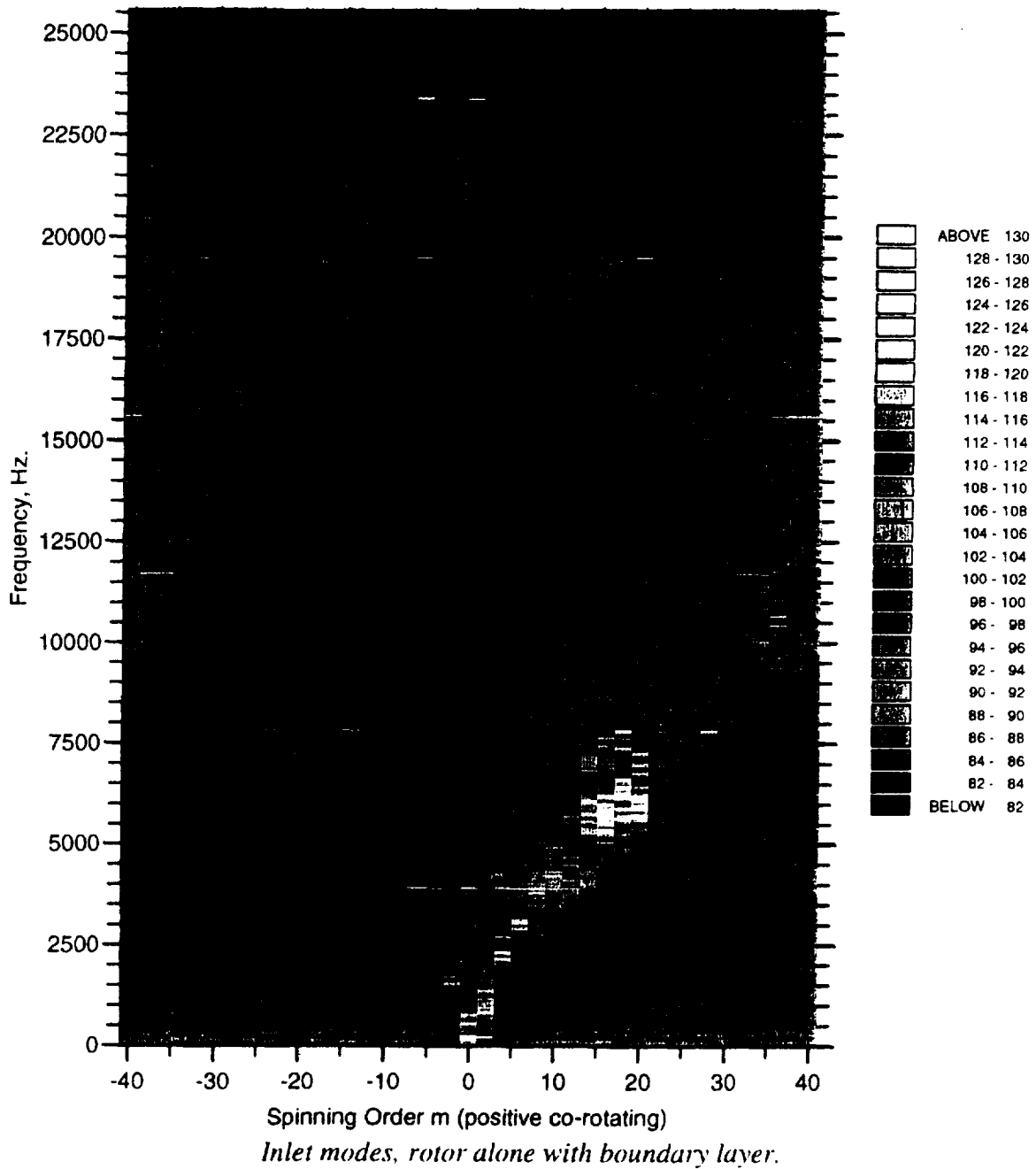


Figure 37. Mode order/frequency plot from Boeing report (ref. 1) for transducer array upstream of rotor. Test configuration without stator.

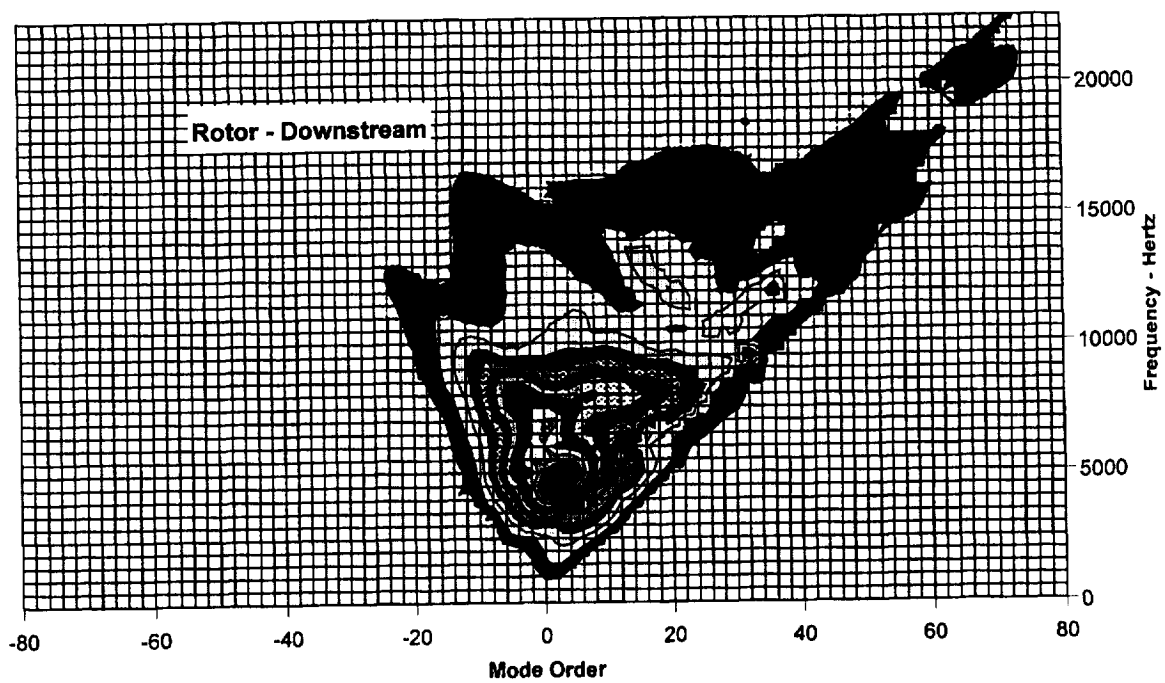
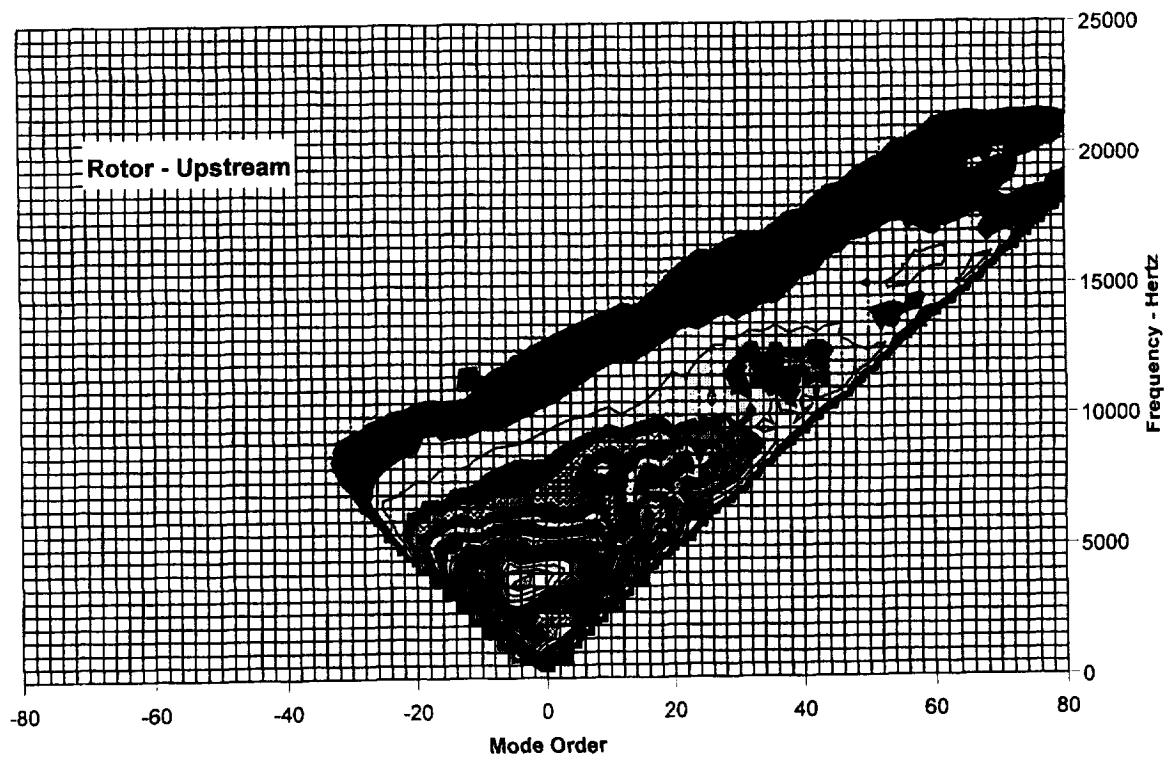


Figure 38. Mode order/frequency plots from BBCascade for rotor showing distribution of sound power over circumferential order (summed over all radial wavenumbers).



SECTION 9 CONCLUDING REMARKS

A theoretical formulation was developed for broadband noise generated by turbulence convected into a cascade. The theory was derived by applying Glegg's harmonic rectilinear cascade theory to the problem of random inflow with resulting equations giving upstream and downstream sound power spectra as integrals over the 3D turbulence spectrum. Within the limitations of the rectilinear cascade model, the analysis was made as general as possible. In particular, it treats noise from rotors as well as stators; the blades or vanes can be leaned and/or swept; and turbulence that can be inhomogeneous and can have a limited form of anisotropy. Two spectra for turbulence are provided: one is the Liepmann spectrum for homogeneous, isotropic flow; the other for axisymmetric turbulence with stretching in the direction of the mean flow. Operation of the theory was explained in some detail with actual plots of turbulence spectra and cascade power response spectra.

The theory is embodied in code BBCascade. This was developed for application to turbofan noise but does not truly provide a fan prediction method since the mean flow and geometry are independent of spanwise position. For the fan application, BBCascade has been incorporated in code BFaNS (described in a reference) with integration over varying geometry and flow properties in the spanwise direction. BFaNS also accounts for trailing edge sources at the rotor and stator.

With the constant geometry and mean flow it was instructive to perform a series of parametric studies to explore the fundamental behavior of predicted noise. The format for these studies was to first compare predictions with data from a model fan, then find flow parameters that give a convincing prediction of the noise, and finally perform parametric variation on the geometry, mean flow, and turbulence. This provides a basic understanding of the methodology and of the sensitivity of noise to various design and flow parameters. Fan models included a Pratt & Whitney 22 inch model fan, an Allison 22 inch model fan with swept and leaned stators, and a Boeing 18 inch fan designed to separate the various broadband noise sources.

Agreement with data is very convincing and explains several observed phenomena. Of most interest today perhaps, the reduction of broadband noise by leaning and sweeping stators is thoroughly investigated and the critical parameters are identified. Predicted noise is reduced by sweeping the vane in its own plane according to $\Delta dB = -30 \log_{10}(\cos \psi_s)$, where ψ_s is the sweep angle. Rotor noise also can benefit from sweep.

Other items studied include sensitivity to geometry variations such as solidity, vane count, and stagger as well as sensitivity to mean flow Mach number. Predicted noise is roughly proportional to vane count in the important frequency ranges, i.e. $PWL \propto 10 \log_{10} V$ where V is vane count. Accurate prediction of broadband noise obviously requires accurate specification of the turbulence properties. Noise increases uniformly at all frequencies with turbulence *intensity*, i.e. 3 dB per doubling of turbulence intensity, $\overline{w^2}/U^2$. However, it is also shown that knowledge of turbulence *scale* can be even a more important driver: doubling or halving transverse scale can cause noise changes greater than 3 dB.



REFERENCES

1. Ganz, U. W., Joppa, P. D., Patten, T. J., Scharpf, D. F., "Boeing 18-Inch Fan Rig Broadband Noise Test", NASA/CR-1998-208704, September 1998.
2. Hanson, D. B., "Quantification of Inflow Turbulence for Prediction of Cascade Broadband Noise", Presented at the 5th International Congress on Sound and Vibration, Adelaide, Australia, December 1997.
3. Hanson, D. B. and Horan, K. P., "Turbulence/Cascade Interaction: Spectra of Inflow, Cascade Response, and Noise", AIAA/CEAS Paper No. 98-2319 presented at the 4th AIAA/CEAS Aeroacoustics Conference, Toulouse, France, June 2-4, 1998.
4. Hanson, D. B., "Influence of Lean and Sweep on Noise of Cascades with Turbulent Inflow," AIAA Paper 99-1863, Presented at 5th AIAA/CEAS Aeroacoustics Conference, Bellevue, Washington, May 10-12, 1999.
5. Glegg, S. A. L., "The Response of a Swept Blade Row to a Three Dimensional Gust", J. Sound & Vibration, Vol. 227(1), pp. 29-64, 1999.
6. Glegg, S., "Fan Noise from Blades Moving Through Wall Boundary Layer Turbulence," Paper AIAA-99-1888, presented at the AIAA/CEAS 5th Aeroacoustics Conference, Bellevue, Washington, May 10-12, 1999.
7. Morin, B. L., "Broadband Noise Prediction System for Gas Turbine Engines", Paper AIAA-99-1889, presented at the AIAA/CEAS 5th Aeroacoustics Conference, Bellevue, Washington, May 10-12, 1999.
8. Goldstein, M. E., *Aeroacoustics*, McGraw-Hill, New York, 1976.
9. Landahl, M. T. and Mollo-Christensen, E., *Turbulence and Random Processes in Fluid Mechanics*, Cambridge University Press, 1992.
10. Liepmann H. W., "Extension of the Statistical Approach to Buffeting and Gust Response of Wings of Finite Span", Journal of the Aeronautical Sciences, March 1955.
11. Kerschen, E. J. and Gliebe, P. R., "Fan Noise Caused by the Ingestion of Anisotropic Turbulence – A Model Based on Axisymmetric Turbulence Theory", AIAA Paper No. AIAA-80-1021, Presented at the AIAA 6th Aeroacoustics Conference, Hartford, Connecticut, June 4-6, 1980.
12. Woodward, R. P., Elliot, D. M., Hughes, C. E., and Berton, J. J., "Benefits of Swept and Leaned Stators for Fan Noise Reduction," AIAA Paper 99-0479, presented at the 37th Aerospace Sciences Meeting and Exhibit, 1999, Reno, Nevada, January 11-14.
13. Mani, R., "Noise Due to Interaction of Inlet Turbulence with Isolated Stators and Rotors", J. Sound and Vibration, Vol. 17, pp. 251-260 (1971).
14. Hanson, D. B., "The Spectrum of Rotor Noise Caused by Atmospheric Turbulence," J. Acoustical Society of America, Vol. 56, No. 1, July 1974.



APPENDIX A

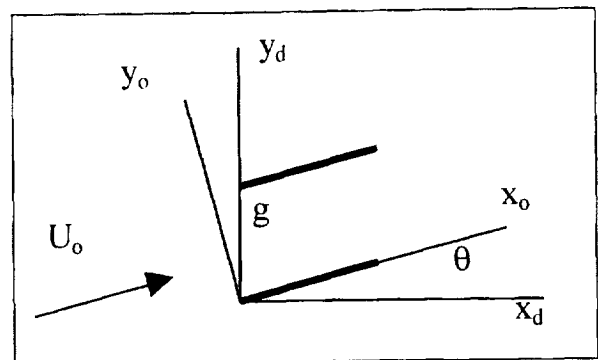
CASCADE GEOMETRY FOR LEAN AND SWEEP ANALYSIS

This appendix derives geometrical relations between duct coordinates (where chord, gap, and stagger angle are c_d, g, θ) and Glegg's cascade coordinates (where chord, gap, and stagger angle are c, s, χ). In the process, we develop the coordinate transformation equations and also define lean and sweep according to 2 different conventions. Geometry for the derivation is presented in Figure 4 of the main text.

Stagger, lean, and sweep are defined by 3 successive rotations about coordinate axes as described in Section 3. The rotations are non-commutative so that the order of the rotations must be part of the convention.

Coordinate Rotations

Stagger is the rotation from the duct system (x_d, y_d, z_d) to the (x_o, y_o, z_o) coordinates. The latter system is used in the main text for analysis of the turbulence Fourier transforms. The sketch at the right represents a cylindrical cut of the stator unwrapped onto a plane. Gap and stagger angle are g and θ .



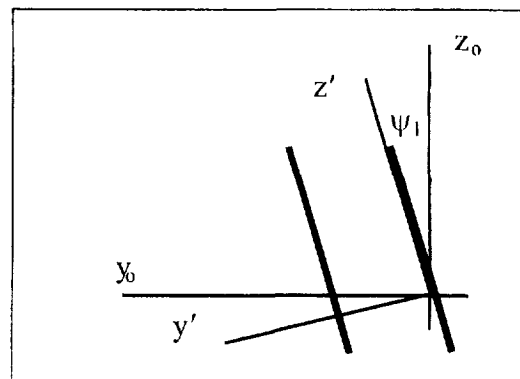
The transformation can be written in matrix form as

$$\begin{bmatrix} x_o \\ y_o \\ z_o \end{bmatrix} = [Q_\theta] \times \begin{bmatrix} x_d \\ y_d \\ z_d \end{bmatrix} \quad (\text{A-1})$$

where

$$[Q_\theta] = \begin{bmatrix} \cos \theta & \sin \theta & 0 \\ -\sin \theta & \cos \theta & 0 \\ 0 & 0 & 1 \end{bmatrix} \quad (\text{A-2})$$

Lean is a rotation through angle ψ_l about the common x_o, x_d axes into the primed system as shown at the right. Consider the vanes to have “hooks” on their leading edges attaching them to the y_d axis. Thus, the cascade does not rotate as a unit. Rather, each vane rotates on its hook, maintaining the original gap g at constant radius. However, the normal gap, used in the cascade theory varies with lean per formulas given later in this appendix.



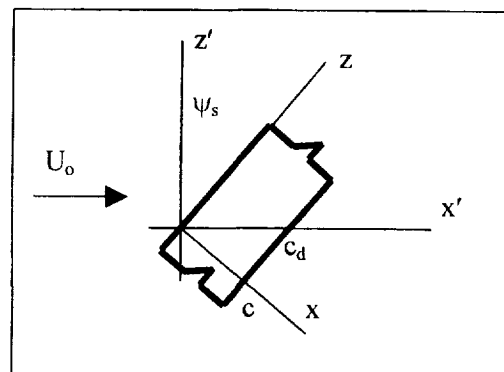
The transformation is

$$\begin{bmatrix} x' \\ y' \\ z' \end{bmatrix} = [Q_l] \times \begin{bmatrix} x_o \\ y_o \\ z_o \end{bmatrix} \quad (A-3)$$

where

$$[Q_l] = \begin{bmatrix} 1 & 0 & 0 \\ 0 & \cos \psi_l & -\sin \psi_l \\ 0 & \sin \psi_l & \cos \psi_l \end{bmatrix} \quad (A-4)$$

Sweep is a rotation of the vane (*in its own plane*) about the y' axis through angle ψ_s . This establishes the chord at constant radius in duct coordinates as c_d and the chord, measured normal to the leading edge as c with the relation $c = c_d \cos \psi_s$.



The transformation is

$$\begin{bmatrix} x \\ y \\ z \end{bmatrix} = [Q_s] \times \begin{bmatrix} x' \\ y' \\ z' \end{bmatrix} \quad (A-5)$$

where

$$[Q_s] = \begin{bmatrix} \cos \psi_s & 0 & -\sin \psi_s \\ 0 & 1 & 0 \\ \sin \psi_s & 0 & \cos \psi_s \end{bmatrix} \quad (A-6)$$

The net result of the 3 rotations is

$$[Q] = [Q_s] \times [Q_l] \times [Q_\theta] \quad (A-7)$$

or

$$[Q] = \begin{bmatrix} \cos\theta \cos\psi_s + \sin\theta \sin\psi_l \sin\psi_s & \sin\theta \cos\psi_s - \cos\theta \sin\psi_l \sin\psi_s & -\cos\psi_l \sin\psi_s \\ -\sin\theta \cos\psi_l & \cos\theta \cos\psi_l & -\sin\psi_l \\ \cos\theta \sin\psi_s - \sin\theta \sin\psi_l \cos\psi_s & \sin\theta \sin\psi_s + \cos\theta \sin\psi_l \cos\psi_s & \cos\psi_l \cos\psi_s \end{bmatrix} \quad (A-8)$$

giving the desired transformation of the duct coordinates into the cascade coordinates:

$$\begin{bmatrix} x \\ y \\ z \end{bmatrix} = [Q] \times \begin{bmatrix} x_d \\ y_d \\ z_d \end{bmatrix} \quad (A-9)$$

The inverse transformation is also useful and is just the transpose of $[Q]$. Define the inverse as

$$[q] = [Q]^{-1} \quad (A-10)$$

so that

$$\begin{bmatrix} x_d \\ y_d \\ z_d \end{bmatrix} = [q] \times \begin{bmatrix} x \\ y \\ z \end{bmatrix} \quad (A-11)$$

where

$$[q] = \begin{bmatrix} \cos\theta \cos\psi_s + \sin\theta \sin\psi_l \sin\psi_s & -\sin\theta \cos\psi_l & \cos\theta \sin\psi_s - \sin\theta \sin\psi_l \cos\psi_s \\ \sin\theta \cos\psi_s - \cos\theta \sin\psi_l \sin\psi_s & \cos\theta \cos\psi_l & \sin\theta \sin\psi_s + \cos\theta \sin\psi_l \cos\psi_s \\ -\cos\psi_l \sin\psi_s & -\sin\psi_l & \cos\psi_l \cos\psi_s \end{bmatrix} \quad (A-12)$$

Lean and Sweep as Viewed Parallel and Perpendicular to Fan Axis

Another scheme to define lean and sweep is according to the front and side views of the unwrapped blade row, as sketched in Figure 5. From the front (looking along the x_d axis) the lean angle is $\hat{\psi}_l$ and looking from the side the sweep angle is $\hat{\psi}_s$. In cascade coordinates, the leading edge of the reference blade is located at $x=0, y=0$. Equation A-11 transforms this to the duct system:

$$\begin{aligned} x_d &= q_{13}z \\ y_d &= q_{23}z \\ z_d &= q_{33}z \end{aligned} \quad (A-13)$$

From the front, the slope is $\tan \hat{\psi}_l = y_d / z_d = q_{23} / q_{33}$ and from the side, the slope is $\tan \hat{\psi}_s = x_d / z_d = q_{13} / q_{33}$ or

$$\begin{aligned}\tan \hat{\psi}_l &= \frac{Q_{32}}{Q_{33}} = \frac{\sin \theta \sin \psi_s + \cos \theta \sin \psi_l \cos \psi_s}{\cos \psi_l \cos \psi_s} \\ \tan \hat{\psi}_s &= \frac{Q_{31}}{Q_{33}} = \frac{\cos \theta \sin \psi_s - \sin \theta \sin \psi_l \cos \psi_s}{\cos \psi_l \cos \psi_s}\end{aligned}\quad (\text{A-14})$$

These equations can be inverted to give

$$\begin{aligned}\tan \psi_l &= \cos \theta \tan \hat{\psi}_l - \sin \theta \tan \hat{\psi}_s \\ \tan \psi_s &= \cos \psi_l (\sin \theta \tan \hat{\psi}_l + \cos \theta \tan \hat{\psi}_s)\end{aligned}\quad (\text{A-15})$$

which must be solved sequentially.

Other expressions required in the text can be obtained from $\sin^2 \hat{\psi}_s + \cos^2 \hat{\psi}_s = 1$:

$$\sin \hat{\psi}_s = \frac{Q_{31}}{\sqrt{Q_{31}^2 + Q_{33}^2}} \quad \cos \hat{\psi}_s = \frac{Q_{33}}{\sqrt{Q_{31}^2 + Q_{33}^2}}\quad (\text{A-16})$$

Finally, for Equation 51, we need an expression for $g / (s \cos \hat{\psi}_s)$. For this, first note that the square root in the expression for $\cos \hat{\psi}_s$ above can be written

$$\sqrt{Q_{31}^2 + Q_{33}^2} = \sqrt{Q_{31}q_{13} + Q_{33}q_{33}}\quad (\text{A-17})$$

where q is the inverse (and therefore transpose) of Q . And since $Q \times q = \mathbf{1}$, it can be seen that $Q_{31}q_{13} + Q_{32}q_{23} + Q_{33}q_{33} = 1$. Therefore

$$\sqrt{Q_{31}^2 + Q_{33}^2} = \sqrt{1 - Q_{32}q_{23}}\quad (\text{A-18})$$

Similarly, from Equation A-23 (below)

$$\frac{s}{g} = \sqrt{Q_{12}^2 + Q_{22}^2} = \sqrt{q_{21}Q_{12} + q_{22}Q_{22}} = \sqrt{1 - q_{23}Q_{32}}\quad (\text{A-19})$$

Then, combining, Equations 16, 18, and 19, we find the desired result for Equation 51

$$\frac{g}{s \cos \hat{\psi}_s} = \frac{1}{Q_{33}} = \frac{1}{\cos \psi_l \cos \psi_s}\quad (\text{A-20})$$

Relations Between Definitions of Chord, Gap, and Stagger

Given the geometry in the duct system in terms of chord c_d , gap g , and stagger angle θ , we can now find the corresponding quantities in the cascade (Glegg's) system. To do this, we note that the coordinates of one point on vane #1 in duct coordinates are $x_d = 0$, $y_d = g$, $z_d = 0$. From Equations B-11 and B-12, the corresponding point on vane #1 in the cascade coordinates is at

$$\begin{aligned} x &= Q_{12} g = (\sin \theta \cos \psi_s - \cos \theta \sin \psi_l \sin \psi_s) g \\ y &= Q_{22} g = (\cos \theta \cos \psi_l) g \\ z &= Q_{32} g = (\sin \theta \sin \psi_s + \cos \theta \sin \psi_l \cos \psi_s) g \end{aligned} \quad (\text{A-21})$$

Since the leading edge is normal to the x, y plane in cascade coordinates, x and y are Glegg's d and h in the sketch below.



Thus, we have

$$\begin{aligned} d &= Q_{12} g = (\sin \theta \cos \psi_s - \cos \theta \sin \psi_l \sin \psi_s) g \\ h &= Q_{22} g = (\cos \theta \cos \psi_l) g \end{aligned} \quad (\text{A-22})$$

And, from these, we immediately write down the expressions for Glegg's gap and stagger angle:

$$s = \sqrt{d^2 + h^2} = g \sqrt{Q_{12}^2 + Q_{22}^2} \quad (\text{A-23})$$

$$\tan \chi = d/h = Q_{12}/Q_{22} \quad (\text{A-24})$$

We have already noted that Glegg's chord is

$$c = c_d \cos \psi_s \quad (\text{A-25})$$

Also, note from the sketch above that the velocity components are

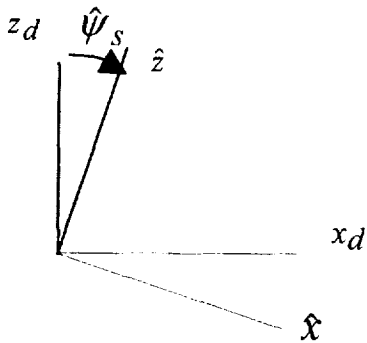
$$\begin{aligned} U &= U_o \cos \psi_s \\ W &= U_o \sin \psi_s \end{aligned} \quad (\text{A-26})$$

where U_o is the full velocity into the cascade (assumed to have no radial component in the duct system).

Thus, for a typical application, we might be given chord c_d , gap g , stagger θ , lean and sweep angles, $\hat{\psi}_l$ and $\hat{\psi}_s$ in the duct system. Lean and sweep would be converted to the “no hat” system via Equations A-15. Then the chord c , gap s , and stagger χ for Glegg’s geometry would be obtained from Equations A-25, A-23, and A-24 and his velocity components from Equations A-26. Interblade phase angle and spanwise wavenumber are discussed in the main text.

Rotation from the “Duct” System to the “Hat” Coordinate System

One more coordinate system is needed in the main body of the report for integration of intensity over the cascade face to obtain sound power. This is the “hat” system reached by rotating about the transverse duct axis y_d through the angle $\hat{\psi}_s$ per the sketch below. The transformation from the duct system to the “hat” system is



$$\begin{bmatrix} x_d \\ y_d \\ z_d \end{bmatrix} = \begin{bmatrix} \cos \hat{\psi}_s & 0 & \sin \hat{\psi}_s \\ 0 & 1 & 0 \\ -\sin \hat{\psi}_s & 0 & \cos \hat{\psi}_s \end{bmatrix} \times \begin{bmatrix} \hat{x} \\ \hat{y} \\ \hat{z} \end{bmatrix} \quad (\text{A-27})$$

and hence the net transformation from the “hat” system to Glegg’s cascade system, namely

$$\begin{bmatrix} x \\ y \\ z \end{bmatrix} = \begin{bmatrix} \hat{Q} \end{bmatrix} \times \begin{bmatrix} \hat{x} \\ \hat{y} \\ \hat{z} \end{bmatrix} \quad (\text{A-28})$$

is given by the matrix

$$\begin{bmatrix} \hat{Q} \end{bmatrix} = \begin{bmatrix} Q \end{bmatrix} \times \begin{bmatrix} \cos \hat{\psi}_s & 0 & \sin \hat{\psi}_s \\ 0 & 1 & 0 \\ -\sin \hat{\psi}_s & 0 & \cos \hat{\psi}_s \end{bmatrix} \quad (\text{A-29})$$

or

$$\hat{Q} = \begin{bmatrix} (Q_{11} \cos \hat{\psi}_s - Q_{13} \sin \hat{\psi}_s) & Q_{12} & (Q_{11} \sin \hat{\psi}_s + Q_{13} \cos \hat{\psi}_s) \\ (Q_{21} \cos \hat{\psi}_s - Q_{23} \sin \hat{\psi}_s) & Q_{22} & (Q_{21} \sin \hat{\psi}_s + Q_{23} \cos \hat{\psi}_s) \\ (Q_{31} \cos \hat{\psi}_s - Q_{33} \sin \hat{\psi}_s) & Q_{32} & (Q_{31} \sin \hat{\psi}_s + Q_{33} \cos \hat{\psi}_s) \end{bmatrix} \quad (\text{A-30})$$

and, by use of Equations A-16 and $Q \times q = 1$, an alternate form can be found

$$\hat{Q} = \begin{bmatrix} \frac{Q_{11}Q_{33} - Q_{13}Q_{31}}{\sqrt{Q_{31}^2 + Q_{33}^2}} & Q_{12} & \frac{-Q_{32}Q_{12}}{\sqrt{Q_{31}^2 + Q_{33}^2}} \\ \frac{Q_{21}Q_{33} - Q_{23}Q_{31}}{\sqrt{Q_{31}^2 + Q_{33}^2}} & Q_{22} & \frac{-Q_{32}Q_{22}}{\sqrt{Q_{31}^2 + Q_{33}^2}} \\ 0 & Q_{32} & \frac{1 - Q_{32}^2}{\sqrt{Q_{31}^2 + Q_{33}^2}} \end{bmatrix} \quad (\text{A-31})$$

This is used in Section 4 of the main text and in Appendix B.



APPENDIX B WAVENUMBERS IN VARIOUS COORDINATE SYSTEMS

In the main body of this report, wavenumber vectors must be expressed in a variety of coordinate systems. This appendix addresses that issue in general and also derives a relation involving wavenumbers that is needed for Equation 42 in derivation of the acoustic equations.

The first issue is easily addressed. In Appendix A several coordinate system were defined by rotations about coordinate axes. Matrices representing these rotations were derived and given names of Q with various subscripts, tildes, and hats. A basic theorem of tensor analysis is that the matrix that rotates position vectors also rotates other vectors. Hence, if

$$\begin{bmatrix} x \\ y \\ z \end{bmatrix} = \begin{bmatrix} & & \\ & \hat{Q} & \\ & & \end{bmatrix} \times \begin{bmatrix} \hat{x} \\ \hat{y} \\ \hat{z} \end{bmatrix} \quad (\text{B-1})$$

then

$$\begin{bmatrix} \gamma_o \\ \alpha \\ \nu \end{bmatrix} = \begin{bmatrix} & & \\ & \hat{Q} & \\ & & \end{bmatrix} \times \begin{bmatrix} \hat{k}_{xd} \\ \hat{k}_{yd} \\ \hat{k}_{zd} \end{bmatrix} \quad (\text{B-2})$$

The other topic of this appendix is to re-express the exponential in Equation 42 in a form more suitable for integration. We extract the term

$$E_R = -\lambda_k^\pm x + \left(\lambda_k^\pm \frac{d}{h} + \frac{\sigma - 2\pi k}{h} \right) y + \nu z + \omega_k t \quad (\text{B-3})$$

from Equation 42. This expresses the kinematics of the cascade *response* waves. We will express this in the $\hat{x}, \hat{y}, \hat{z}$ system, identify the wavenumbers of the *excitation* waves in this system, and then re-write the exponential in the desired form. If we use Equation B-1 to transform the x, y, z coordinates, E_R becomes

$$\begin{aligned} E_R = & [-\lambda_k^\pm \hat{Q}_{11} + \left(\lambda_k^\pm \frac{d}{h} + \frac{\sigma - 2\pi k}{h} \right) \hat{Q}_{21} + \nu \hat{Q}_{31}] \hat{x} \\ & + [-\lambda_k^\pm \hat{Q}_{12} + \left(\lambda_k^\pm \frac{d}{h} + \frac{\sigma - 2\pi k}{h} \right) \hat{Q}_{22} + \nu \hat{Q}_{32}] \hat{y} \\ & + [-\lambda_k^\pm \hat{Q}_{13} + \left(\lambda_k^\pm \frac{d}{h} + \frac{\sigma - 2\pi k}{h} \right) \hat{Q}_{23} + \nu \hat{Q}_{33}] \hat{z} \end{aligned} \quad (\text{B-4})$$

The terms involving the λ 's on the 2nd and 3rd lines cancel, leaving

$$\begin{aligned} E_R = & [-\lambda_k^\pm \hat{Q}_{11} + \left(\lambda_k^\pm \frac{d}{h} + \frac{\sigma - 2\pi k}{h} \right) \hat{Q}_{21} + \nu \hat{Q}_{31}] \hat{x} \\ & + \left[\left(\frac{\sigma - 2\pi k}{g} \right) + \nu \hat{Q}_{32} \right] \hat{y} + \left[\left(\frac{\sigma - 2\pi k}{h} \right) \hat{Q}_{23} + \nu \hat{Q}_{33} \right] \hat{z} \end{aligned} \quad (\text{B-5})$$

where we have used $\hat{Q}_{12} = Q_{12}$, $\hat{Q}_{22} = Q_{22}$, $\hat{Q}_{32} = Q_{32}$. Now, we examine a similar expression for the excitation wave

$$E_E = \gamma_o x + \alpha y + \nu z = \hat{k}_{xd} \hat{x} + \hat{k}_{yd} \hat{y} + \hat{k}_{zd} \hat{z} \quad (\text{B-6})$$

The inverse of Equation B-2 leads to

$$\begin{aligned} \hat{k}_{yd} &= \hat{Q}_{12} \gamma_o + \hat{Q}_{22} \alpha + \hat{Q}_{32} \nu \\ &= Q_{12} \gamma_o + Q_{22} \alpha + Q_{32} \nu \\ &= \frac{\sigma}{g} + Q_{32} \nu \end{aligned} \quad (\text{B-7})$$

and

$$\begin{aligned} \hat{k}_{zd} &= \hat{Q}_{13} \gamma_o + \hat{Q}_{23} \alpha + \hat{Q}_{33} \nu \\ &= \hat{Q}_{23} \frac{\sigma}{h} + \hat{Q}_{33} \nu \end{aligned} \quad (\text{B-8})$$

Now, we can identify the excitation terms in Equation B-5 and re-write it as follows

$$E_R = \hat{k}_{xk}^a \hat{x} + \left(\hat{k}_{yd} - \frac{2\pi k}{g} \right) \hat{y} + \left(\hat{k}_{zd} - \frac{2\pi k}{h} \hat{Q}_{23} \right) \hat{z} \quad (\text{B-9})$$

where

$$\hat{k}_{xk}^a = -\lambda_k^\pm \hat{Q}_{11} + \left(\lambda_k^\pm \frac{d}{h} + \frac{\sigma - 2\pi k}{h} \right) \hat{Q}_{21} + \nu \hat{Q}_{31} \quad (\text{B-10})$$

is the response wavenumber in the \hat{x} direction. If we use Equations 23 and B-7 and note that $\hat{k}_{yd} = k_{yd}$, then

$$\omega_k = -k_{yd} \Omega R + kB\Omega \quad (\text{B-11})$$

and Equation 43 of the main text follows immediately.

APPENDIX C

SYMBOLS AND SUMMARY OF COORDINATES AND WAVENUMBERS

Symbols

a	speed of sound
c	airfoil chord, measured normal to leading edge, see Figure 3
c_d	airfoil chord, measured at constant radius, see Figure 4
\bar{c}	$= c/R$
d	stagger distance, see Figure 3
f_k	see Equation 6
g	blade gap measured at constant radius
h	normal distance between airfoils, see Figure 3
i	imaginary unit
k	scattering index
$k_x \dots$	see end of this appendix for summary of various wavenumber coordinate systems
m	circumferential mode order
p	acoustic pressure
s	blade gap in Glegg's coordinates, see Figure 3
s_e	see Equation 4
t	time
w	upwash velocity component, see Equation 1
w_o	complex amplitude of upwash, see Equation 1
x, y, z	see end of this appendix for summary of various spatial coordinate systems
B	blade count in rotor or vane count in stator
D	Glegg's potential function, described in Section 2, derived in ref. 5
F^\pm	see Equation 90
F^\pm	acoustic intensity component normal to cascade face, + upstream, - downstream
K_1, K_2, K_3	$\gamma_o R, \alpha R, \nu R$. Also, $k_1 R, k_2 R, k_3 R$
L	normalized turbulence integral scale, Λ/R
M	chordwise Mach number of mean flow, U/a
M_x	Mach number in axial direction
M_y	Mach number in tangential direction (stator frame)
M_T	rotor rotational Mach number, $\Omega R/a$
P_o	Ambient pressure
Q	matrix of transformation from duct coordinates to Glegg's coordinates
R	an equivalent radius used for scaling, effective radius for noise generation
ΔR	radial extent of band of turbulence causing noise
T	a random starting time used in derivation
U	mean flow velocity in chordwise direction, see Figure 3
U_o	resultant of U and W . Total mean flow velocity
V	vane count
W	mean flow velocity in spanwise direction, see Figure 3
$W(\mathbf{K}, \omega)$	Fourier transform of gust field, see Equation 17
I	Acoustic power flux vector
K	wavenumber vector
U	mean flow vector in stator frame

α	Glegg's transverse wavenumber
$\bar{\alpha}$	αc
α'	α shifted for integration, see Equation 58
β	$\sqrt{1 - M^2}$
γ_0	Glegg's chordwise wavenumber
$\bar{\gamma}_0$	$\gamma_0 c$
ϕ^\pm	acoustic velocity potential, + upstream, - downstream
ϕ_{22}	3D turbulence spectrum
κ	see Equation 5
κ_e	see Equation 5
λ	axial distance between chops of a turbulent eddy by a rotor
λ_k^\pm	see Equation 4
η_k^\pm	see Equation 6
ν	Glegg's spanwise wavenumber
$\bar{\nu}$	νc
θ	stagger (and flow) angle at constant radius
θ_s	flow angle in stator coordinates, see Figure 6
ρ_0	density of mean flow
ρ'	acoustic density perturbation
σ	interblade phase angle in Glegg's system
ω	radian frequency in stator frame
ω_g	Glegg's shifted frequency, see Equation 3
ω_k	Doppler frequency, see Equations 22 and 23
$\tilde{\omega}$	radian frequency in rotating frame. (same as ω for stator analysis)
$\bar{\omega}$	$\omega R/a$
$\hat{\omega}$	$\omega c/a$
ζ_k	see Equation 5
χ	Glegg's cascade stagger angle, see Figure 3
χ_e	see Equation 4
ψ	used with subscripts for lean and sweep angles, see discussion in Section 3
Ω	rotor angular speed
Λ	integral scale of turbulence
Φ_{22}	non-dimensional form of 3D turbulence spectrum, see Equation 68
Π^\pm	sound power upstream (+) and downstream (-), integrated over all frequency
Π_ω^\pm	sound power spectrum upstream (+) and downstream (-), see Equation 55